University of Sussex

Surface Terahertz Phenomena

Luke A.S. Peters

Submitted for the degree of Doctor of Philosophy

University of Sussex

29th May 2018

Declaration

I hereby declare that this thesis has not been and will not be submitted in whole or in part to another University for the award of any other degree. This thesis conforms to a 'papers style' format in which a substantial part of the contents are reproductions from published and un-published submissions to journals in which I was the first Author. I hereby declare that the experimental and theoretical work presented in those papers was my own.

Signature:

Luke Peters May 2018

UNIVERSITY OF SUSSEX

Luke Peters, Doctor of Philosophy

Surface Terahertz Phenomena

Summary

With the massive advantages of THz radiation and the current technical difficulties in mind, I have chosen to undertake research into terahertz surface phenomena, which is the focal point of my thesis. Ultrathin surface terahertz emitters have many advantages as they have an extremely thin active region, typically hundreds of atomic layers. In this framework, III-V semiconductors, such as InAs and InSb, have record-breaking conversion efficiencies per unit thickness. In addition, the phase mismatch, which commonly limits the generation of terahertz from optical crystal, is negligible and so there is an opportunity for enhancing the emitted bandwidth.

My thesis is born as the core of many research interests of my research lab (Emergent Photonics), which enabled the appropriate availability of resources that made my results possible. It also created several spin-out research lines. All the work presented is my work (with the exception of the background research). Parts of chapters have been published in journals and publications which see me as the first author.

The structure of this thesis is as follows. First I discuss optical pump rectification emission, and the saturation of InAs terahertz emissions. Then I introduce my work on terahertz enhancement emission through graphene. Finally, I present my work on an exotic terahertz emission mechanism, namely the all-optical surface optical rectification and I place my concluding remarks.

Acknowledgements

First of all, I would like to thank my supervisors Marco Peccianti and Alessia Pasquazi for the all continued support and advice throughout the years. I am sincerely grateful for all the effort that you have both put into assisting me with my PhD.

I acknowledge all members of the Emergent Photonics lab, who have helped and assisted me throughout the years. In particular I would like to thank Jacob Tunesi and Juan Sebastian Totero Gongora for taking the effort to correct my mistakes (of which there have been many) and for being excellent people to work with.

To Andrew, Luigi and James all of whom have kept me sane while sharing an office and helping to make the many long days of office work bearable I want to say thank you.

The research leading to these results has received funding from the People Programme (Marie Curie Actions) of the European Union's Seventh Framework programme FP7/2007 2013 under REA grant agreement no. 630833 and [327627]. I acknowledge the support of the U.K. Quantum Technology Hub for Sensors and Metrology, EPSRC, under Grant EP/M013294/1. This research received funding from the European Union's Horizon 2020 research and innovation programme, grant agreement no 725046.

Finally to my family, Jennifer, and my friends with all your unconditional love and support it has really helped me become who I am today.

Contents

List of Tables

List of Figures

List of Abbreviations

AO-SOR All-Optical Surface Optical Rectification.

CP Calcite Plate.

CVD Chemical Vapour Deposition.

DFG Difference Frequency Generation.

DTEM Dynamic Terahertz Emission Microscope.

FFT Fast Fourier Transform.

GaAs Gallium Arsenide.

InAs Indium Arsenide.

InGaAs Indium Gallium Arsenide.

InSb Indium Antimonide.

IR Infrared.

KDP Potassium Dihydrogen Phosphate.

KPFM Kelvin Probe Force Microscopy.

LPE Liquid Phase Exfoliation.

LTEM Laser Terahertz Emission Microscope.

NMP N Methyl-Pyrrolidone.

OPRE Optical Pump Rectification Emission.

OPTP Optical Pump Terahertz Probe.

OR Optical Rectification.

RD Relative Density.

RMS Root Mean Square.

SFG Sum Frequency Generation.

SHG Second Harmonic Generation.

SOR Surface Optical Rectification.

TDS Time-Domain Spectroscopy.

THz Terahertz.

ZnTe Zinc Telluride.

List of Constants and Variables

$\boldsymbol{\lambda}$	Wavelength.
$\boldsymbol{V_{PD}}$	Photo-Dember voltage.
$\boldsymbol{k_B}$	Boltzmann constant.
$\boldsymbol{T}$	Temperature.
$\boldsymbol{b}$	Mobility ratio of the electrons and holes.
$\boldsymbol{\mu_e}$	Mobility of electrons.
$\boldsymbol{\mu_h}$	Mobility of holes.
$\boldsymbol{n_0}$	Initial density of electrons.
$\boldsymbol{h_0}$	Initial density of holes.
$\boldsymbol{e}$	Elementary charge.
$\boldsymbol{\Delta n}$	Change in number of electrons.
$\boldsymbol{\Delta E}$	Change in energy.
$\boldsymbol{T_e}$	Temperature of electrons.
$\boldsymbol{E_{PD}}$	Photo-Dember field.
$\boldsymbol{\alpha}$	Absorption depth.
$\boldsymbol{E_{SC}}$	Terahertz field generated from surge current.
$\boldsymbol{A}$	Exposed area.
$\boldsymbol{\tau}$	Duration of laser pulse.
$\boldsymbol{G}$	Generation rate of the photocarriers.
$\boldsymbol{N_D}$	Concentration of donor atoms.
$\boldsymbol{N_A}$	Concentration of acceptor atoms.
$\boldsymbol{c}$	Speed of light in vacuum.
$\boldsymbol{r}$	Distance.
$\boldsymbol{\epsilon_0}$	Permittivity of free space.
$\boldsymbol{\epsilon_r}$	Relative permittivity.
$\boldsymbol{W}$	Power of laser pulse.

$\boldsymbol{E_{PA}}$	Terahertz field generated from photoconductive antenna.
$\boldsymbol{J_S}$	Induced current.
$\boldsymbol{\omega}$	Frequency.
$\boldsymbol{P}$	Polarisation.
$\boldsymbol{\chi^{(1)}}$	Linear susceptibility.
$\boldsymbol{\chi^{(2)}}$	Second order nonlinear susceptibility.
$\boldsymbol{\chi^{(3)}}$	Third order nonlinear susceptibility.
$\boldsymbol{E_Z^{surf}}$	Surface depletion field.
$\boldsymbol{W_G}$	Energy of THz generating pump.
$\boldsymbol{W_S}$	Energy of the screening pump.
$\boldsymbol{\eta}$	Generation efficiency
$\boldsymbol{Q_{surf}}$	Total charge hosted by the surface states of a semiconductor.
$\boldsymbol{Q_{Sc}}$	Total charge in Schottky depletion region.
$\boldsymbol{Q_{Z_0}}$	Total charge in narrow accumulation region.
$\boldsymbol{n_Ph}$	Density of photo-electrons close to surface layer.
$\boldsymbol{P_T}$	Thermoelectric power.
$\boldsymbol{D_M}$	Electron diffusion coefficient.
$\boldsymbol{\tau_s}$	Delay of the screening pulse.
$\boldsymbol{\tau_{cp}}$	Delay induced by the calcite plate.
$\boldsymbol{t_d}$	Delay of optical probe.
$\boldsymbol{A}$	Maximum THz peak field.
$\boldsymbol{W_{sat}}$	Saturation energy.
$\boldsymbol{V_b}$	Electric potential in proximity to the surface.
$\boldsymbol{\phi}$	Angle of calcite plate.
$\boldsymbol{\varphi}$	Crystal rotation angle.
$\boldsymbol{E_{800}}$	Electric field at 800nm.
$\boldsymbol{E_{400}}$	Electric field at 400nm.
$\boldsymbol{A_s}$	Phase matching coefficient for s.
$\boldsymbol{F_{800}}$	Fresnel component at 800nm.
$\boldsymbol{F_{400}}$	Fresnel component at 400nm.
$\boldsymbol{t_{800}}$	Fresnel transmission coefficient at 800nm.
$\boldsymbol{t_{400}}$	Fresnel transmission coefficient at 400nm.
$\boldsymbol{L_{eff}}$	Effective length in the medium.

Chapter 1

Introduction

1.1 Introduction to Terahertz Radiation

Since the formation of the sun and the solar system roughly 4.5 billion years ago, the earth has been bathed with light and electromagnetic radiation. Since the beginning of mankind, we have strived to control light. The initial campfires used by our ancestors in their caves are a very early example of this. As mankind developed so has our ability to control light, we developed mirrors and lenses to divert and magnify the light. In the last century, we have gained access to light we can not see, and the study of different sections of the electromagnetic spectrum has become vital, producing very useful technological advances such as x-ray machines, microwave devices and radio. The current research into THz radiation can be seen under the same light: it will expand upon our knowledge of the electromagnetic spectrum we have strived to control.

In the electromagnetic spectrum the THz band conventionally occupies the region between the high-frequency edge of the microwave band, often conventionally indicated as 0.3 THz, and the low-frequency edge of the Infrared (IR) band, normally fixed by the state of the art mid-IR laser technologies as 10 THz. In terms of wavelength, this corresponds to a range between 0.03 mm to 1.00 mm. The THz gap encompasses the region that separates electronics and optics.

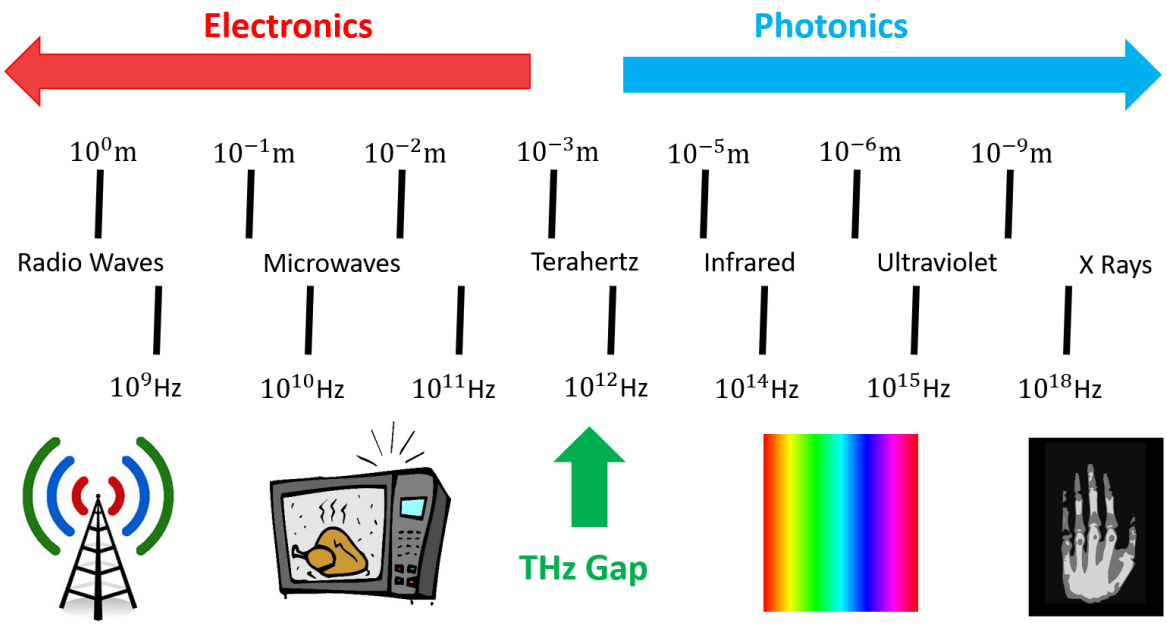

Figure 1.1: Diagram showing the electromagnetic spectrum along with the location of the THz gap and conventional uses of different parts of the electromagnetic spectrum.

The peculiar nature of the field-matter interactions induced by THz radiation makes it a formidable tool for investigation of the natural world. In a relevant example, many compounds possess very specific electromagnetic resonances, originating from their molecular structure, which lies in the THz region. This has been the main motivation behind the development of active spectroscopy in the THz domain, as opposed to optical spectroscopy. Optical spectroscopy is more sensitive to the nature of the atomic bonding but is less sensitive to molecular structure and arrangement of complex compounds: this is where THz spectroscopy excels. Amino acids, DNA and many bio-compounds are prominent examples. This and the extremely low energy (non-ionising) nature of THz photons, catalysed the specific interest of THz radiation for application in biological and medical fields.

From a historical perspective, investigations within the THz frequency range were restricted for a long time to niche scientific environments, such as synchrotron facilities and free electron lasers, with few relevant scientific applications due to the massively bulky nature and unwieldy cost of these facilities. The advent of THz science as an emerging domain can be certainly connected to the mainstream diffusion of cost-effective generation devices and techniques, which can be traced back to the demonstration of the first laser in 1960 by Theodore Maiman.

A few years later this revolution led to the first demonstration of mode-locked lasers [1] in 1964, which was indeed a significant enabling event in the THz science chronology. THz science has a long pre-THz era history (e.g. in astronomy and in synchrotron light investigation), pre-dating the introduction of the now widely diffused THz antenna in the 1980's [2, 3, 4, 5], the first demonstration of a THz pulse in 1971 (at the time defined as generation of far-IR radiation) [6], and even the first demonstration of the optical rectification process in 1962 [7]. Probably the first example of Time-Domain Spectroscopy (TDS) in the modern sense (a pivotal methodology in THz spectroscopy) can be attributed to Auston et al. [8]. Interestingly none of these dates can be exactly related to the emergence of THz science as recognised in modern times, whereas the most likely triggering event has been the cost-effectiveness and diffusion (and the availability of proper off the shelf components) of pulsed lasers achieved in the early 1990's.

In the current state of development, there is still a lack of accessible technologies in the THz frequency band; even basic processes such as imaging present hurdles and unsolved challenges. A significant number of scientific publications related to THz light appear regularly in every major optics journal. It is the peculiar fundamental and technical difficulty encountered in THz exploitation that brought the definition of a very specific and distinct scientific and engineering community investigating on this topic: in fact 'THz-Science' is now universally accepted as describing the overall kernel of this research endeavour.

1.2 Terahertz radiation and other disciplines

Today the application of THz technology is a key research and development subject in areas such as the semiconductor industry, biological and medical sciences, security, quality control of food and agricultural products, global environmental monitoring and ultrafast computing [9, 10].

There are a number of potential practical advantages which makes THz technologies very suitable for industrial applications. For example, THz waves can pass through many packaging materials, including paper, cardboard, plastics, certain kinds of glass and clothes without strong attenuation, revealing what is inside the package [11]. In terms of electromagnetic compatibility and radiation safety, THz waves are preferable than X-rays (which are often used for such purposes) as THz photons have an energy within the scale of a few meV (X-rays are within the order of 10 keV).

The applications where there is an urgent demand for a reliable THz analysis include, for example, fast analysis to monitor illegal materials (explosives and illicit drugs) [12, 13,

14, 15] for security checkpoints or for monitoring molecular composition and poly-morphs (molecules which have the same molecular composition but different lattice structures) in pharmaceutical products [16]. Here, the THz capability of discriminating structural differences between similar compounds promises many on-field application breakthroughs. Due to recent developments in the field of sources and detectors, THz technology has been associated with a rapidly increasing list of potential applications [9] in fields as different as life sciences and security. THz imaging has been investigated for shape identification in passenger and luggage imaging in airports [17].

The deployment of the technology on an industrial level is undoubtedly related to the diffusion of efficient sources and detectors. The last ten years have been marked by an increasing number of standard systems on the market, driven by progressively smaller ultrafast (femtosecond) lasers, capable of performing THz-TDS and forms of hyper-spectral imaging. When compared with similar devices and methodology performed in the optical domain, these THz tools are still primitive, bulky and unpractical. Nor do they possess the typical characteristic of mass diffused devices; such as high sensitivity, integrability and scalability. However, it is undoubtedly true that these are the first tangible examples of end-user applications which is a common landmark of a maturing research field.

1.3 Terahertz Time-Domain Spectroscopy (TDS)

Although TDS is not a concept that can be exclusively related to THz radiation, it has certainly been a defining element in its investigation. As such, it is a fundamental element of the research pursued within this thesis. This methodology is capable of exactly reconstructing the whole temporal evolution of the electric field of a THz pulse. It is perhaps the most comprehensive form of coherent detection for an electromagnetic pulse. In THz-TDS, a pulsed THz wave is emitted from a source and is then detected by sampling its electric field at different instants of its evolution in time [8, 18]. This can be performed by specific devices known as photoconductive switches or by exploiting nonlinear interactions occurring between the THz wave and an optical pulse in different media (e.g. a crystal or gas). In all these embodiments, an ultrashort optical laser pulse is used to generate the THz wave and a replica of the optical pulse, the probe, is exploited for this "electro-optical sampling." The THz pulse is reconstructed, by delaying the THz wave with respect to the probe pulse. The specific details of electro=optical sampling are covered in later paragraphs.

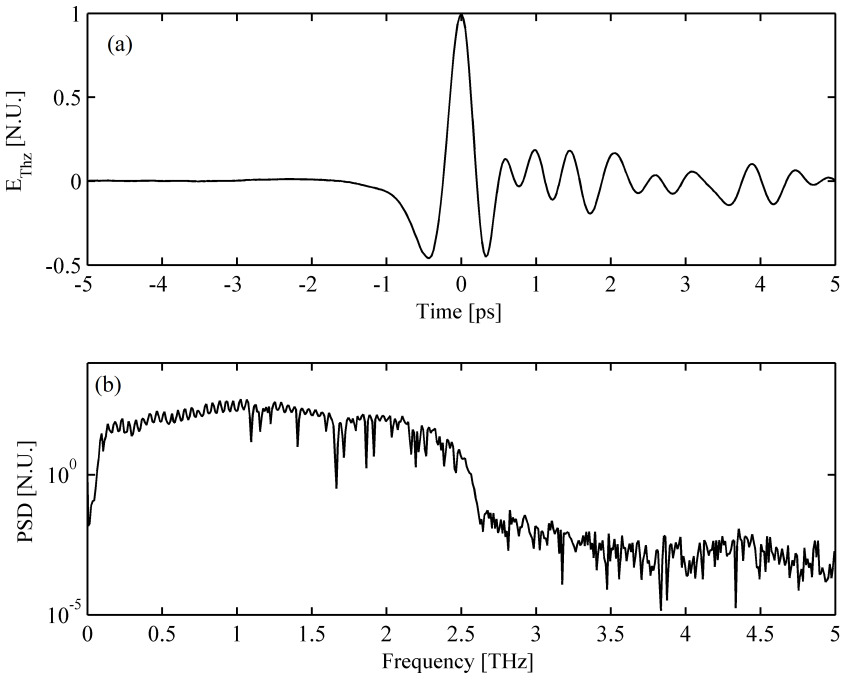

Figure 1.2: (a) A typical THz-TDS reference pulse generated and detected using a Zinc Telluride crystal (ZnTe). (b) The spectrum of the above pulse, calculated using a Fourier transform.

The reconstruction of the temporal evolution of the THz pulse electric field is probably the most disruptive element in the domain. An example of a waveform retrieved from a typical THz-TDS system is shown in Fig. 1.2. The most striking feature of the TDS is that as the full temporal field evolution becomes available, so too does its full complex spectrum, as opposed to optical spectroscopy where only the power spectral density of the field is normally available (without resorting to much more complex and field-specific methodologies). In practical terms, this means that the spectrum of electromagnetic delay (which commonly represents the refractive index spectrum of a medium) is a directly measurable quantity.

In addition, in a way conceptually similar to modern ultrasound imaging, time-of-flight imaging with THz pulses is possible and allows for a three-dimensional reconstruction of transparent and semi-transparent objects. This technique has been successfully used to retrieve the signature of Goya from the inner layers of one of his paintings [19] as shown in Fig. 1.3.

A very common experimental implementation of THz-TDS is presented in Fig. 1.4. The optical beam is split into two components, the optical pump pulse illuminates the

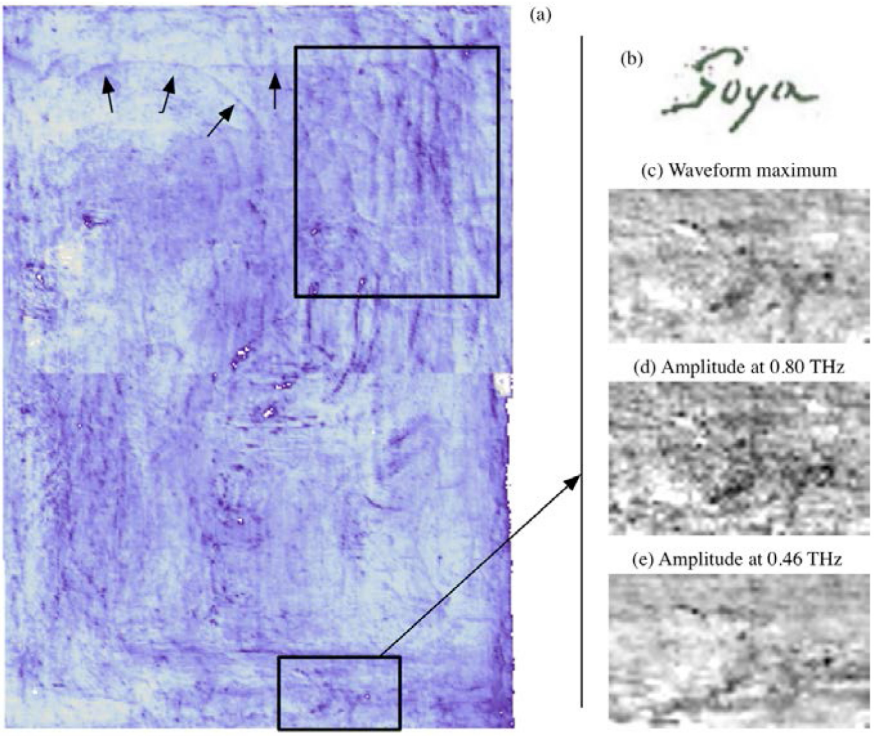

Figure 1.3: (a) Structural features in the THz image and signature area. (b) Known signature of the artist. (c) Alleged signature resulting from finding the maximum amplitude in the time-domain data. (d) Image of the alleged signature in the frequency domain at 0.8 THz. (e) Image of the same area in the frequency domain at 0.46 THz in which the alleged signature is not visible due to larger wavelength than that corresponding to 0.8 THz.

emitter and generates the THz pulse, this pulse then travels through free space before focusing on the detector. The delay of the second component can be controlled by a mechanical stage and acts as the delay for the probe pulse. A nonlinear crystal is exploited to use the THz wave to induce a rotation of the polarisation state of the optical probe. Such a rotation can be detected by a polarisation discriminator and allows direct estimation of the THz electric field at each delay. A Fast Fourier Transform (FFT) can be used to reconstruct the THz spectrum. In the next section, an overview of the most common generation and coherent detection approach is presented. In this specific framework, it is important to stress that the field is still immature. Although, some technologies and principles can be considered established (e.g. the THz antenna emission and detection), others are still reaching, or only recently reached a self-consistent physical description (e.g. the two-colour plasma THz emission).

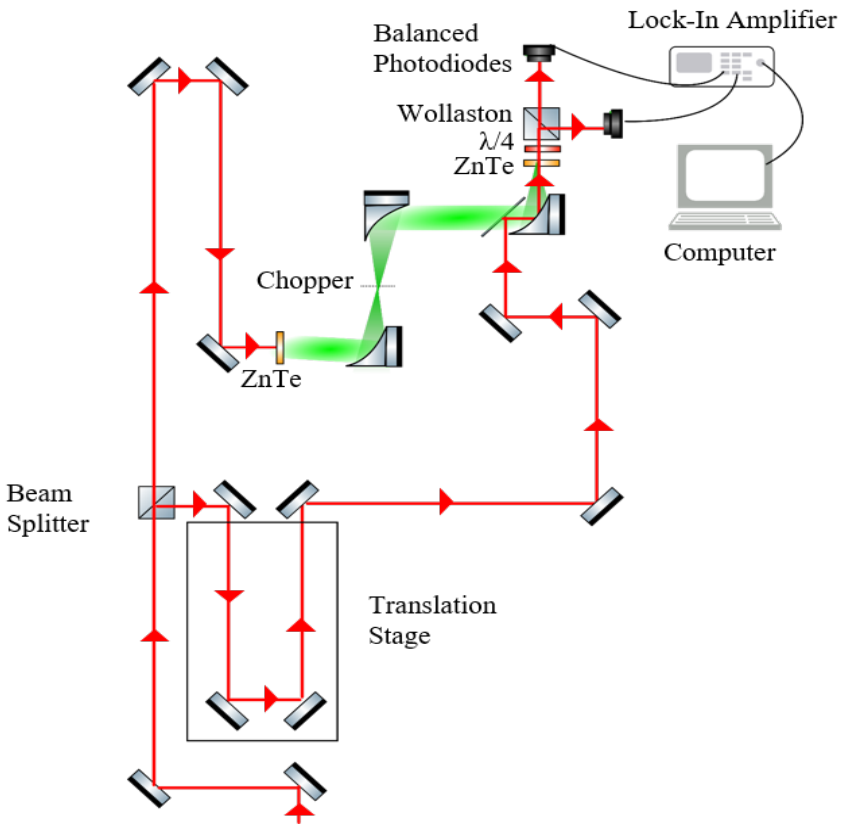

Figure 1.4: Experimental setup for a typical embodiment of a THz-TDS based on nonlinear optical conversion. The red beam path denotes the 800 nm optical beam path, while the green beam path denotes the THz emission. The optical beam is split into a generation and probe beam using a beamsplitter. The optical pump pulse illuminates the emitter (ZnTe in the figure) and generates the THz pulse, this pulse then travels through free space before being focused on the detector. The delay of the probe is controlled by a translation stage. A nonlinear crystal (ZnTe) is exploited to use the THz wave to induce a rotation of the polarisation state of the optical probe. Such a rotation can be detected by a combination of a $\frac{\lambda}{4}$ waveplate, a Wollaston prism and a pair of balanced photodiodes. An optical chopper and a lock-in amplifier are used to enhance the signal to noise ratio of the detection.

1.4 Generation of Terahertz radiation

In a general definition, the most common approaches to the generation of a THz pulse requires a nonlinear conversion of an ultrafast optical field into THz photons. However, in light of the large fundamental differences in the physical descriptions of these approaches, there is a general distinction between generation and detection mechanisms based on photo-carrier excitation, where the THz source is a current transient mediated by photo-

induced carriers upon optical excitation [20, 21], and methods that exploit nonlinear interactions between optical photons that are not mediated by photoexcited carriers. This is not the only possible classification, others being based on the non-perturbative nature of the nonlinearity, others that classify the generation and detection on the base of whether or not the energy of the THz wave is actually provided by the impinging optical field or by a third source (e.g. the DC field in a THz photo-conductive emitter). In the framework of this thesis, we will choose a classification based on the involvement (or not) of photo-excited carriers in the ruling model of the generation, operating an ad-hoc distinction where this classification is not sufficient to capture peculiar features of the generation mechanism.

1.4.1 Photo-carrier related emissions

When a femtosecond optical beam strikes the surface of a semiconductor, and the photon energy exceeds that of the band gap, electron-hole pairs are generated on time scales that can be considered instantaneous at optical frequencies. In such a scenario, a transient current, induced by an increased conductivity, may then develop for a number of different possible physical reasons. More generally, when the excitation is ultrashort a number of burst-current source mechanisms exist in many different materials.

Photo-Dember emission

The photo-Dember emission is a photo-carrier based THz-emission mechanism which occurs in bulk or semiconductor films [22]. It arises from the different mobilities of holes and electrons within a semiconductor [23, 24, 25, 21, 26, 27, 28, 29, 30]. In a simplified description, an ultrashort optical pulse excites the medium, generating carriers on the surface. As the carriers can not diffuse through the boundary of the semiconductor, they diffuse into the bulk. The difference in mobilities between the electrons and holes is responsible for a carrier spatial imbalance which generates a dipole whose direction is normal to the surface of the material. In the state of the art, the general potential unbalance normal to the surface and can be reduced to the following [31]

$$V_{PD} = \frac{k_B T}{e} \frac{b-1}{b+1} \ln(1 + \frac{(b+1)\Delta n}{n_0 b + h_0}). \tag{1.1}$$

b represents the mobility ratio ($b = \mu_e/\mu_h$) of the electrons (μ_e) and holes (μ_h). n_0 and h_0 are the initial density of electrons and holes. T is the temperature of the photoexcited electrons and holes. Electron excess energies, with respect to the band-gap, also enhance

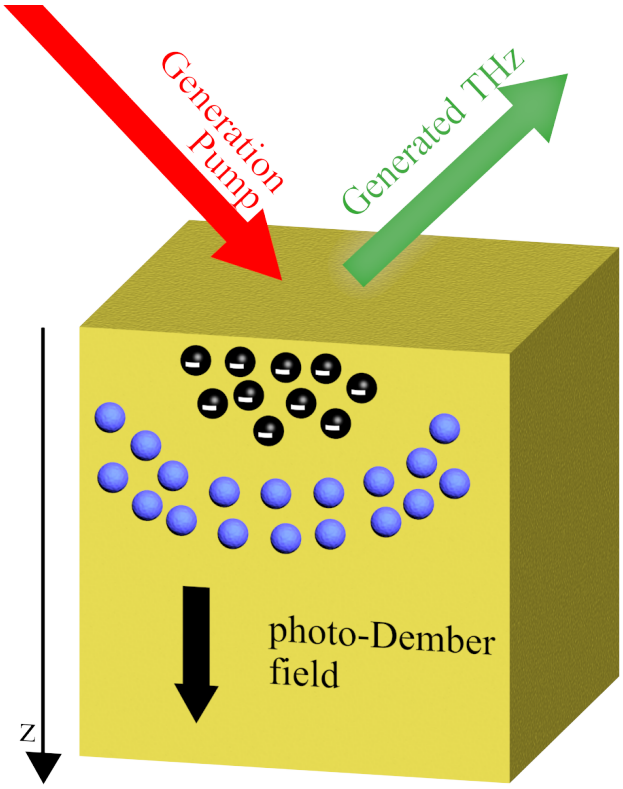

Figure 1.5: A schematic of photo-Dember THz emission, in which an optical pump generates electron-hole pairs, and the difference in mobilities causes a photo-Dember field to arise.

the photo-Dember effect. For these reasons narrow band-gap semiconductors (such as InAs (Indium Arsenide) and Indium Antimonide (InSb)) can exhibit a significant photo-Dember emission. The photo-Dember emission is then stronger in narrow band-gap semiconductors due to the thin absorption depth. The emitted THz electric field from the photo-Dember effect E_{PD} is related to the photo-Dember Voltage through the absorption depth α.

$$E_{PD} = \frac{V_{PD}}{\alpha}. \tag{1.2}$$

For the same wavelength, InSb had a shorter penetration depth than that of InAs, 92 nm and 142 nm respectively, and has a higher value for the ratio between the electron and hole mobilities, 125 and 95 respectively. Therefore from Eq. 1.2 it could be expected that a photo-Dember field has nearly four times the magnitude than that of InAs and would, therefore be sixteen times greater in power. However, this was shown experimentally to not be the case [27]. This unexpectedly low emission can be attributed to a reduction of the

transient mobility as a result of intervalley scattering of electrons to the L valley [21, 32], where the electron mobility is considerably lower. As the intervalley scattering typically relies very "hot" electrons the photo-Dember emission from InSb can be increased six-fold by migrating to higher wavelengths [33], which is surprising considering the detrimental effect of the long penetration depth at higher wavelengths.

Surge Current

Surge current emission (also referred to as surface field emission and drift-diffusion emission) has many analogies with the photo-Dember effect. However, the transient current develops as a result of the photo-generated carriers being accelerated by a surface electric-field typically present across the surface of many semiconductors [34, 28, 35, 36, 37]. Surge current emissions are essentially sourced by the depletion field of the semiconductor.

In wide band-gap semiconductors (such as Gallium Arsenide (GaAs)) the population of the surface states induce pinning of the Fermi level at the surface. This results in band bending and the formation of a depletion region where a surface field exists. When the semiconductor surface is excited by an ultrashort laser pulse, electron-hole pairs are created. Due to the presence of the surface field, the electrons and holes are accelerated in opposite directions resulting in a surge current perpendicular to the semiconductor surface. The dopants and impurities of the semiconductor influence the direction and magnitude of the surface depletion such that, in most cases, an n-type semiconductor drives the photogenerated carriers in the opposite direction to that of a p-type semiconductor. This reversal of the surge current direction causes a polarity reversal of the generated THz waveform between semiconductors of different doping types [38]. The generated THz field in the far field is described by Eq. 1.3 [39]

$$E_{SC} = \frac{Ae^2\mu_e G|N_D - N_A|}{4\pi\epsilon_0^2\epsilon_r c^3 \tau r \alpha^2}[W\alpha - 1 + e^{-\alpha W}], \tag{1.3}$$

where S represents the laser focal spot size, τ is the duration of the laser pulse, r is the distance in the far field. G is generation rate of the photocarriers. ϵ_R is the relative permittivity of the semiconductor.

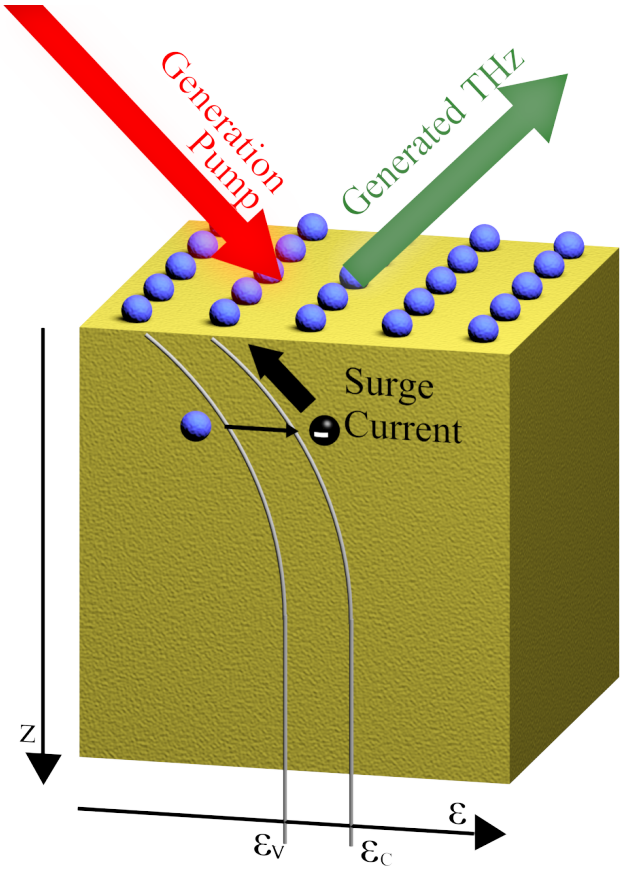

Figure 1.6: A schematic of surge current THz emission, in which an optical pump generates electron-hole pairs, and the surface field causes photo-generated carriers to be accelerated giving rise to a transient current.

Photoconductive Antenna

A photoconductive antenna comprises two biased electrodes separated by a small semiconductor gap. When the gap is exposed to light, an increase in the electrical conductivity of the semiconductor is observed. When the photoconductive antenna is illuminated with a femtosecond laser pulse, the resulting transient current generates THz radiation. A THz emitter based on a photoconductive antenna is constructed of two metal electrodes deposited upon a semiconductor. The impinging laser pulse must have a photon energy larger than the material energy-bandgap, in order to promote the generation of free electron-hole pairs. The bias field, applied by the electrodes, accelerates the free carriers.

Let's assume that the emitted THz field is a Hertzian dipole antenna, with arms much smaller than the wavelength of the emitted radiation. Under this hypothesis, the emitted THz field in the far field region is governed by Eq. 1.4.

$$E_{PA} = -\frac{A}{4\pi\varepsilon_0 c^2} J_s \tag{1.4}$$

Where A is the exposed area, r is the distance between the observation and the centre of the aperture, and J_s is the induced current. The output electric field of a photoconductive antenna depends on two key factors: the bias voltage, and the optical pump power. When both the optical power and bias voltage are sufficiently low, the amplitude of the electric field of the THz radiation is linearly proportional to both parameters. At high optical powers the screening effect, induced by the large photocarrier density causes saturation of the THz field emission.

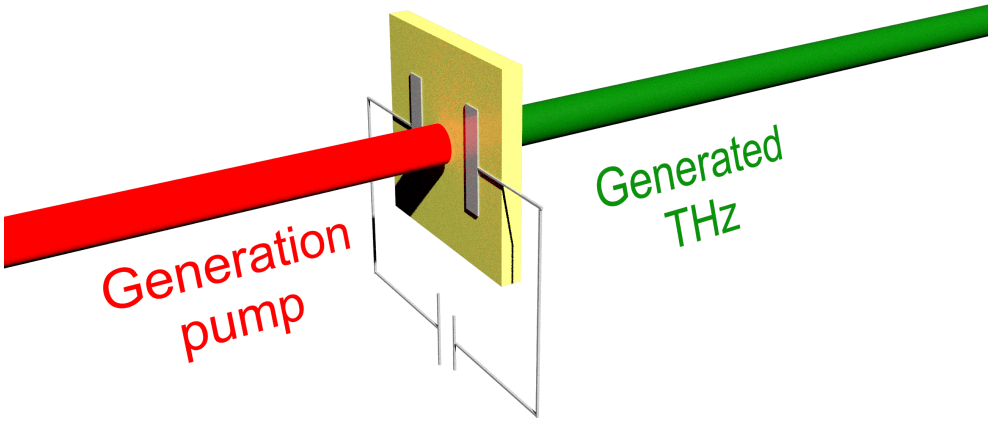

Figure 1.7: A schematic of photoconductive antenna emission, in which an optical pump excites a semiconductor. A DC bias is applied to the semiconductor via two metal electrodes resulting in an acceleration of the optically excited free carriers, resulting in THz emission.

1.4.2 Nonlinear field-matter interactions

On an atomic scale, a simplistic description of an interaction between a wave and an atom is that the electromagnetic wave acts as an applied electric field, causing a displacement of the electronic cloud of electrons surrounding the nucleus. On a macroscopic scale, a material is made up of N atoms, all of which act as N identical dipoles, the material exhibits an average dipole density N, which is the source of the electromagnetic polarisation. The classical modelling route describes the system as a classical anharmonic oscillator (assuming a perturbative anharmonic behaviour). In an anharmonic oscillator, the electron displacement is not proportional to the applied field. Translated in terms of electric polarisation, this means that the harmonic content of the polarisation differs from the harmonic content of the excitation.

In the perturbative analysis, it is convenient to express the excitation as a superposition of monochromatic components at different frequencies. In light of the nonlinear field-matter interaction, the polarisation may contain several distinguishable components, each oscillating at a frequency which is a combination of the frequencies of the excitation components. It is usual (and convenient) to identify each specific frequency mixing with a specific process name (e.g. sum frequency, difference frequency etc.).

In nonlinear optics the generalised model of the field polarisation can be expressed as a power series of the nonlinear perturbation:

$$\begin{aligned} P(t) &= \epsilon_0[\chi^{(1)}E(t) + \chi^{(2)}E^2(t) + \chi^{(3)}E^3(t) + ...] \\ &\equiv P^{(1)}(t) + P^{(2)}(t) + P^{(3)}(t) + ... \end{aligned} \tag{1.5}$$

Where $\chi^{(2)}$ and $\chi^{(3)}$ are the second and third order nonlinear optical susceptibilities, $P^{(2)}$ and $P^{(3)}$ represent the second and third order contribution to the nonlinear polarisation. For simplicity P(t) and E(t) have been assumed to be scalar properties, in the case of treating with the vector properties of the fields $\chi^{(2)}$ becomes a third rank tensor, $\chi^{(3)}$ becomes a fourth rank tensor and so on. It should also be noted that many materials, such as crystals and glasses, display inversion symmetry and as such $\chi^{(2)}$ vanishes for such media.

Now the sum and difference frequency generation will be briefly described. If we consider a second order nonlinear medium, with two impinging optical fields with two frequency components. The optical field has the form of,

$$E(t) = E_1 e^{-i\omega_1 t} + E_2 e^{-i\omega_2 t} + C.C., \tag{1.6}$$

by inputting Eq. 1.6 into the second order nonlinear polarisation component of Eq. 1.5, It is found that the nonlinear polarisation is given by

$$\begin{aligned} P^{(2)}(t) = \epsilon_0\chi^{(2)}[&E_1^2 e^{-2i\omega_1 t} + E_2^2 e^{-2i\omega_2 t} + 2E_1E_2e^{-i(\omega_1+\omega_2)t} \\ &+2E_1E_2^* e^{-i(\omega_1-\omega_2)t} + c.c.] + 2\epsilon_0\chi^{(2)}[E_1E_1^* + E_2E_2^*]. \end{aligned} \tag{1.7}$$

If the nonlinear polarisation is expressed as the following notation,

$$P^{(2)} = \sum_n P(\omega_n)e^{-i\omega_n t}. \tag{1.8}$$

This allows for Eq. 1.7 to be expressed in terms of the various frequency components of the nonlinear polarisation, where each of the individual expressions describes a separate

second order nonlinear physical process. Eq. 1.9 shows each of the terms, as well as a caption for the process it describes where the processes have the following names Second Harmonic Generation (SHG), Sum Frequency Generation (SFG), Difference Frequency Generation (DFG) and OR.

$$\begin{aligned} P(2\omega_1) &= \epsilon_0 \chi^{(2)} E_1^2 \ (SHG). \\ P(2\omega_2) &= \epsilon_0 \chi^{(2)} E_2^2 \ (SHG). \\ P(\omega_1 + \omega_2) &= 2\epsilon_0 \chi^{(2)} E_1 E_2 \ (SFG). \\ P(\omega_1 - \omega_2) &= 2\epsilon_0 \chi^{(2)} E_1 E_2^* \ (DFG). \\ P(0) &= 2\epsilon_0 \chi^{(2)} (E_1 E_1^* + E_2 E_2^*) \ (OR). \end{aligned} \tag{1.9}$$

Although Eq. 1.9 describes several processes, in most practical cases, other conditions such as the velocity matching between the different field components and the transparency of the medium make only a single process relevant.

Optical Rectification

Optical rectification was first reported by Bass et al. in 1962 [7]: in which a DC polarisation was observed by illuminating Potassium Dihydrogen Phosphate (KDP) crystals with an intense ruby laser. In a broader sense, we talk of OR even in the case of a non-monochromatic excitation, like the one provided by ultrafast femtosecond lasers. Due to the inherently large bandwidth of an exciting femtosecond pulse (within the THz scale), the resulting polarisation assumes the form of a short few-cycle pulse with a spectrum continuously spanning a significant portion of the THz band. For a femtosecond pulse, the THz field is actually the second order derivative of the pulse envelope.

Although the bandwidth of the THz pulse is dependant on the pulse width of the laser pulse there are some limiting factors. For an ideal situation of optical rectification, the optical generation pump and the THz pulse would co-propagate through the nonlinear crystal, however, for most materials, the refractive index of the generation pump and the THz pulse are not equal. Specifically, the phase matching condition for THz emission requires that the group velocity of the femtosecond pulse matches the phase velocity of the THz pulse. This requirement stems from the fact that the THz wave is the second derivative of the pulse envelope. This phase mismatch results in destructive interference reducing the effective THz radiation generated. The length of material the generation is feasible over before destructive interference occurs is referred to as the materials coherence length. This difference in this phase mismatch is highlighted in Fig. 1.8, in which the group

index for 800 nm is shown against the index of refraction for ZnTe over a range of THz wavelengths. The data used for this graph was taken from [40] for the THz, and [41] for the 800 nm. In addition, most nonlinear crystals also suffer from holes in the emitted THz spectrum due to phonon resonances. Typically, these resonances lie somewhere between 5-10 THz, as the length of the material is increased the spectral hole due to the phonon resonance will widen, resulting in a narrower THz emission spectra. It should be noted that currently there is no known material that exists with ideal co-linear propagation, it is quite incidental luck that phase matching can be realised for a ZnTe crystal with a ⟨100⟩ cut for a wavelength of 800 nm, which happens to be the peak efficiency wavelength for a Ti:Sa femtosecond oscillator, this coincidence is the reason for the popularity of ZnTe crystals in THz nonlinear generation.

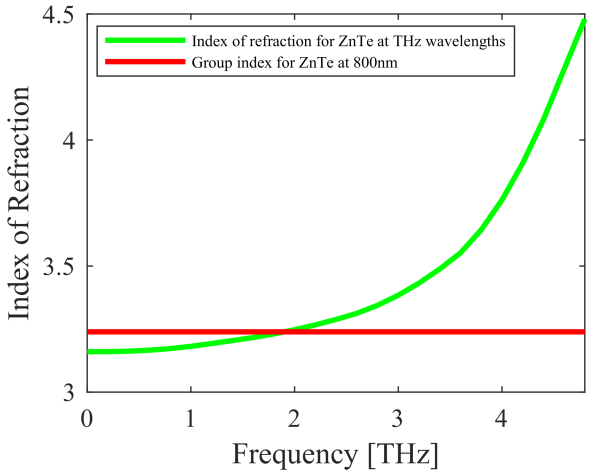

Figure 1.8: The index of refraction for ZnTe across a range of THz frequencies (green), shown against the group index of ZnTe at 800 nm (red).

Surface optical rectification (SOR)

In the early 90s, it has been demonstrated that significant THz pulse emissions could be obtained from a specific nonlinear rectification process occurring at the surface of semiconductor materials [42]. The underlying principle of SOR relies on the symmetry breaking static surface depletion field $E = E_Z^{surf}$ which is present in several semiconductors in light of the polarisation of the surface states. Like any optical field-induced second order nonlinearity, this process relies on the cubic nonlinear properties of the material, hence it is generally present regardless of the centrosymmetric nature of the medium (or the lack of). As such SOR exhibits unique physics when compared to bulk quadratic-optical rectification.

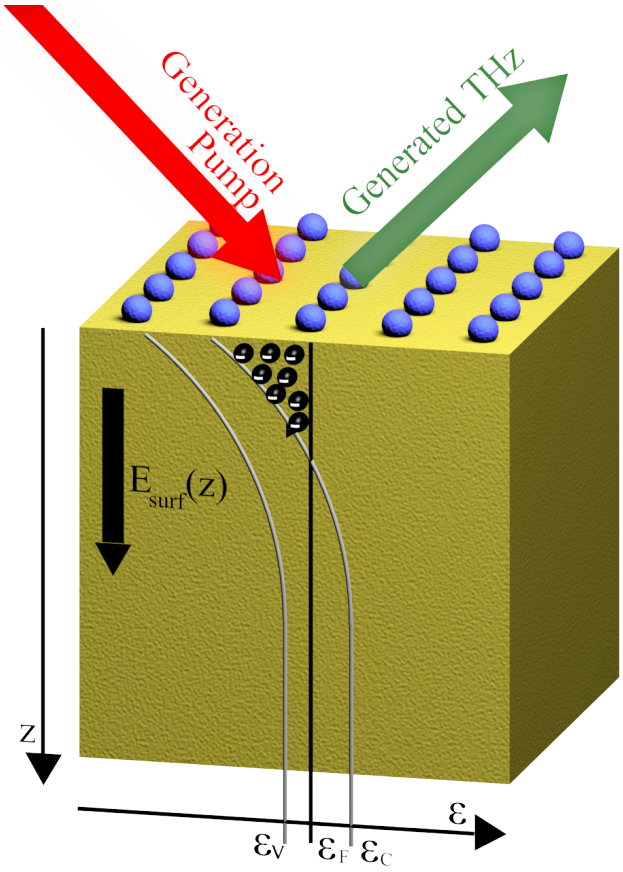

Figure 1.9: A schematic showing SOR emission. An ultrashort optical pulse excites a semiconductor surface, generating free electron-hole pairs within the optical skin depth. Band diagrams along the depth direction z, with the valence and conducting energies ε_v and ε_c are indicated in both cases. The surface field E_Z^{surf} is indicated, resulting from the balancing of the surface charges (plus signs on the top) and localised free-electrons in the surface accumulation region and the spatial charge in the depleted region. Free-electrons in the conduction band are indicated by black dots with minus signs, while ε_F indicates the Fermi level. The THz is generated by the interaction of the generation pump with the surface field.

The surface field E_Z^{surf} is directed along the normal of the surface $\hat{z}$. The nonlinear surface polarisation $\boldsymbol{P}_{THz}$ responsible for the emission of the quasi-static THz field with frequency $\omega_{THz} << \omega$ can be described as

$$\boldsymbol{P}_{THz} = \chi^{(3)}(\omega_{THz} : -\omega; \omega, 0) : \boldsymbol{E}(-\omega) : \boldsymbol{E}(\omega) : E_Z^{surf}(0)\hat{\boldsymbol{Z}}, \tag{1.10}$$

with $\chi^{(3)}$ being the third order nonlinear susceptibility tensor. The surface then behaves effectively as a second order nonlinear material [43]. We can define the effective quadratic

nonlinear susceptibility tensor $\chi^{(2)}$ as

$$\chi^{(2)}(\omega_{THz} : -\omega; \omega) = E_Z^{surf}(0)\chi^{(3)}(\omega_{THz} : -\omega; \omega, 0). \tag{1.11}$$

The effective nonlinear coefficient is then directly proportional to the surface field of the generating surface. The THz wave is generated by standard second order optical rectification [44] as described in the previous section. It is worth noting that in light of the typical thinness of the surface field region in many semiconductors, the velocity mismatch between the THz waves and optical pulse does not play a significant role in the SOR. In addition, although the absolute THz conversion is significantly below the common benchmarks fixed by nonlinear optical crystals, the SOR is generally driven by an extremely high nonlinear coefficient, which makes surface emission of macroscopic importance.

1.5 Detection of Terahertz radiation

Currently, there are three key methods used to detect pulsed THz radiation, these are electro-optic sampling, photoconductive antenna detection and air break-down coherent detection. It is worth noting that the detection performed using photoconductive antennas can be in principle assimilated to electro-optic sampling (and is done so in a number of publications). However, within the framework of this thesis, we will separate its description in light of the different physical mechanism when compared to the nonlinear electro-optic sampling based upon the Pockels effect. In the following section, a basic description of these methodologies is provided.

1.5.1 Electro-Optic Sampling

Electro-Optic (EO) is a methodology that samples the value of a propagating electric field, in a specific location, at a specific time. The key mechanism to EO sampling relies on the Pockels effect. In a nonlinear material, a static electric field will induce a change in birefringence. This change in birefringence is proportional to the amplitude of the applied electromagnetic field.

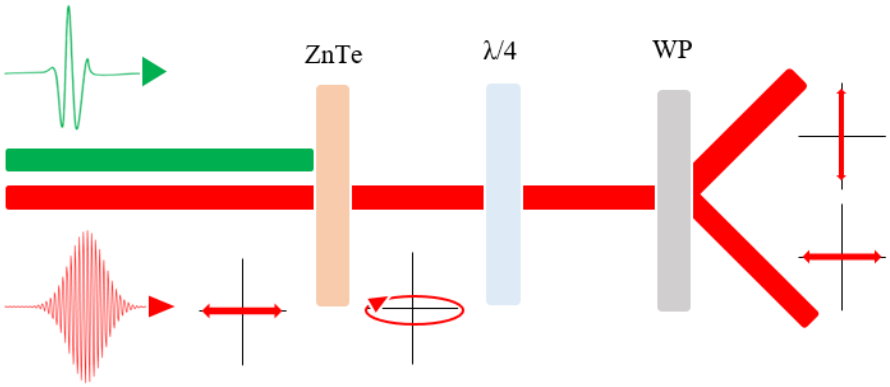

Figure 1.10: A schematic for electro-optic sampling, in which a THz pulse and an ultrashort optical pulse co-propagate through a nonlinear crystal. The THz pulse induces a change in polarisation on the optical pulse, resulting in an elliptical pulse. The optical pulse subsequently propagates through a $\lambda/4$ waveplate and a Wollaston prism, splitting the pulse into its linear polarisation components, the pulse is then detected with a pair of balanced photodiodes.

Fig. 1.10 shows a typical setup used to measure birefringence for electro-optic sampling. A linearly polarised optical probe pulse and the THz pulse propagate together through the EO crystal. The THz field induces a change in the refractive index ellipsoid of the ZnTe (or similar nonlinear crystal). This induced a birefringence which rotates the optical probe pulse polarisation which makes the probe pulse slightly elliptical in polarisation. The probe pulse then passes through a $\frac{\lambda}{4}$ waveplate which is used to map the two circularly polarised components of the field into two linearly polarised components. The probe pulse is then split into its two orthogonal components by a Wollaston prism. These two orthogonal components are then directed to a pair of balanced photodiodes. The photodiodes will measure the intensity difference between the two orthogonal components, this difference is proportional to the amplitude of the applied THz field. When there is no THz field applied the output is a linear polarisation that can be described as the superposition of equally powered circularly polarised components. As such, both photodiodes will detect the same signal and the differential signal is zero. The THz field applied rotates the polarisation creating an imbalance in the photodiodes proportional to the polarisation and the applied THz field. Hence the differential signal of the balanced photodiodes can be interpreted as proportional to the sampled THz field.

Electro-optic sampling suffers from the same problems as optical rectification, in that

the spectrum of the THz radiation detected is clipped by both the phonon processes of the crystal and the coherence length, limiting the effective bandwidth.

1.5.2 Photoconductive Antenna Detection

When a photoconductive antenna is used to detect a THz field, a femtosecond optical pulse induces a high photocarrier density between two electrodes (normally the two internal ends of a Hertzian-antenna structure. An impinging THz field induces drift of the photocarriers between the electrodes. As the femtosecond pulse overlaps with a specific section of the THz pulse, overall the antenna behaves as the generator of a current that can flow in an external connection that connects the two electrodes.

If the photocarrier lifetime is sufficiently low, the conductivity perturbation has a duration much shorter than the THz wavelength. In a very similar to nonlinear electro-optic sampling, the antenna samples the THz field. Measuring the photocurrent at different time delays between the optical pulse and THz pulse allows for the reconstruction of the THz pulse. As the photocurrent is extremely small (typically between femtoamperes and picoamperes), a lock-in detection approach is commonly used to enhance the signal to noise ratio.

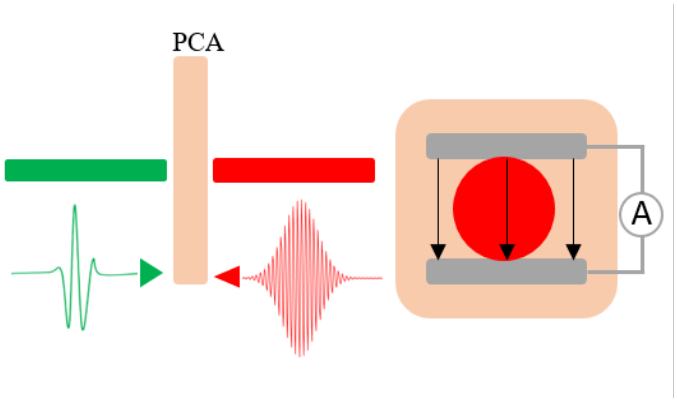

Figure 1.11: A schematic showing photoconductive antenna detection, in which an optical probe beam and a THz pulse simultaneously excite a gap between two biased electrodes, generating a photocurrent.

The detected photocurrent depends on the THz field and also on the surface conductivity of the material used to construct the antenna. An equation for the photocurrent, as a function of time, where σ_s is the finite relaxation time of the conductivity is shown in Eq. 1.12

$$J_s(t) = \int_{-\infty}^{t} \sigma_s(t - t')E_{THz}(t')dt'. \tag{1.12}$$

As a result, the finite relaxation time of the conductivity, induced by the photocarrier lifetime, actually 'smears' out the sampling of the THz field. By performing a Fourier transformation on Eq. 1.12 we can clearly appreciate that this behaviour corresponds to a low-pass filtering of the impinging THz spectrum, limiting the detection bandwidth. In fact, most of the recent research on photo-conductive switches focuses on the identification of substrates with extremely fast recombination times to overcome this limit.

1.6 Current Challenges in the field

Perhaps the most important limiting factor in the diffusion of ultrafast THz technologies is the lack of efficiency of the THz generation, and the fact that most of these generation approaches cannot be easily scaled-up to increase the output: mild improvements in the generation output usually require disproportionate technical efforts. Standard generation techniques exhibit an optical-to-THz conversion efficiency within the range 10^{-5} - 10^{-4}. It should be noted that although efficiencies above 1% have been reported they have been usually achieved with very important compromises in terms of generation bandwidth. Pulsed femtosecond lasers with energy in the mJ scale (with peak powers in the order of 10 GW) can be used to generate relatively bright THz pulses with energy within the scale of 0.1μJ-1μJ. This scenario is quite independent of the inherent generation process used. The cost of the technology exponentially increases with the desired THz power. There are also a few current issues in the detection of THz waves, for example, an electro-optic sampling setup is bulky and expensive as a nonlinear crystal, waveplate and polarising beamsplitter are required.

The standard apparatus for THz-TDS is the photoconductive antenna, however, they face a huge technological challenge in cost-effective large-scale production viability. GaAs (or Indium Gallium Arsenide (InGaAs)) is the most widely used materials for photoconductive devices, but the fabrication has two major disadvantages first, the semiconductor properties are difficult to reproduce, even when grown with the same reactor conditions. Secondly, the growth of these semiconductors is performed in molecular-beam-epitaxy machines, which is a very expensive machine for large-scale production of THz devices.

The search for a wider bandwidth in generation and detection is another obvious challenge in modern THz science. Although a TDS with more than 100 THz of bandwidth have been demonstrated via laser plasma generation and Air-based detection, these examples are of scarce practical impact, in light of the cost of the system and the several practical complications in their uses. Velocity mismatch limits the continuous spectrum available

from the crystals, although in a limited fashion different crystals can be used to explore different spectral regions. In a semiconductor, the recombination time and electrical time-constant appear to be a hard limit for exploring a wider bandwidth. It is worth noting that although the surface THz generation is potentially impacted by a similar bandwidth issue, there are several indications that specific surface generation approaches could enable an agile access to a much wider bandwidth.

1.7 This Thesis

With the massive advantages of THz radiations and the current technical difficulties in mind, I chose to undertake research into THz surface phenomena, which is the focal point of this thesis. III-V semiconductors, such as InAs and InSb, have world record-breaking conversion efficiencies per unit thickness due to their extremely thin active region, typically hundreds of atomic layers. In addition, as the active regions are very thin, the phase mismatch is negligible and so there is an opportunity for much wider bandwidths.

This thesis is born as the focal point of many research interests of my research lab (Emergent Photonics Lab), which enabled the appropriate availability of resources that made my results possible. All the work presented in my thesis is my work. Parts of chapters have been published in journals. I significantly contributed to the writing of the articles.

The structure of this thesis is as follows, In chapter 2 I will introduce Optical Pump Rectification Emission, and the utilisation of this technique to probe the surface dynamics of semiconductors. In chapter 3, building upon the work of chapter 2 I will use Optical Pump Rectification Emission to expose the saturation mechanisms within surface optical rectification. In chapter 4 I will demonstrate the enhancement of the surface field by the addition of Graphene flakes. This work results in the overcoming of the saturation limits of surface optical rectification. In Chapter 5 I will demonstrate my most recent spin-off investigation into a new generation mechanism, known as All-Optical Surface Optical Rectification. In chapter 6 I will place my conclusion, and provide an educated glimpse into the future of this work and my future-self as a scientist.

Chapter 2

Optical Pump Rectification Emission

The contents of this chapter have been published in [45]. I introduce a method for the diagnostics of electric surface potentials of a semiconductor based on THz surface generation. In this scheme, that was named Optical Pump Rectification Emission, a THz pulse is generated directly on the surface via SOR, utilising an ultrashort pulse, during which the DC surface potential is screened with a second optical pump pulse. As the THz generation directly relates to the surface potential arising from the surface states, the temporal dynamics of the static surface field induced by the screening effect of the photo-carriers can be observed. Such an approach is potentially insensitive to bulk carrier dynamics and does not require special illumination geometries.

2.1 Introduction

The diagnostics of electric surface potentials in semiconductors, arising as a result of the charged states at the surface of the material, together with the measurement of the dynamics of the surface carriers, has been at the heart of the development of many modern technologies [31]. In particular, in semiconductor technology, the map of surface carrier dynamics is of paramount importance in a number of industrial steps; for example, it is well established that the surface states strongly influence the potential of Schottky junctions [46]. Many rising technologies, such as photovoltaics and tuneable metamaterials, rely on thin-layer semiconductors and surface engineering [47, 48] requiring fast and in-situ monitoring of the surface properties, capable of evaluating the dynamics of carriers and static potentials at the surface. There are several ways (e.g. surface-tunnelling mi-

croscopy [49, 50]) to investigate the nature of surface potentials. Optical approaches have been largely investigated as effective, non-contact alternatives, particularly suitable when ultrafast dynamics need to be reconstructed. In these scenarios, the THz electromagnetic radiation, lying in the electromagnetic spectrum between IR and microwaves [51], has been shown to be an important tool.

Optical Pump Terahertz Probe OPTP is a well-established spectroscopy technique [32, 52, 53, 54] to monitor bulk photo-excited carrier dynamics. An ultrashort optical pulse is exploited to generate free electron-hole pairs, to alter the transmission (or the reflection) coefficient experienced by a propagating THz pulse. Whereas a THz pulse is exploited to probe the excited semiconductor. The photo-carriers effectively screen the THz field, the measurement of the THz field hence provides a measurement of the photo-induced carrier density. By changing the relative delay between the exciting pulse and the measured THz probe, the dynamical response of the photo-carriers can be reconstructed. Such a technique is very popular to map the photo-carrier dynamics in bulk semiconductors, providing relevant information about their mobility and recombination time. OPTP can be used to reveal a vast array of information, such as the ultrafast carrier trapping in semiconductors [55] and the electronic properties of nanowires [56].

The OPTP technique can in principle be extended to measure surface photo-carrier dynamics, with an embodiment operating in reflection: a change in reflectivity of the sample can be related to the density of photo-generated electron-hole pairs, as is generally done in transmission. The optical penetration depth, when illuminating with photon energies largely exceeding the semiconductor bandgap, can be within the order of a few hundred atomic layers or lower [57]. This short depth results in the excitation of carriers in proximity of the surface. However, OPTP is in overall an approach weakly sensitive to surface dynamics. The most important limitation is that, in all practical scenarios, the THz penetration depth is usually very large, on the order of some tens of microns. This situation implies that the actual overlap between the THz decaying field and the photo-excited layer is always quite weak and very weakly dependent on the carrier dynamics in the surface field region. Most importantly, OPTP is not directly sensitive to the surface potential.

Better approaches have been proposed in literature to analyse photo-excited surface carriers. Dynamic Terahertz Emission Microscope (DTEM) is an extension of the Laser Terahertz Emission Microscope (LTEM) [58, 59]. In these techniques, a pump laser is used to excite photo-carriers. The surface current generated by such photo-carriers is

the source of a THz field, which is directly generated in the photo-excited region of the sample, in striking contrast with the OPTP. The DTEM has been applied to phenomenologically describe the THz generated by surge currents in a polycrystalline silicon solar cell [60]. Moreover, LTEM based approaches allow information on the surface potential to be extracted. Very recently, it has been demonstrated that electrically induced changes in the surface potential of materials such as Gallium Nitride, where the generation mechanism is dominated by surge current effects, directly affects the THz generation. Here LTEM has been used to map changes in the THz spectrum induced by the surface potential [58]. Furthermore, LTEM has since been used to probe the surface potential of electrically biased silicon [61]. Mag-Usara et al. proposed the "double optical pump" THz time-domain emission spectroscopy, which maps the carrier lifetimes by observing variation in the surge-current generated THz electric field when varying the delay between a THz generating pump and a second optical screening pump [62].

A potential complexity of LTEM based approaches is that the relationship between the surface potential and the THz field is not direct: the surface field accelerates the surface photo-carriers, while the emitted THz is connected to their motion-dynamics. Most importantly, in low bandgap semiconductors, THz generation mechanisms related to carrier dynamics (surge current generation and photo-Dember emission) are known to saturate quickly as the excitation increases. A recent study [63] modelling photo-Dember carrier dynamics has attributed its saturation to the Coulomb attraction. For excitation fluences of about tens of $\frac{\mu J}{cm^2}$, the THz emission is ruled by SOR. In such regimes, the THz generation is directly related to a symmetry-breaking, static surface field which seeds optical rectification [42]. It is well established that the THz surface optical generation arises from a third order nonlinear effect involving the optical, THz and static surface field itself. The resulting THz field is then directly proportional to the surface field, with an important fallout in surface field monitoring that I will exploit in this chapter. Very interestingly, in most semiconductor surfaces, such surface fields arise directly from the pinning of the Fermi Level induced by the surface states [64]. Thanks to this mechanism, the optical nonlinearity has been proposed for probing surface states in topological insulators [65].

In this chapter, I investigate the use of optical rectification to probe the surface static potential dynamics of a semiconductor by inducing a population of photo-carriers in the surface field region. An ultrashort optical pulse interacts with the surface and, thanks to the presence of the electrostatic surface field, THz radiation is emitted via a third-order

nonlinearity, while a second optical 'screening pump' is used to generate surface photo-carriers. Differently from OPTP, where the photo-carriers screen a THz field, here the photo-carriers screen the static field directly and hence inhibits the generated THz. I will assume a screening pump with typical penetration depth on the scale of the surface field region thickness. This translates to wavelengths of 800 nm or shorter in this case of study (InAs). I named this technique Optical Pump Rectification Emission OPRE . It is worth noting that the screening of the propagating fields has a negligible role in the OPRE. Similar to LTEM, my approach has the benefit of directly generating the THz field on the surface of the semiconductor, with the advantage of the THz emission being directly proportional to the surface potential. Moreover, OPRE can also be efficiently applied to low-bandgap semiconductors, where the nonlinear generation is the dominating mechanism. As such, I could measure a clear linear relation between the photo-excited charges and the screening optical energy. This approach may then open up the possibility of using THz spectroscopy for quantitative analysis of the surface potential distribution in semiconductors and, eventually, of the surface states. Moreover, my results demonstrate that it provides an efficient alternative to OPTP and LTEM for the detection of the photo-induced surface carrier dynamics.

2.2 Optical Pump Rectification Emission

Before entering into the experimental details, it is useful to describe the general principle of the OPRE, together with a brief summary of the OPTP technique, which we used in a reflection configuration as a benchmark for probing photo-induced surface carrier dynamics. Fig. 2.1 sketches the interaction geometry in the two approaches, OPTP and OPRE in (a) and (b) respectively. In the OPTP technique Fig. 2.1 (a) a THz beam is used in reflection geometry to probe the surface carriers generated by a powerful screening pump. The pump has photon energies far exceeding the semiconductor bandgap and induces electron-hole free carrier pairs. The optical penetration depth depends on the strong single photon absorption process and, for a wavelength of 800 nm as used in this experiment is on the order of 140 nm [57]. Note that, in general, such penetration depths are not affected by the generated free-carriers until very high injections. The absorption process of the THz wave, conversely, is ruled solely by the contribution of free-carriers. Hence, the photo-induced charges screen the reflected THz wave. The absorption by free-carriers is weaker than the single photon absorption process therefore the THz penetration depth (on the order of 50 μm in undoped InAs[66]) is much larger than the

penetration of the optical screening pump. I experimentally observe that this results in a small change in the reflectivity of the THz probe. In general, other important limitations arise from the fact that semiconductors usually exhibit a very high refractive index at THz frequencies [67], hence the signal under investigation is normally superimposed with a large contribution originating from the Fresnel reflection. This aspect translates in the need of specific reflection geometries to suppress the strong linear reflection (e.g. the usage of a p-polarised field at the Brewster angle). Moreover, the optical pump can in principle produce an additional change in the THz reflection coefficient through other nonlinear mechanisms, e.g. Kerr-cross phase modulation[68] unrelated to the surface free carrier concentration.

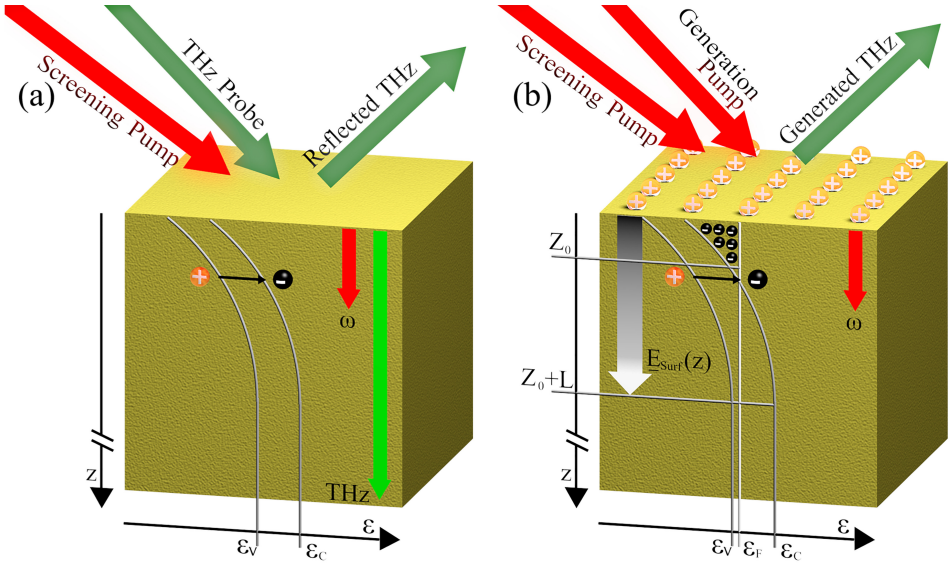

Figure 2.1: A schematic of the excitation geometry of the InAs surface, depicting the relevant physical interactions, for OPTP (a) and OPRE (b) Band diagrams along the depth direction z, with the valence and conducting energies ε_v and ε_c are indicated in both cases. (a) A screening pump induces free electron-hole pairs, such free-carriers are generated mostly within the skin depth of the pump, indicated with the red arrow. The concentration of free-carriers changes the reflectivity of a THz probe. The skin depth of the THz is indicated in green. (b) The surface field E_Z^{surf} is indicated by the graduated arrow, resulting from the balancing of the surface charges (plus signs on the top), and localised free-electrons in the surface accumulation region ($0 < z < Z_0$), and the spatial charge in the depleted ($Z_0 < z < Z_0 + L$) region. Free-electrons in the conduction band are indicated by black dots with minus signs, while ε_F indicates the Fermi level. The THz is generated by the interaction of the generation pump with the surface field, while the screening pump also generates free-carriers in this case, effectively screening the surface field E_Z^{surf} .

In the OPRE technique, the THz wave is generated directly in the sample surface field region. It is important to stress that the underlying principle of SOR relies on a symmetry-breaking static (DC) surface depletion field $\boldsymbol{E} = E_Z^{surf}\hat{\boldsymbol{Z}}$ [69]. The DC surface field is directed along the normal of the surface $\hat{z}$, as depicted in Fig. 2.1 (b); together with the optical generating field ($\boldsymbol{E}_G(\omega)$ in the frequency domain) it contributes to the nonlinear surface polarisation $\boldsymbol{P}_{THz}$ that acts as a source for the emission of a quasi-static THz field with frequency $\omega_{THz} \ll \omega$, where

$$\boldsymbol{P}_{THz} = \chi^{(3)}(\omega_{THz} : -\omega; \omega, 0) : \boldsymbol{E}_G(-\omega) : \boldsymbol{E}_G(\omega) : E_Z^{surf}(0)\hat{\boldsymbol{z}}, \tag{2.1}$$

where $\chi^{(3)}$ represents the third order nonlinear susceptibility tensor. The surface then behaves as an effective second-order material [43]. The elements of the resulting nonlinear susceptibility tensor $\chi^{(2)}$ are:

$$\chi^{(2)}_{ijk}(\omega_{THz} : -\omega; \omega) = E_z^{surf}(0)\chi^{(3)}_{ijkz}(\omega_{THz} : -\omega; \omega, 0). \tag{2.2}$$

The effective nonlinear coefficient is thus directly proportional to the DC surface field of the material. It is important to stress that this quadratic contribution is not related to the quadratic nonlinearity of the medium. The THz wave is then generated by an equivalent second order optical rectification of the ultrashort pulse[44]. From Eq. 2.1 , we shall expect a trend of the THz peak field of the form $E_{THz} \propto W_G E_z^{surf}$, where W_G is the energy of the THz generating pulse, i.e. the generation efficiency is:

$$\eta = \frac{E_{THz}}{W_G} \propto E_z^{surf}. \tag{2.3}$$

There are two important considerations that need to be addressed. The first is that, following Eq. 2.1, the THz source is entirely confined within the penetration depth of the optical field (140 nm at λ=800 nm). With the generating volume decreasing as the wavelength decreases and can be as low as ≈16 nm at $\lambda = 400$ nm [57]. The second, following Eq. 2.3, is that the efficiency η directly reveals the DC surface field E_z^{surf}. Before describing the role of the screening pump, it is important to clarify the nature of the DC surface field, which is directly related to the electric surface states of the semiconductor. To formalise the problem and, specifically, the band bending, we consider the general case of a p-type semiconductor (i.e. with Fermi-level approaching the valence band) and a band bending enriching of a negative charge region in proximity of the surface. It is important to note, however, that in many materials (e.g. InAs, which will be used in the experiments) a significant band bending also occurs in the undoped case, due to the significant charge of the surface states. The electron/hole surface states of a semiconductor represent a perturbation to the charge balance. The total charge Q_{surf}, hosted by such surface states, needs to balance (and hence neutralise) the charge in the semiconductor. Such a charge is mostly confined in the band-bending region close to the material surface [70], comprising of the negative accumulation and Schottky depletion regions, represented in Fig. 2.1 (b) for $0 < z < Z_0$ and $Z_0 < z < Z_0 + L$ respectively. The Schottky depletion

region L is characterised by a constant density of space charge, resulting in a total charge Q_{surf}:

$$Q_{Sc} = -eN_A L, \tag{2.4}$$

where N_A represents the density of ionised acceptors. Close to the surface, the bending of the bands increases and the Fermi level approaches the conduction band minimum. Here the semiconductor has a narrow accumulation region rich of free-electrons with 2-dimensional concentration N_S [71, 72], the total charge is:

$$Q_{Z_0} = -e(N_S + N_A Z_0). \tag{2.5}$$

The total charge balancing the surface charge Q_{surf} in the band-bending region is then $Q_{Z_0} + Q_{Sc}$. Fig. 2.1 (b) we reported the energy level diagram in the surface accumulation and Schottky depletion regions. The surface charge Q_{surf} is represented on the top surface of the material. The free-electron charges are sketched behind the surface. They represent a large fraction of the total charge when the Fermi level is pinned well above the conduction band minimum. The biasing potential induced by the charge of the surface states gives rise to the DC surface electric field that seeds the four wave-mixing process in Fig. 2.1 The DC field immediately at the surface[73] is then

$$E_z^{surf}(z=0) = -\frac{Q_{z_0} + Q_{Sc}}{\epsilon} = \frac{e}{\epsilon}[N_A(Z_0 + L) + N_s]. \tag{2.6}$$

The DC surface field monotonically decreases with z in the Schottky region until it completely neutralises. In SOR, however, we can assume that a significant fraction of the generated THz can be attributed to the region between the surface and the electron accumulation layer (where the surface field is maximum and approximately constant) and is proportional to the electric field given by Eq. 2.6. This is also true in low-doped or intrinsic materials, as in those cases the DC surface field is only strong for $z < Z_0$.
We can now take into account the role of the screening optical pump. When photoexcitation is included, hot carriers are induced in proximity of the surface, similarly to the case of OPTP. We will assume that, immediately after excitation, most of the photo-excited electrons are localised in the potential well and drift (because of the high mobility) towards the surface, screening the surface charges and hence the DC surface field E_z^{surf} .

By assuming that the saturation dynamics is effective within the typical THz timescales (my screening time resolution is within the order of 3 ps) the density of photo-electrons close to the surface layer can be approximated as a surface density n_{Ph}, which directly modifies Eq. 2.6:

$$E_z^{surf}(z=0) = \frac{e}{\epsilon}[N_A(Z_0 + L(+N_S - n_{Ph}))]. \tag{2.7}$$

The carriers inhibit the DC surface field E_z^{surf} , effectively reducing the THz generation efficiency in proximity of the accumulation region (where the nonlinear conversion is stronger because of the high field). Relevantly, at low injections, the density of screening photo-electrons is proportional to the impinging optical energy. Neglecting the very small impinging angle difference between screening pump and THz generating pump, we expect a dependence of the type:

$$n_{Ph} \propto (W_G + W_S), \tag{2.8}$$

where W_s is the energy of the screening pulse. For low energy, the modulation of the surface potential is the sole source of change, as the THz emission is not significantly related to the screening of any of the propagating fields, in stark contrast to OPTP where the photo-carriers screen the THz field directly by increasing its reflection. Before closing this section, it is worth briefly discussing the expected dynamics of the photo-carriers. The total electromotive field for electrons is[74]

$$E(z) = E_z^{surf}(z) + P_T\frac{dT}{dz} + \frac{eD_N}{\sigma}\frac{dN_{Ph}}{dz}, \tag{2.9}$$

where P_T represents the thermoelectric power, T the temperature, D_N the electron diffusion coefficient, N_{Ph} the volume density of photo-generated carriers and σ the conductivity. At high screening injections, we expect E_z^{surf} to be comparable or smaller than the thermoelectric and diffusion terms in Eq. 2.9, hence other dynamics may become relevant. It is outside the scope of this chapter to discuss high-injection dynamics, but we can argue that, as the excitation increases, the depletion layer contracts because the band-bending is reduced by the accumulation of photo-electrons close to the surface. This means that we expect a saturation of the screening effect because most of the carriers will then be generated near or outside the surface field region. The motion of those carriers is then

dominated by diffusion and thermal dynamics, only marginally contributing to further screening of $E_z^{surf}(z)$.

Finally, the electromotive force affects both holes and electrons. In materials such as InAs, however, the mobilities of the two carriers are rather different. This creates a mostly unipolar electron flow [74, 75]. Although a unipolar flow can induce photo-Dember THz generation, such generation is quite saturated at the high excitations considered here and has negligible s-polarisation contribution [76].

2.3 Experimental Setup

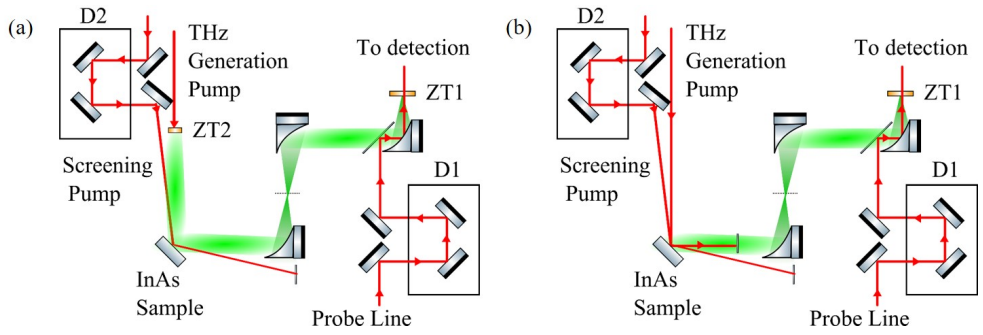

Figure 2.2: Experimental setup for OPTP (a) and OPRE (b) diagnostics. The red and green beam paths denote the 800 nm optical and THz beam paths respectively. For both setups, the THz field is measured with a standard electro-optic detection, which retrieves the change of polarisation of an optical probe of energy ($\approx$1 μJ) inside a ZnTe detection crystal (ZT1) due to the THz field. A delay line D1 controls the delay t_d between the THz and the optical probe and allows for the reconstruction of the THz waveform. (a) The THz is generated by a ZnTe crystal (ZT2) converting a generation pump with a pulse energy of 1 mJ. (b) The THz is directly generated on the sample under investigation (InAs sample) converting a generating pump with energy 0.1 mJ. In both configurations, the relative angle between the screening pump beam and the THz probe beam (a) or optical generating pump (b) is 11.9°. The p-polarised screening pump energy was 1 mJ and 0.1 mJ for (a) and (b) respectively. The delay between the screening optical pulse and the generating optical pulse τ_s is controlled with the delay line D2 in both cases.

Fig. 2.2 (a) and (b) show the experimental setup for OPTP (used as reference) and OPRE respectively. The excitation pulses are supplied by a 5 mJ-class Ti:Sa regenerative amplifier (Coherent Libra-He) generating 100 fs pulses centred at $\lambda = 800$nm, with a 1 kHz repetition rate. The beam diameter (intensity at $\frac{1}{e^2}$) d =9 mm was determined via knife-

edge technique. The setup comprises of three separate beam lines, the THz excitation pump (≈1.5 mJ), the screening pump (≈2.5mJ) and the optical sampling probe (≈1 μJ) for the detection. A THz electro-optic detection is implemented by co-propagating the THz field and the optical sampling probe in a standard 1mm thick $<110>$ZnTe crystal[77]. For the OPTP, the detection crystal and the probe polarisation are set to detect the p-polarised THz field. For the OPRE a s-detection is preferred as it is in principle unaffected by any carrier-mediated generation phenomena. As in standard TDS schemes, the time-domain traces are reconstructed by changing the delay t_d between the THz and the optical probe. The TDS signal is measured with a balanced photo-detection unit feeding a lock-in amplifier. The main emitter consists of a standard 1mm thick $<110>$ ZnTe crystal for the OPTP case that generates the THz probe. The sample under investigation is an undoped 0.5 mm-thick $<100>$ InAs crystal, which is also used for generating the THz in the OPRE case. The typical semiconductor bandgap is on the order of 0.35 eV, much lower than the photon energy of 1.55 eV used for both the generating and screening pumps, translating to a skin depth for normal illumination on the order of 140nm [57]. This value needs to be considered as an upper boundary, and as the skin depth decreases with the impinging angle[78] of the optical beam on the surface. The angle between the screening pump and THz probe and between the screening pump and generating pump is fixed at 11.9° for both OPTP and OPRE respectively. This results in a temporal smearing and thus a resolution of the pump delay within the order of 3ps.

A system of delay lines allows for the independent control of the group delay in the screening pump and optical probe lines. For the OPRE case in Fig. 2.2 (b) the generation mechanism of the s-polarised THz emission in InAs was confirmed to be optical rectification by rotating the polarisation of the generation pump: we observed a two-fold symmetry typical of optical rectification emission from surfaces[76]. This also allowed us to exclude any relevant contribution of the photo-Dember effect, which is unaffected by a change of polarisation[76] and was not detectable for angles of minimum generation by optical rectification. In contrast to[63], where the sample was rotated to suppress the SOR, we oriented the surface and the generating pump polarisation to maximise the nonlinear conversion efficiency.

2.4 Results and Discussion

As a benchmark of this technique, we measured the photo-carrier dynamics with a reflective OPTP trace for an undoped InAs substrate. In this experiment, the THz was

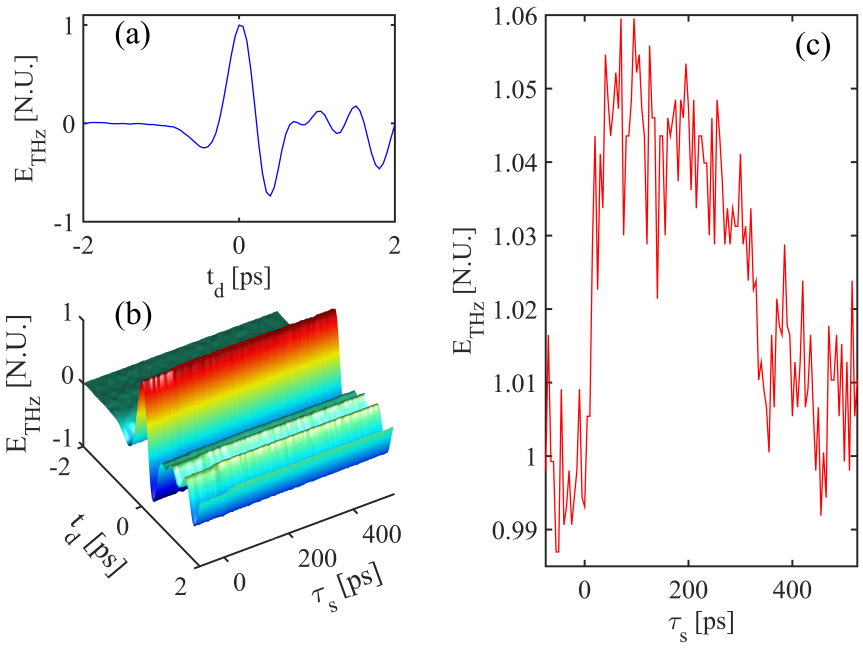

Figure 2.3: Reflective OPTP trace for an undoped $< 100 >$ InAs substrate. (a) A typical THz waveform reflected by the InAs sample, for a generating pump energy of 1mJ, as a function of the TDS delay t_d. (b) Measured THz field as reflected from the InAs substrate as a function of the TDS delay t_d and screening pump delay τ_s, for a THz pump energy and screening pump energy of 1 mJ. The delay $\tau_s = 0$ represents the perfect temporal matching between the screening pump and the peak of the impinging THz wave. (c) Detail of the recovery of the peak THz field ($t_d = 0$) vs the screening pump delay τ_s.

generated by bulk optical rectification of 1 mJ optical pulses in a ZnTe crystal. Fig. 2.3 (a) reports a typical THz wave generated in the system, reconstructed in time against the delay t_d between the THz pulse and the optical probe pulse in the detection scheme Fig. 2.2. The reflectivity of the sample for the THz probe was increased when a screening pump of 1 mJ was overlapped in the sample. This is visible in Fig. 2.3 (b) where we report the evolution of the THz waveform with the delay τ_s between the optical screening pump and the THz. The change of reflectivity is visible in a weak modulation of the THz wave that fades away for large delays. Reflective OPTP indeed allows for the carrier relaxation dynamics to be inferred from the change in reflectivity of the sample. The increase in reflectivity is related to the increased conductivity due to the photo-carriers generated by the screening pump. As stated above, the interpretation of the time-resolved or frequency resolved traces is quite complex because in many practical scenarios the penetration depth of THz and optical fields are rather different. Hence, the distribution of photo-carriers

along z is very inhomogeneous on the scale of the THz penetration depth. This makes the modelling of the reflection using the standard Leontovich approach difficult[79].

Most importantly, the key drawback of this technique is that the signal variation (and therefore the change in the THz signal) is very small when compared to the total signal received, as visible in Fig. 2.3 (b). A better visualisation of the reflectivity change is obtained by plotting the THz peak field (measured for a fixed delay $t_d = 0$), as reported in Fig. 2.3 (c). This is the measurement with the best contrast and the relative change in THz field is approximately 5×10^{-2}. The RMS noise of this measurement was 8.2×10^{-3}, resulting in a signal-to-noise ratio (SNR) lower than 8.6 dB. Widening my comparison to the reflective electro-optic sampling approach[29] (that estimates the carrier density from the optical reflectivity) it is also experimentally observed that a very faint relative change of the power of the reflected THz generating optical pump, which is on the order of 4×10^{-5}. Summarising, the OPTP approach leads to signal contrast on the order of 5×10^{-2}, with a low SNR of 8.6 dB, in measuring the photo-carriers effect on the reflectivity. In addition, the observed carrier dynamics show a decay on the order of ns, as visible in Fig. 2.3 (c). Such a decay time is compatible with the carriers' recombination time and appears mostly unrelated to the dynamics of the surface potential, which are expected to occur at lower time scales.

In the OPRE setup, the generation is obtained directly on the InAs sample with a 0.1 mJ optical pump. A typical THz trace generated with this setup is reported in Fig. 2.4 (a), and represented by the blue plot. The THz trace for a screening pump pulse of energy 0.1 mJ at maximum overlap ($\tau_s = 0$) with the generating pump is reported in black. The contrast is clearly higher than in OPTP for a much lower THz pump pulse energy (0.1 mJ) and screening pump pulse energy (0.1 mJ): at $\tau_s = 0$ a relative change of around 87% is observed, with no appreciable distortion of the waveform. Under measuring conditions, the laser source stability introduces noise with RMS relative to the peak field estimated to be lower than 3.5%. This gives rise to an SNR at maximum contrast of 30 dB. More importantly, we can observe here rather different temporal dynamics. This is visible in Fig. 2.4 (b), where we observe the change in the THz field with the delay τ_s for the whole temporal scale, and in Fig. 2.4 (c), where the recovery of the THz peak measured at $t_d = 0$. Differently from the OPTP trace in Fig. 2.3 (c), that shows a slow recovery in the ns range, the OPRE reveals a fast recovery immediately after the screening time $\tau_s = 0$ we can argue that OPRE perceives the modulation of the DC surface potential (which is established in a thin region), where the diffusion of photo-electrons (described in Eq. 2.9) is a relevant

process in InAs on the ps scale [75], making it the source of these fast dynamics. This migration reduces the effective concentration of charges screening the DC surface electric field. A second, slower, dynamic is instead related to the recombination time, similarly to what is observed with the OPTP diagnostics. In sharp difference with the OPTP, however, the OPRE technique explicitly reveals the dynamics of carriers interacting with the DC surface field region.

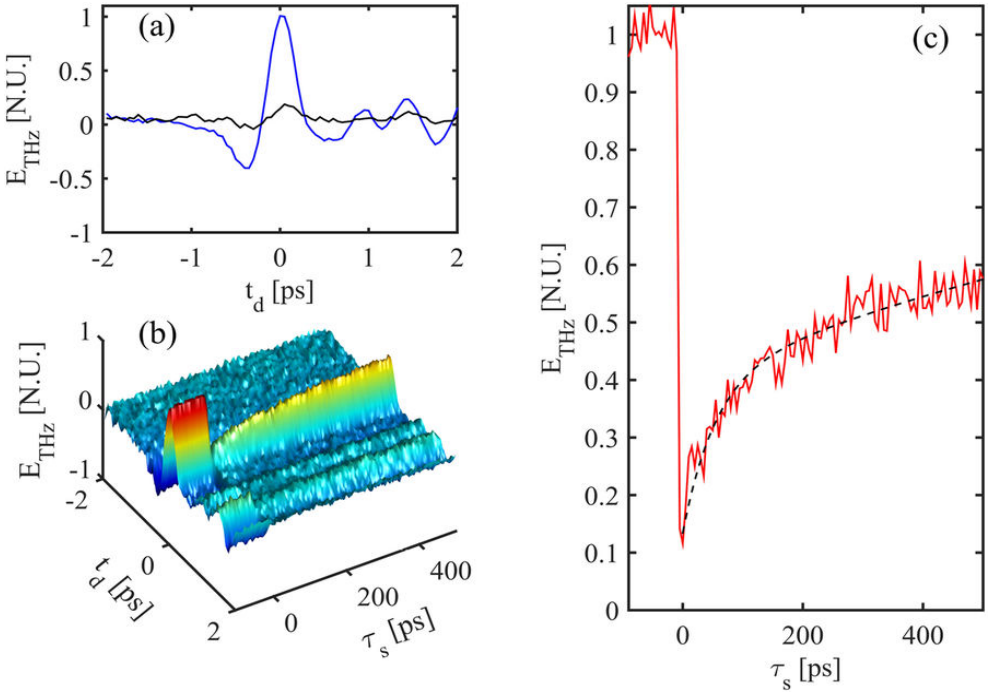

Figure 2.4: OPRE trace for an undoped $< 100 >$ InAs substrate in the configuration for detecting s polarised THz. (a) A typical THz waveform generated by the InAs sample, by a pump energy of 0.1 mJ, as a function of the TDS delay t_d. The blue plot is the TDS trace for no screening pump, the black plot is for a perfectly overlapped ($\tau_s = 0$) screening pump of 0.1 mJ (b) Measured THz field as generated from the InAs substrate as a function of the TDS delay t_d and screening pump delay τ_s, for a THz pump energy and screening pump energy of 0.1 mJ. The delay $\tau_s = 0$ represents the perfect temporal matching between the screening pump and the peak of the impinging THz wave. (c) Detail of the recovery of the peak THz field ($t_d = 0$) vs the screening pump delay τ_s. The dashed-plot represents the best fit with a double exponential trend. Under measuring conditions, the laser source stability introduces noise with RMS relative to the peak field estimated to be lower than 3.5%.

For the data in Fig. 2.4, it was found that the decaying curve can be fit by a combination of two exponential decays (reported in dashed black) with different time constants: a

fast recovery time constant on the order of 50 ps, that can be associated to the diffusion of the photo-carriers away from the surface-field region, and the much slower recombination time, above 1 ns (the fit of the fast recovery is quite sensitive to the estimation of the screening time). This description potentially provides another physical mechanism consistent with the need in literature to fit surface charge decay rates with two different time constants in experiments based on THz emission spectroscopy [80], e.g. when emitted by surge currents [62]. In fact, such an experiment could face a similar decay trend as in my OPRE case. To further analyse the capability of the OPRE experiments, we studied the effect of the screening pump energy on the THz generation efficiency η defined by Eq. 2.3. Specifically, we considered the reduced efficiency resulting from the screening pump by measuring the THz peak field, that occurs at $\tau_s = 0$ and $t_d = 0$ (black plot in Fig. 2.4 (a)). In Fig. 2.5 we report such a minimum for the efficiency at various screening pulse energies obtained from OPRE scans.

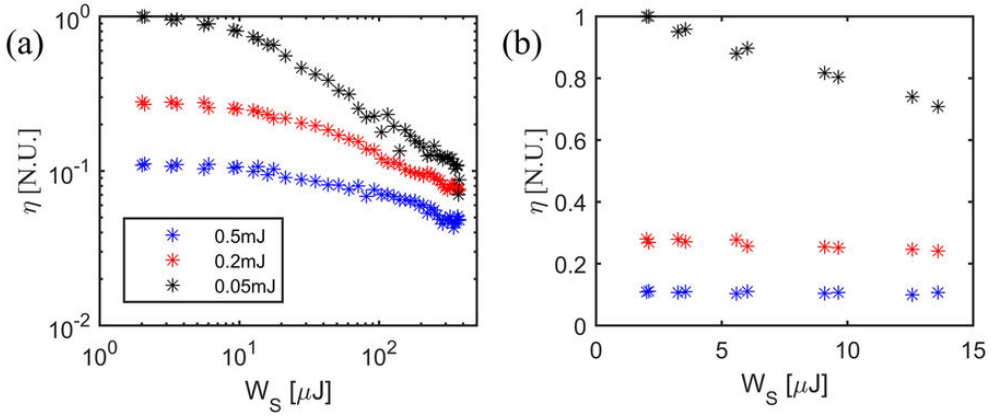

Figure 2.5: (a) Generation efficiency $\eta = \frac{E_{THz}}{W_G}$ vs. screening pump energy W_s for three different THz generation pump energies W_G in the configuration for detecting p polarised THz. (b) Detail of the generation efficiency at low screening energies, showing the linear trend with the screening energy W_s.

In line with Eq.2.8 and Eq. 2.9, as discussed previously, such a measurement is mapping the screening of the DC surface field. As visible in Fig. 2.5 (a), the THz field initially decreases linearly with the screening pump at low energy injection (better highlighted in Fig. 2.5 (b) for values below 2 μJ, whereas the dependence becomes more complex at high screening energies. This result is consistent with the prediction of the linear dependence between DC surface field and screening pulse energy (i.e. a quadratic dependence between the THz pulse energy and the screening energy). Such a linear dependence also occurs with the energy of the generating pump W_G. From Fig. 2.5 (b), we can appreciate that,

in the case where $W_G = 0.5$ mJ, the efficiency η for $W_s \approx 0$ is approximately 35% the efficiency for $W_G = 0.2$ mJ and 10% the efficiency for $W_G = 0.05$ mJ. This corroborates the hypothesis that the surface potential is screened by the surface carriers.

In this investigation, in order to isolate the contribution of the OR from any parasitic contribution of carrier-mediated generation mechanisms, the detection crystal was rotated to detect the s-polarised (perpendicular to the impinging plane). It can be argued that for $< 100 >$ InAs under the given illumination condition the potential out-of-plane (s) carrier dynamics induced by structural anisotropies for both the field-driven surge-current and photo-Dember mechanisms should be negligible. Attached here are Fig. 2.6 and Fig. 2.7 which are equivalent to Fig. 2.4 and Fig. 2.7 respectively. But with the detection crystal orientated to detect the p-polarisation. The trends between detecting p-polarisation and detecting s-polarisation are very similar, potentially highlighting how dominant SOR is when compared to the field driven surge-current and photo-Dember mechanisms at high excitation fluence.

2.5 Conclusions

To conclude, a new technique for mapping the DC surface potential in semiconductors has been proposed. The THz field is generated uniquely in the DC surface field-region by optical rectification and the efficiency of the process is directly dependent on the DC surface field. The physical understanding has been tested by analysing the inhibiting effect in the THz generation of photo-induced free-carriers by an optical screening pump. The THz generation is strongly inhibited by the presence of the photo-carriers and that the reduction of the efficiency generation is linear with the optical screening pump energy at low injections. In addition, when compared to the standard OPTP, the enhanced sensitivity to the surface carriers is due to the inherent physical difference between the two methods, the OPTP approach being based on a screening effect of the charges on the THz probe, that increases its reflectivity, while my OPRE is based on a modulation of the generation directly related to the screening of the DC surface field. This was also confirmed by verifying the linearity of the reduction in generation efficiency with the optical energy. Finally, as opposed to OPTP, which does not specifically relate to carrier dynamics at the surface, nor is it directly related to the surface potential, the OPRE directly probes the surface potential in semiconductors. This could lead to novel methods to qualify semiconductor surfaces with potential impact in electronics, photovoltaics and optical sensors.

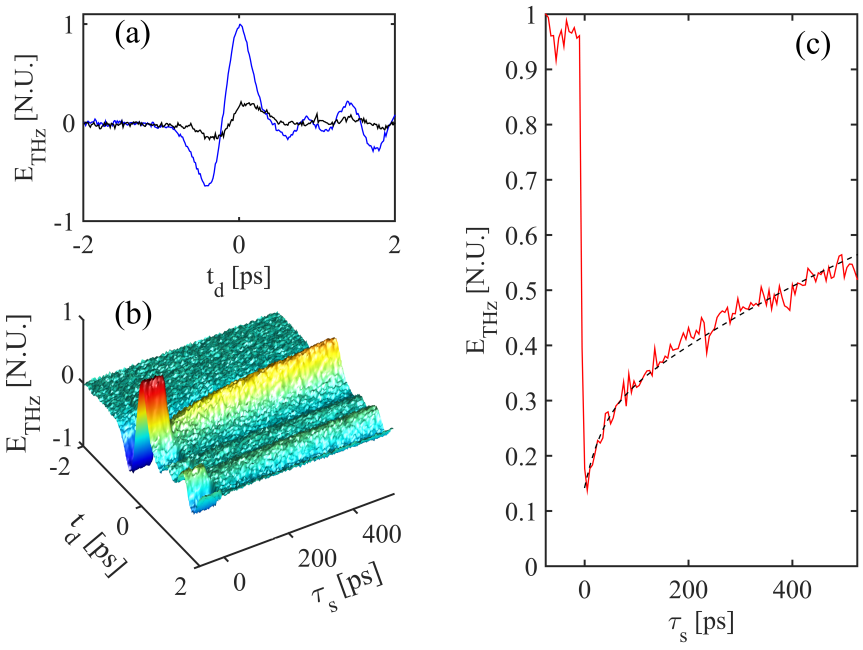

Figure 2.6: OPRE trace for an undoped < 100 > InAs substrate in the configuration for detecting p polarised THz . (a) A typical THz waveform generated by the InAs sample, by a pump energy of 0.1 mJ, as a function of the TDS delay t_d. The blue plot is the TDS trace for no screening pump, the black plot is for a perfectly overlapped (τ_s=0) screening pump of 0.1 mJ (b) Measured THz field as generated from the InAs substrate as a function of the TDS delay t_d and screening pump delay τ_s, for a THz pump energy and screening pump energy of 0.1 mJ. The delay τ_s=0 represents the perfect temporal matching between the screening pump and the peak of the impinging THz wave. (c) Detail of the recovery of the peak THz field (t_d=0) vs the screening pump delay τ_s. The dashed-plot represents the best fit with a double-exponential trend. Under measuring conditions, the laser source stability introduces an RMS noise relative to the peak field estimated to be 1.5%.

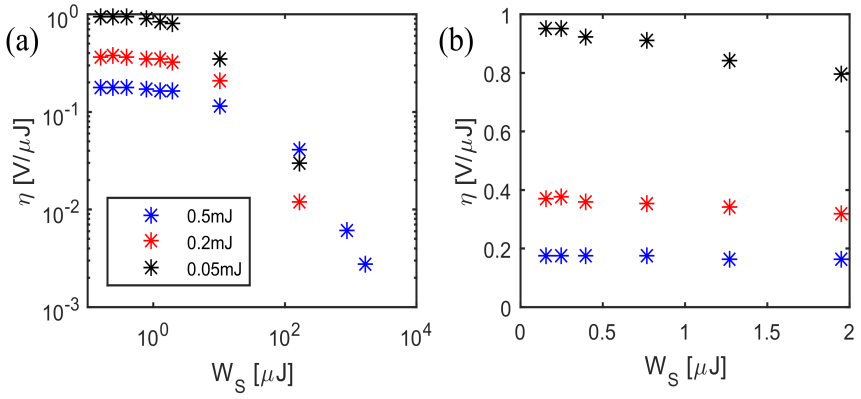

Figure 2.7: (a) Generation efficiency $\eta = \frac{E_{THz}}{W_G}$ vs. screening pump energy W_s for three different THz generation pump energies W_G in the configuration for detecting s polarised THz. (b). Detail of the generation efficiency at low screening energies, showing the linear trend with the screening energy W_s .

Chapter 3

Saturation of surface Optical Rectification

The contents of this chapter have been published in [81]. The interest in surface THz emitters lies in their extremely thin active region, typically hundreds of atomic layers, and the agile surface scalability. The ultimate limit in the achievable emission is determined by the saturation of the several different mechanisms concurring to the THz frequency conversion. Although there is a very prolific debate about the contribution of each process, SOR has been highlighted as the dominant process at high excitation, but the effective limits in the conversion are largely unknown. The current state of the art suggests that in field-induced optical rectification a maximum limit of the emission may exist and it is ruled by the photocarrier induced neutralisation of the medium's surface field. This would represent the most important impediment to the application of SOR in high-energy THz emitters. This chapter unveils novel physical insights in the THz conversion at high excitation energies mediated by the ultrafast SOR process. The main finding is that the expected saturation of the THz emission vs pump energy does not actually occur. At high energy, the surface field region contracts towards the surface. It is argued that this mechanism weakens the main saturation process, re-establishing a clearly observable quadratic dependence between the emitted THz energy and the excitation. This enables access to intense generation at high fluences.

3.1 Introduction

A significant fraction of the pioneering works on THz surface emission focuses on narrow band-gap III-V semiconductors, such as InAs and InSb, which exhibit surface THz emission

when excited with ultrashort optical pulses. In most scenarios, the generation is driven by the kinetic carrier dynamics [21, 25, 20] and surface field-induced Optical Rectification (OR) [42, 82, 83], upon excitation with photon energies well above the energy bandgap [84]. The interest is certainly driven by the surprisingly high conversion efficiencies. For materials possessing a direct band structure, the optical absorption depth for photons with energy exceeding the bandgap is typically very low (e.g. within the scale of $100nm - 200$ nm at $\lambda = 800$ nm in InAs [57]). A significant and macroscopic THz emission is then obtained in a very thin interaction region, with very high energy conversion per unit thickness [85].

At low impinging fluences (below $100\frac{textrmnJ}{textrmcm^2}$), InAs is perhaps one of the most important benchmarks for surface THz emission driven by the photo-Dember effect [86, 87]. However, it has been argued that THz generation by carrier migration is quite saturated at high excitation energies and that the generation is dominated by surface OR [20]. This interpretation reconciles the observed dependence of the emission from the polarisation and crystal orientation in InAs and seeded thorough works about the microscopic mechanisms responsible for the nonlinearity [88, 89, 90].

A saturation fluence for surface OR has been identified within the order of tens of $\frac{\mu J}{textrmcm^2}$ by Reid et al [69] The specific mechanism has not been investigated. Yet, its understanding is clearly fundamental in boosting the THz conversion efficiency at semiconductor surfaces. The basic model of the SOR process suggests that the main saturation mechanism in OR is driven by the drift of photoinduced carriers that screen the static surface field of the semiconductor responsible for the surface nonlinearity [42].

In this chapter, we explore the emission limits, with a novel methodology. The experimental approach involves the THz generation with an ultrafast generating pump and the simultaneous injection of photo-carriers in the surface field region (within 100 nm -200 nm of the surface) with a second optical screening pump. The underlying idea is to connect the change of the emitted field to the modulation of the surface field as it is neutralised by the photo-carrier drift. The photo-carriers frustrate the surface potential, changing its contribution to the third-order nonlinear ruling mechanism of surface OR, in a process that I can define as OPRE [45] (by analogy with the OPTP). Krotkus et al [91] argued that at moderate exciting peak powers the surface static field could be significantly augmented by the carrier diffusion but that this does not affect the OR frustration mechanism. With specific reference to my experimental campaign, the signature of this specific contribution is not present at high energy excitations (we present the complete characterisation set

later in this chapter). It is worth noting that the THz emission through surface OR is a third-order nonlinear phenomenon and is driven by the cubic relation [42]

$$\boldsymbol{E_{THz}} \propto \chi^{(3)}(\omega_{THz} : -\omega; \omega, 0) : \boldsymbol{E_G}(-\omega) : \boldsymbol{E_G}(\omega) : E^{(0)}_{surf}(0)\hat{\boldsymbol{z}}. \tag{3.1}$$

As such it is not related to the bulk OR which is driven by the second-order medium nonlinear response ($\chi^{(2)}$), which is not relevant in the physics at semiconductor surfaces.

In this investigation, we can argue that because of the very small penetration depth of the optical NIR excitation, the change of the THz generation is also significantly connected to the weakening and contraction of the surface field region upon carrier screening. Hence, at high pumping energies most of the photocarriers are generated outside of the surface field region and therefore they no longer contribute to the saturation. At this point, the system converges again to a quadratic conversion efficiency because the progress of the screening of the surface field is no-longer significant. In different words, a real flattening of the pump vs emission trend should not exist, this observation is consistent with my experimental results.

3.2 The field-matter interaction mechanism

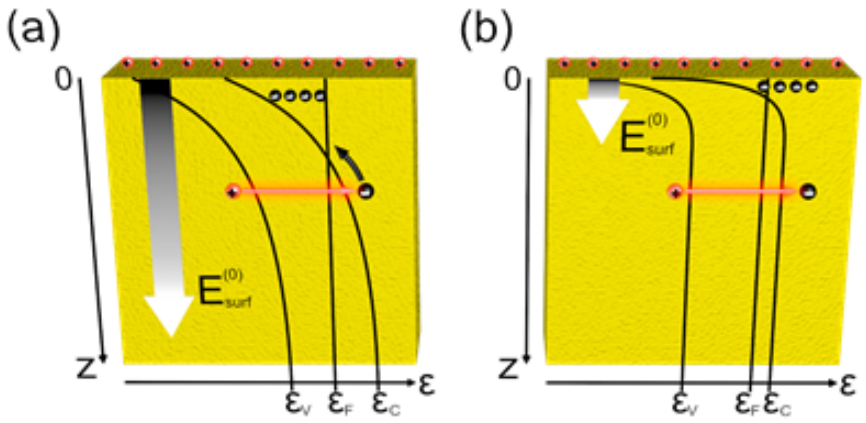

Figure 3.1: A sketch depicting the bending of the boundary of the valence (ε_V) and conduction (ε_C) bands at the InAs surface for (a) Undoped InAs and (b) n-Type InAs, where the positive surface states pin the Fermi level (ε_F) above the conduction band minimum at the surface. $E^{(0)}_{surf}$ is depicted by the graduated arrow where darker shades represent a higher field magnitude. In the latter case, photo-excited electron-hole pairs are mostly generated outside the surface field region, weakening their role in surface field screening.

The field-matter interaction at the semiconductor band bending region is sketched in Fig. 3.1. In InAs, the benchmark model, the surface states result in a positively charged surface density regardless of the doping type [92]. This pins the position of the Fermi-level above the conduction band minimum at the surface such that an electron accumulation layer is formed immediately below the surface. When photoexcited electron-hole pairs are generated, the electrons dominate the surface potential dynamics in light of their much higher mobility.

To infer the contraction, we observe that in InAs the surface field region is known to weaken and contract as the concentration of free electrons increases [93, 94, 75] [27–29]. Interestingly, because of the large difference in mobility, moderately doped p-type InAs exhibits lower conduction and a thicker surface field region than intrinsic and n-doped InAs. At significant n-doping levels, at room temperature, the surface field region thickness (Fig. 3.1 (b)) can be much smaller (tens of nm) than the optical penetration depth.

The experimental campaign revealed that the typical generation vs excitation trend observed at any n-doping concentration can be reproduced by photo-exciting a p-type semiconductor, corroborating the hypothesis that even in this latter case the field region weakens and thins as the concentration of photocarriers increases. Hence, we argue that upon intense optical pumping the fraction of photocarriers neutralising the surface-field decays and that this is a relevant mechanism in re-establishing a quadratic dependence between emission and excitation. For the work in this chapter, unless otherwise specified, the experimental setup and procedure are the same as described in Chapter 2.

$$n_{Ph}(z) \propto W_G. \tag{3.2}$$

The surface accumulation layer is essentially a 2-dimensional distribution of electrons centred up to tens of nanometres below the surface because of the quantisation of motion of the electrons in the z-direction [73]. We can assume that a fraction of the photo-electrons drift to screen the surface field $E^{(0)}_{surf}$ and approximated that as equivalent to a 2-D layer of density n_{Ph}.

$$E_{surf}(z=0) = E^{(0)}_{surf} - n_{Ph}\frac{e}{\epsilon}. \tag{3.3}$$

However, as the field weakens at high excitations, n_{Ph} becomes a progressively smaller fraction of the total population of photoexcited carriers, mitigating any further increment of n_{Ph}, i.e. weakening the main saturation mechanism. This is a potential source of the trend observed in Fig. 3.2, where a linear dependence between THz peak field and pump energy (i.e. a quadratic conversion) is re-established after a 'knee'. Quite interestingly, in the case of highly n-doped materials (blue and red plots), in which the surface field

region is known to be very thin, this high-energy linear dependence between peak field and energy (i.e. a quadratic conversion) almost covers the entire generation pump energy range.

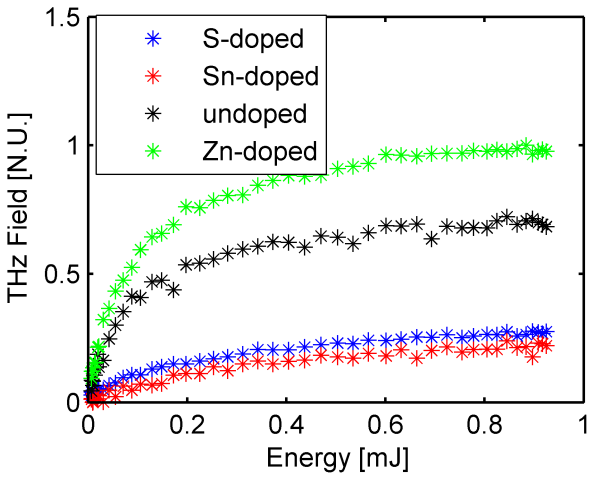

Figure 3.2: The peak THz field has been plotted for various excitation energies, for a number of different freestanding $< 100 >$ InAs substrates, two n-type samples doped with Sn and S donors, one undoped sample and one p-type sample doped with Zn acceptors. The peak THz field has been normalised across all substrates with respect to the maximum field achieved with the Zn-doped InAs.

In Reid et al [69], the saturation curve in the OR process is fitted with a typical saturation equation

$$E_{THz} = \frac{AW_G}{W_G + W_{sat}}, \tag{3.4}$$

where A represents the maximum THz peak field, E_{THz} is the THz field and W_{sat} is the saturation energy. The best fit values for W_{sat} for each of the curves are displayed in Table. 3.1. In light of the sufficient accuracy of my experimental measurement, we can observe in Fig. 3.2. that at high energy E_{THz} does not exhibit the plateau predicted by Eq. 3.3. This results in a very poor statistical significance of the fitted values ($\chi^2 = 9.03$ for undoped InAs). The observed linear trend corroborates the hypothesis that the main saturation mechanism weakens at high energy.

It is worth noting that because of the much higher mobility of electrons, the undoped substrate (that possesses a process-induced n-doping around ($2{\times}10^{16}\mathrm{cm}^{-3}$)) exhibits a weaker surface field and a lower conversion efficiency when compared to the p-doped sample.

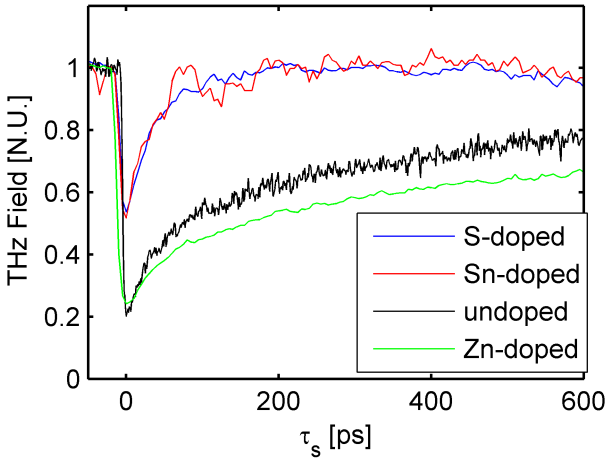

Figure 3.3: OPRE measurements of the peak THz field vs the screening pump delay for the four different freestanding $< 100 >$ InAs substrates of Table. 3.1. Each curve is normalised with respect to the unscreened peak THz field.

In Fig. 3.3, the OPRE measurement in the different samples is presented: it is clear that the free electron concentration has an important impact on these dynamics. Following a similar approach to literature, the normalised recovery trend is fitted as [62]

$$E_{THz} = 1 - k_1 \times e^{-\frac{\tau_s}{\tau_1}} - k_2 \times e^{-\frac{\tau_s}{\tau_2}}, \tag{3.5}$$

where k_1, k_2, τ_1, τ_2 are the fitting parameters and τ_s is the time delay between the screening pump and the THz emission pump. τ_1 represents a fast recovery time. It is potentially consistent with the time scale of the migration of photocarriers away from the surface-field region as its thickness can be a very small fraction of the pump wavelength. Although we should expect the carrier diffusion to be a dominant process in the carrier dynamics (as recognised in a number of studies as the source of the photo-Dember mechanism) we cannot exclude a contribution from quasi-ballistic photo-electron dynamics [95] and from the electron scattering into other conduction band valleys. τ_2 is consistent with the slow recovery time typically associated with the bulk recombination of photoexcited carriers.

Substrate	Doping[cm^{-3}]	W_{sat} [μJ]	$\tau_1[ps]$	$\tau_2[ns]$	R^2[N.U.]	RDC [N.U.]
n-InAs S-doped < 100 >	n = 1×10^{18}	201	40	N/A	0.817	2.83
n-InAs Sn-doped < 100 >	n = $3 - 10 \times 10^{17}$	371	31	N/A	0.846	3.40
n-InAs undoped < 100 >	n < 3×10^{16}	88	54	>1.0	0.947	1.00
p-InAs Zn-doped < 100 >	p = 5.3×10^{18}	86	37	1.0	0.982	0.28

Table 3.1: Shows the known carrier concentration, saturation power and THz recovery times once excited for a number of different substrates. In light of the low accuracy in the doping specified by the supplier, the measured relative dark conductivity (RDC), relative to the undoped sample is also reported.

For the n-doped sample, we can assume k_2=0 as there is no appreciable slow decay in the traces: this appears consistent with the assumption that only the decay of the photocarrier density in a very thin region close to the surface dominates the dynamics. As soon as the concentration of carriers becomes comparable to the inherent free carrier concentration (from doping) the THz emission returns to its original level. Therefore, in n-doped substrates, the bulk carrier recombination time does not appear to be relevant in the OPRE measurements. The best-fitting parameters can be appreciated in Table. 3.1.

We compared the doping of the substrates along with the calculated values for the saturation power (W_{sat}) and surface field recovery times in Table. 3.1. For the sake of comparison, W_{sat} was extracted from the data fitted using Eq. 3.3. It is evident that the apparent saturation of n-type samples occurs at significantly larger powers.

To test the main hypothesis, we reproduced the conversion trend of Fig. 3.2 for the undoped and n-doped media by artificially pumping photocarriers within the surface field regions in the p-type InAs, using the SP with appropriate energy. We fixed the delay of the SP to obtain the maximum screening. The expected effect is an increase in the electron-mediated screening of the surface field. The acquired data are presented in Fig. 3.4.

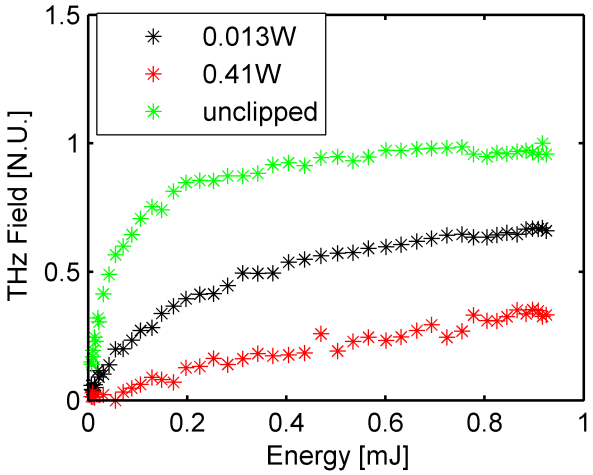

Figure 3.4: The peak THz field has been plotted against W_G, for a Zn-doped $< 100 >$ p-InAs substrate, for various screening energies W_s fixed at τ_s=0. The peak THz field has been normalised across with respect to the maximum peak field generated by Zn-doped InAs.

The average screening pulse energy W_S could be adjusted to reproduce fairly accurately all the observed conversion trends in the undoped and n-doped cases of Fig. 3.2. Hence, we can deduce and argue that the photo-carriers produce the same contraction of the surface field region as it is known to be the case when the material is n-doped.

In addition, it is worth observing that the photo-excited carrier distribution in the pumped example of Fig. 3.4 is certainly very different from the almost homogeneous free-carrier density of the n-type sample. Then, the close matching of the trends of Fig. 3.2 and Fig. 3.4 suggests that all the screening dynamics must occur within depths much smaller than the optical skin depth (so that the carrier profile plays a minor role), which also corroborates the main hypothesis. This also suggests that the carrier induced screening of the THz propagating field plays a minor role (the typical THz skin-depth in the used n-doped materials lies in the range of hundreds of nm to micrometre scales).

In this investigation, in order to isolate the contribution of the OR from any parasitic contribution of carrier-mediated generation mechanisms, we detect the s-polarised THz field (perpendicular to the impinging plane). Fig. 3.5 shows the detected THz waveforms for both s- and p-polarised electric fields emitted by $< 100 >$ Zn doped p-InAs, where the input optical polarisation has been oriented to maximise the emitted THz field.

Although we cannot exclude contamination from carrier mediated generation, for the sake of completeness we recreated analogous cases of Fig. 3.2, Fig. 3.3 and Fig. 3.4 for the p-polarised emission (Fig. 3.6, Fig. 3.7 and Fig. 3.8 respectively) to highlight that

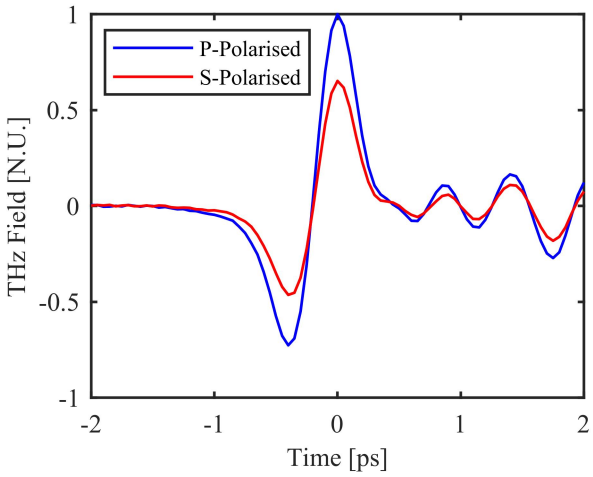

Figure 3.5: Detected THz waveform generated from < 100 > p-InAs. Both TDS measurements have been normalised with respect to the p-polarised peak field.

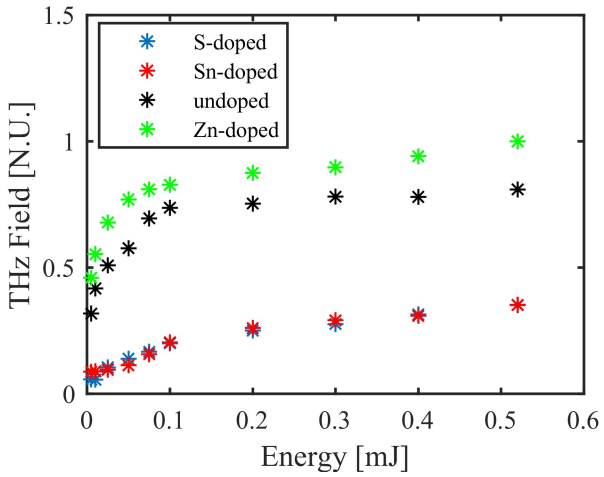

Figure 3.6: The peak THz field has been plotted for various excitation energies, for a number of different freestanding < 100 > InAs substrates, two n-type samples doped with Sn and S donors, one undoped sample and one p-type sample doped with Zn acceptors. The peak THz field has been normalised across all substrates with respect to the maximum field achieved with the Zn-doped InAs.

the phenomenological trend is very similar. This is expected as the available literature concurs about the fact that at high energy OR is the dominant process.

3.3 Temporal smearing in the OPRE measurements

The angle between generating pump and screening pump induces a temporal smearing of the screening effect on the order of 3 ps, because of the induced temporal mismatch of the

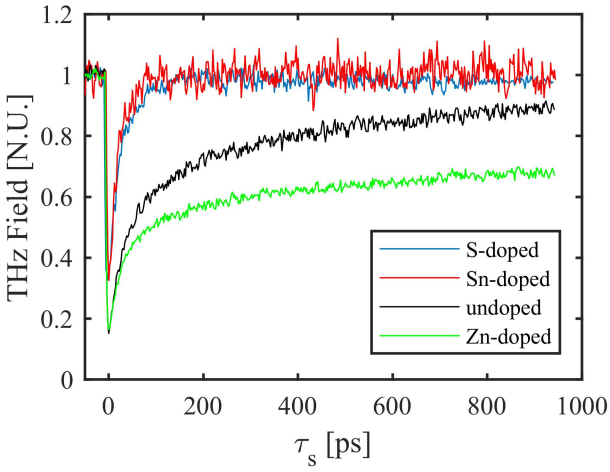

Figure 3.7: OPRE measurements of the peak THz field vs the screening pump delay for the four different freestanding $< 100 >$ InAs substrates of Table. 3.1. Each curve is normalised with respect to the unscreened peak THz field. The energy and illumination conditions of both optical excitations are comparable to one of Fig. 3.3.

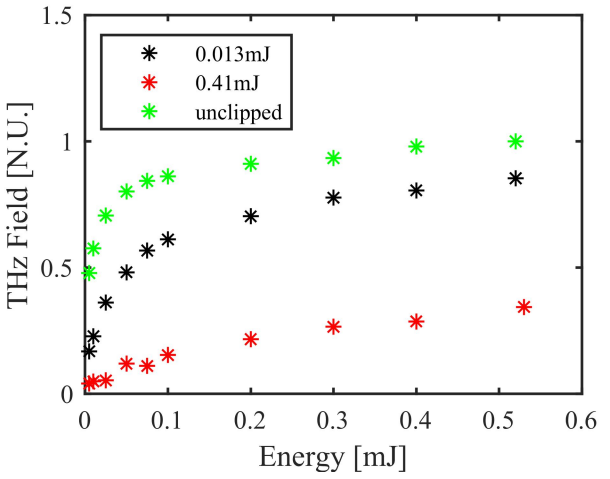

Figure 3.8: The peak THz field has been plotted against W_G, for a Zn-doped $< 100 >$ p-InAs substrate, for various screening energies W_S fixed at $\tau_s = 0$. The peak THz field has been normalised across with respect to the maximum peak field generated by Zn-doped InAs.

wavefronts at the target surface.

To investigate possible artefacts induced by such a smearing, we performed an OPRE measurement detecting the s-polarisation for $< 111 >$ undoped InAs while reducing the size of the THz generating pump to $\sim$ 1 mm diameter and keeping the large screening pump. This corresponds to a maximum smearing estimated within the order of 600 fs. As expected the screening transition appears steeper (the higher noise is induced by the

lower THz field detected). However, no other substantial differences are highlighted by the measurement.

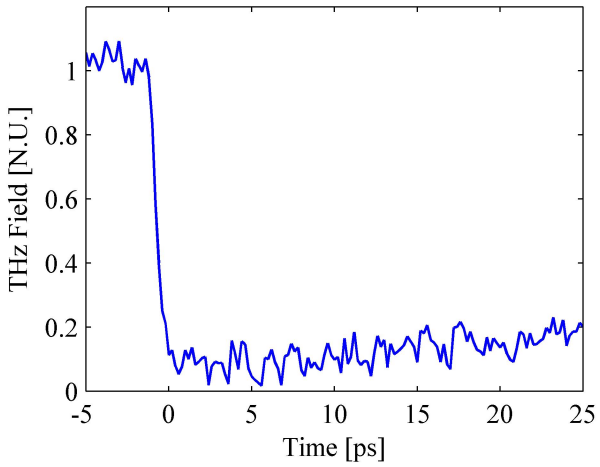

Figure 3.9: OPRE measurement of $< 111 >$ InAs with a reduced impinging optical spot size of $\sim$ 1 mm. The measurement was performed with a generating pump energy W_G of 0.1 mJ and a screening pump energy W_S of 0.1 mJ. The peak THz field has been normalised with respect to the average unscreened field

To further reduce the temporal smearing to negligible scales the OPRE measurement were also performed exploiting a highly focused THz generation. In order to keep a sufficiently high detected THz signal the measurement was carried out using an ultrafast Ti:Sa oscillator (Coherent Chameleon Ultra II) that provides an ultrashort pulse train with 80 MHz repetition rate, 140 fs pulse duration, 4 W average power at a centre wavelength of 800nm.

It is important to stress that to achieve sufficient screening fluences, powers as high as 2.2 W were diverted to the screening pump and focused to a spot size of $\sim$ 0.7 mm. This may result in two potential issues:

(i) the first is common to all pump-and-probe measurements performed using an high-repetition rate source and it is due to the low temporal separation between two consecutive pulses. Because the observed relaxation time for InAs in the experimental conditions is on the scale of ns, the 12.5 ns pulse period is not sufficiently large to ensure the complete decay of all the photo-excited carriers. This means the observed dynamics can in principle be affected by an accumulated screening observable even when the screening pulse impinges after the generation pulse.

(ii) when the screening pump is focused the cross-talk between generation and screening pump increases. Normally, in typical lock-in signal detection, the generating pump is

chopped to introduce an oscillating THz signal. The photo carrier density injected by the generation oscillates as well. Hence, the THz generated by the screening pump is chopped by the screening induced by the generating pump. If the screening pump is Gaussian with 0.7mm FWHM (this case), the resulting THz intensity profile has FWHM on the order of 0.49 mm because of the quadratic relation between pump and THz. The peak spectral efficiency for the InAs emission is usually at a frequency $f_{peak} = 0.7$ THz ($\lambda_{peak} = 427\mu$m) or lower. At 0.7 THz we can estimate a Gaussian beam divergence (half-angle) of about 18.6 degrees. At this angle, the field is still 36% of the maximum and a small fraction of the power is still contained on one side of the beam at larger angles (i.e. a relevant portion of the total field). This means that a good isolation requires very large angles between screening pump and generating pump and small numerical apertures of the THz collecting optics (which has the effect of reducing the detected signal). It is important also to consider that the emitted spectrum also contains much lower frequency components (typically down to 0.3 THz).

There is also another factor that potentially increases the cross-talk at any screening pump size, which is due to the nature of the photocarrier induced modulation. The carrier modulation severely alters the THz emission profile of the screening pump, punching a hole in the THz profile of the typical dimension of the generating pump. Hence, the modulation potentially induces THz scattering at much larger angles, which becomes more visible as the generating pump becomes stronger. For the data presented in Fig. 3.10, the screening pump impinges onto the sample at 10 ° to the normal (i.e. 35 ° between the two pump wave vectors) of the semiconductor surface, which results in a sub-100 fs smearing. There are no fundamental differences in the screening dynamics after excitation compared to the high energy case. However, a modulation in the detected s-polarised field is observed within the timescale of the THz generated by the screening pump at the overlap between the two pulses. For the sake of completeness, at lower generation pump energies the photocarrier modulation is less significant and manifests as an increase in the detected peak field before the main drop (shown in Fig. 3.11(a)), which could be consistent with the phenomenon investigated by Krotkus et al [91]. However, in these experimental conditions, a contamination from the screening pump appears to have a major role as this feature significantly changes with the numerical aperture (NA) of the optics collecting the THz wave and with the screening pump angle. In fact, the oscillation at the edge of the slope in Fig. 3.10 resembles the field profile of the screening pump.

This can be observed in Fig. 3.11(b), where the screening pump impinging angle was

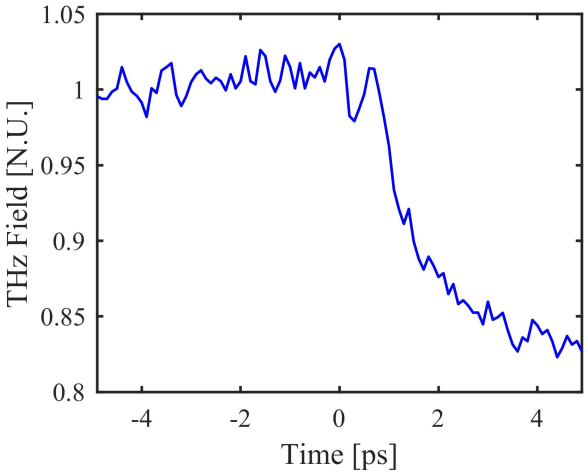

Figure 3.10: S-polarised OPRE traces of < 111 > InAs measured with a focused generation (20μm spot) the screening pump was focused to a spot size of 0.7 mm. The measurements were performed with a generating pump energy W_G of 2 nJ and a screening pump energy W_S of 27.5 nJ. The screening pump impinged onto the sample at 10 ° to the normal

changed such that it counter propagates in the same quadrant of the THz wave vector, at -70 ° from the InAs normal. The increased temporal smearing induced by the large angle is still well within the sub-ps scale. However, this configuration certainly reduces the average fluence which appears to be the only determining factor in the observed dynamics as verified at high energy with larger beams.

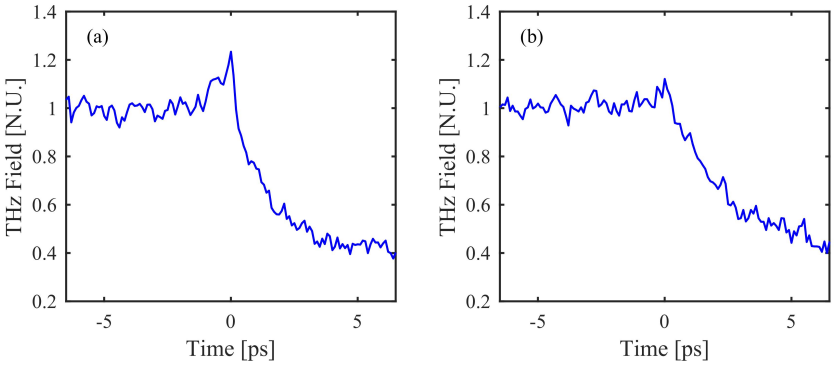

Figure 3.11: S-polarised OPRE traces of < 111 > InAs measured with a focused generation (20μm spot) the screening pump was focused to a spot size of 0.7 mm. The measurements were performed with a generating pump energy W_G of 0.5 nJ and a screening pump energy W_S of 27.5 nJ. In (a) The screening pump impinged onto the sample at 10degrees to the normal. In (b) The screening pump impinged onto the sample -70 ° from the normal.

3.4 Conclusion

In conclusion, a physical process for the saturation of SOR at high fluences has been proposed. It is argued that as the injection of photo-carriers increases, the thickness of the surface field region contracts and a progressively larger fraction of the photocarriers are excited outside of the surface field region. As those carriers do not contribute to the surface field screening, a quadratic conversion trend (i.e. a linear dependence of the peak THz field from the generating pump energy) is eventually re-established at high excitation energies. As confirmation of the main hypothesis, the depth of this surface field layer, and therefore the saturation trend of the substrates, can be controlled with either doping of the material or by injecting an equivalent quantity of photocarriers. I believe this to be a significant advancement in the understanding of the THz surface generation physics at very high excitation and a step forward in the realisation of high energy surface THz emitters.

Chapter 4

Route to Enhancing Surface-Field Emission via 2D-materials

In this chapter, I will explore the experimental investigation of the potential role of 2D-materials, specifically Graphene, in enhancing the surface THz emission of semiconductors. Upon contact, the graphene changes the surface potential of the substrate semiconductor. This results in a change of the in-built depletion surface field with an enhancement of the band-bending in proximity of the surface. This mechanism has been verified through Kelvin Probe Force Microscopy (KPFM) measurements of the relative local potential at the surface. This chapter is being prepared as a paper for publication.

4.1 Background

As discussed in previous chapters, optical THz generation is typically limited by the saturation of the relevant field-matter interaction mechanism [45], the damage threshold of nonlinear crystals or in the lack of suitable velocity-matching between THz and optical pulses in real materials by their inherent absorption in part of the THz spectrum [40]. OR is commonly implemented to generate THz radiation, one of the few methods of increasing the THz emission in bulk OR in nonlinear crystals is to simply increase the thickness of the crystal used (as shown in chapter 1), however, this inherently introduces additional costs and phase matching limitations.

It has been demonstrated in chapter 3 that the quadratic dependence between the emitted THz energy and the excitation is reestablished at high energy as the main saturation mechanism weakens. However increasing the impinging optical energy becomes impractical as the optical damage threshold of the semiconductor is approached [96], it

would, therefore, be greatly beneficial to enhance the surface field to further increase the THz emission energy.

It is then worth investigating methods of enhancing the surface field, once such technique involves biasing the surface using a thin, transparent electrode layer, such as that which has been used to assess the surface potential of silicon surfaces [61]. This will, however, add to the cost and complexity of the system. It would, therefore, be greatly beneficial to introduce a passive bias to the surface interface, which corresponds to a higher local field. Graphene presents a simple and promising material to achieve this aim. Graphene, being a single two-dimensional layer of graphite with zero band gap, has demonstrated remarkable electrical and mechanical properties which have fuelled a vast amount of research into the development of 2D materials [97]. Furthermore, as new exfoliation techniques are developed, the cost of the fabrication process for graphene devices is rapidly decreasing. Liquid Phase Exfoliation (LPE) of graphitic powder represents a cheap and scalable method for the manufacture of graphene flakes dispersed in various solutions [98].

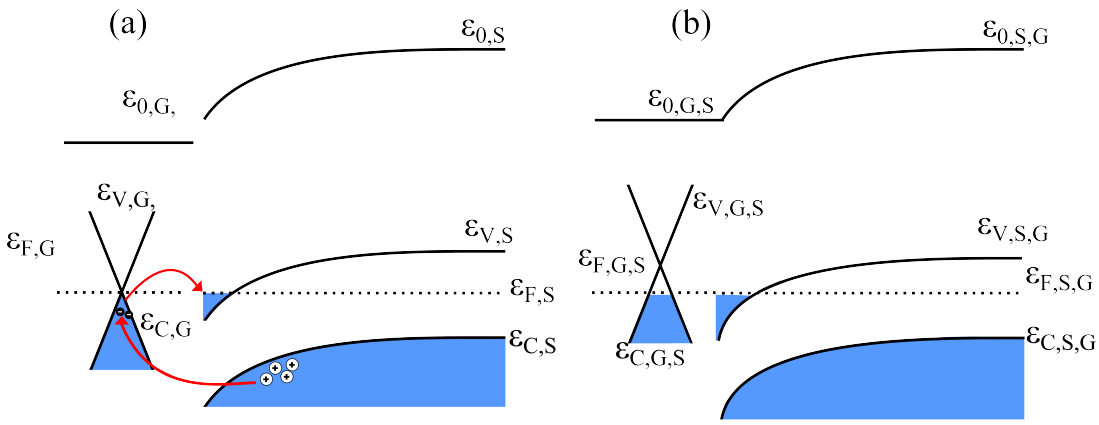

Figure 4.1: Sketch of the Graphene-InAs Schottky junction. (a) Shows the charge transfer due to the Fermi level alignment. $\varepsilon_{0,G}$, $\varepsilon_{V,G}$, $\varepsilon_{F,G}$ and $\varepsilon_{C,G}$ represent the vacuum, valence, Fermi and conduction band levels in the Graphene respectively. $\varepsilon_{0,S}$, $\varepsilon_{V,S}$, $\varepsilon_{F,S}$ and $\varepsilon_{C,S}$ represent the vacuum, valence, Fermi and conduction band levels in the semiconductor respectively. (b) Shows the band structure of the materials after Fermi level alignment. Where $\varepsilon_{0,G,S}$, $\varepsilon_{V,G,S}$, $\varepsilon_{F,G,S}$ and $\varepsilon_{C,G,S}$ represent the vacuum, valence, Fermi and conduction band levels in the Graphene after Fermi level alignment, respectively. $\varepsilon_{0,S,G}$, $\varepsilon_{V,S,G}$, $\varepsilon_{F,S,G}$ and $\varepsilon_{C,S,G}$ represent the vacuum, valence, Fermi and conduction band levels in the semiconductor, after Fermi level alignment, respectively.

Graphene-on-semiconductor based devices have been extensively studied for their rectifying behaviour, triggering a large amount of experimental work on graphene Schottky junction diodes [99, 100]. Due to the fact that the work function of graphene is lower than that of InAs there is a transfer of electrons at the interface as holes flow from the InAs into the graphene. This establishes a greater surface charge than that which is native to the surface states of the semiconductor. The semiconductor band bending response to this results in an additional built-in potential at the interface equivalent to the difference in the material's Fermi levels, as shown in Fig. 4.1. The electric potential close to the surface can be represented by Eq. 4.1.

$$V_b = \frac{1}{e}(\varepsilon_{F,G} - \varepsilon_{F,S}). \tag{4.1}$$

The modification of this potential is an indication of an enhancement of the surface electric field in such a way that it can be exploited to increase the THz field emission via SOR.

4.2 Experiment

The InAs samples used were all undoped with a <100> surface orientation and were 5x5x0.5 mm^3 in dimension. Graphene platelets were prepared via liquid phase deposition of graphite powder in N Methyl-Pyrrolidone (NMP) solution [101] and deposited onto the InAs surface using a Langmuir-Schaefer approach [102]. The experimental setup and procedure are the same as described in Chapter 2.

Fig. 4.2 (a) displays a SEM image depicting graphene flakes self-assembling across the surface, we can observe regions of both monolayer and multilayer graphene platelets. As the concentration of graphene flakes increases, they begin to percolate across the entire sample, a conductive connection will form between the graphene platelets. Fig. 4.2 (b) is a KPFM image of a region of the InAs surface, from which it is evident that the presence of the graphene platelets has fundamentally altered the surface potential with respect to the substrate. It is expected that this alteration in the local work function of the sample will result in these isolated regions emitting a larger peak THz field than that of the rest of the semiconductor. The experimental evidence is an overall increment in the detected THz waveform.

It is worth noting that, graphene has been shown to emit THz radiation through the photon drag effect [103] when Chemical Vapour Deposition (CVD) graphene is illuminated by femtosecond optical pulses. This hypothesis has been tested fabricating a sample of

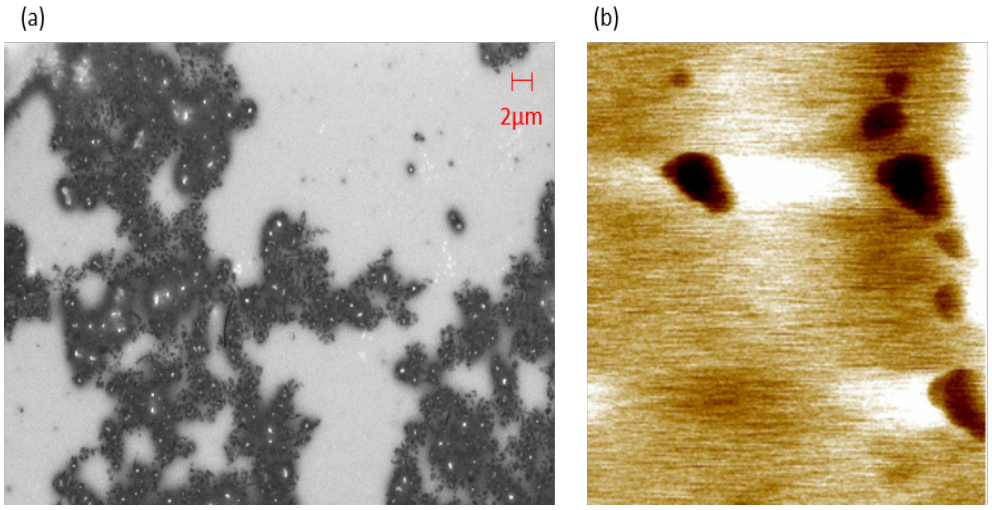

Figure 4.2: (a) Scanning Electron Micrograph of a graphene flake coated InAs surface. The sample shown has a relative density coverage of 1. (b) Kelvin Probe Force Micrograph of the individual graphene platelets, showing the relative work function across the graphene platelets.

graphene flakes on crystalline quartz and on silicon, using the same parameters in the deposition on InAs. It was confirmed that there was no significant emission from the flakes in both reflection and transmission geometries such that it can fully exclude any THz contribution from the flakes themselves.

4.3 Results

Fig. 4.3 displays THz TDS scans of two of the samples, one sample is bare with no graphene coverage and was used as a reference. The second sample was coated with graphene with a relative coverage density of 1.5, relative to the lowest coverage used in this chapter. Both results were normalised to the peak THz field emitted by the bare sample. The peak field enhancement is on the order of 26.6%, which is equivalent to a 60.3% increase in emitted THz power. This enhancement demonstrates that the graphene has altered the surface field in such a way as to increase the emitted field. This enhancement is verified by the KPFM image shown in Fig. 4.2 and demonstrates that the graphene has indeed enhanced the emitted THz field. This modification is fundamentally explained by this local increase in the surface potential induced by the graphene platelets, converging to an accumulative intensification in the detected peak THz field. Furthermore, a change in the waveform can be observed between samples, this suggests that the contributions from the two different mechanisms (the photo-Dember effect and Surface Optical Rectification) do

not scale identically with an increase in the surface field.

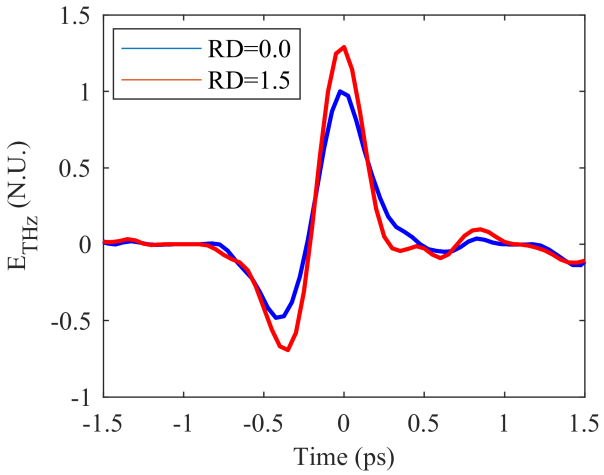

Figure 4.3: THz-TDS scans of an undoped 5x5x0.5 $textrmmm^3$ <100> InAs sample along with a TDS of a sample with a relative density coverage of 1.5, relative to the lowest coverage on a sample used in this chapter. Both TDS scans are normalised to the maximum peak field of the bare InAs sample.

Multiple THz-TDS scans were taken for a variety of samples with different graphene flake coverages. In doing so the emitted peak field was measured and plotted in Fig. 4.4. The graphene-enhanced emission increases to a peak at Relative Density (RD) 1.5 after which any further increase to the relative density produces a detrimental effect on the emitted THz field. This reduction in the THz field occurs due to the high degree of absorption characteristic of monolayer graphene, where many absorption channels are allowed by the zero-bandgap material. Which is in addition to the intrinsically high conductivity of graphene as it begins to percolate across the sample and forming large, macroscopic regions which will attenuate the emitted THz field.

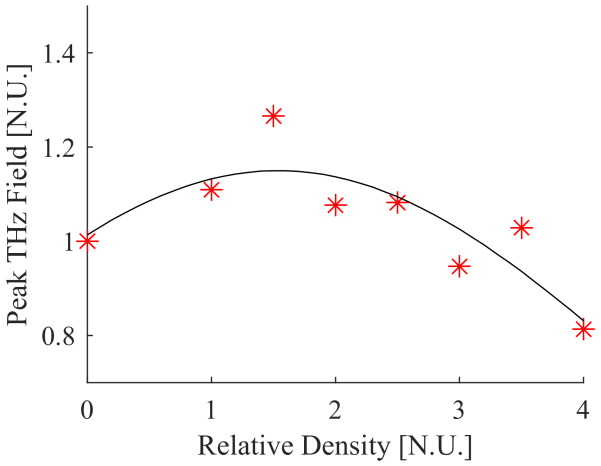

Figure 4.4: The emitted peak THz field as a function of the relative graphene coverage density. The figure is normalised to the maximum peak field of the bare InAs sample. A line of best fit was added to illustrate the trend.

In this chapter, I have demonstrated that a surface concentration of graphene platelets enhances the emitted THz power with an optimal density of RD 1.5. The graphene flakes fundamentally alter the semiconductor surface field responsible for the third order nonlinear conversion while having a negligible impact on the optical pump pulse. As the coverage increases the graphene begins to considerably frustrate the detected THz field, as it percolates across the surface and forms a conductive layer. I believe that this work potentially enables new techniques to passively enhance the surface field of semiconductors and through this passive enhancement increase the viability and impact of the development of ultrathin surface THz emitters.

Chapter 5

All optical rectification from surfaces

Nonlinear optics in sub-wavelength structures play a key role in the development of advanced integrated photonics platforms. Surfaces, nanostructures and 2D media provide an attractive framework for fundamental investigation in light-matter interaction, as they are inherently free from any longitudinal phase matching constraint. To date, however, research has been mostly focused in the optical and near infrared spectral region. In this chapter, it is demonstrated that the generation of terahertz radiation from the nonlinear mixing of purely optical fields at interfaces enabled by the surface third-order nonlinearity. This process is different from the optical rectification field induced symmetry breaking at the medium surface. The terahertz emission is fully controllable by adjusting the relative phase between the interacting optical fields. The terahertz emission from this mechanism has also been analysed to calculate the $\chi^{(3)}$ for the material. The contents of this chapter are being prepared as a paper for publishing.

5.1 Introduction

As discussed in previous chapters, the efficiency of nonlinear frequency conversion is directly related to the longitudinal phase-matching conditions, which are rarely met in macroscopic systems. To achieve phase-matching, standard nonlinear optics applications require expensive materials and complex configurations, such as birefringent crystals or complex periodic stacks. Phase-matching, however, is not relevant in nanoscale structures, whose characteristic sizes are not sufficient to introduce a significant walk-off among the interacting optical fields [104]. This is a significant advantage when designing integrated

applications, which can exploit the large bandwidths inherent to optical nonlinearities. Nanoscale nonlinear systems have been recently employed as a viable platform for a range of technologies [105], which rely on ultrafast refractive index modulation [106, 107, 108] or on the generation of frequencies in the optical and infrared regions via up-frequency conversion (e.g., second or third harmonic generation) [109] and four-wave-mixing [110]. Intuitively, the integration of highly nonlinear materials in nanoscale media could also be employed to generate long wavelength radiation via OR. In recent years, parametric rectification processes in ultrathin structures have been subject of intense research, particularly in the field of THz photonics [111, 112, 113]. As discussed in previous chapters the SOR generation of THz pulses from InAs occurs within a tightly confined volume, placed in proximity of the incidence surface. Such high degree of spatial confinement is a direct consequence of the short skin depth of the optical field. It immediately follows that the SOR process is characterised by a very high conversion efficiency per unit length. An interesting question is whether the static surface field in SOR could be replaced by an optical field oscillating at 2ω In this case the THz electric field would be the result of a four wave mixing process, which I denote as AO-SOR:

$$E_{THz} \propto \chi^{(3)}(\omega_{THz}; 2\omega + \omega_{THz}, -\omega, -\omega) E_{\omega}^{2}(t) E_{2\omega}(t). \tag{5.1}$$

In this context, researchers have initially proposed all-optical SOR as the origin of the high conversion efficiency recorded when focusing an optical pulse and its second harmonic in air [114]. Such interpretation, however, was later disproved in favour of a transient photocurrent originated within the tightly confined focusing region. The transient photocurrent contribution, in fact, largely overcomes the underlying four wave mixing process as widely discussed in [115] and references therein. At the same time, the observation of AO-SOR in solid-state media represents an extremely challenging task, due to the large phase-mismatch between the two optical pulses In the past, two-colour excitation of unbiased silicon substrates has been investigated in the context of ultrafast ballistic electrical currents generation, as discussed in [116] and references therein. In this chapter, we report the observation of this elusive process in a low-bandgap direct semiconductor which exhibits a strong single photon absorption in the NIR band. Owing to its very high nonlinearity and to an interaction length below the coherence length of the AO-SOR process, we were able to successfully observe a measurable THz signal from the mixing of femtosecond pulses at 800 nm and 400 nm.

5.2 Experiment

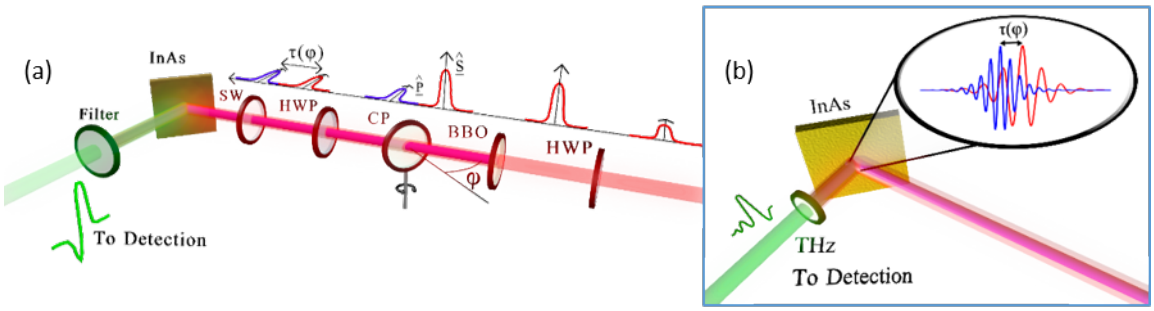

Figure 5.1: Experimental realisation of all-optical surface optical rectification generation from InAs substrates. (a) Schematics of the experimental setup. The red, blue and green beams denote the 800 nm, 400 nm optical and THz beam paths respectively. (b) A schematic view of the role played by the group delay τ_{cp} between fundamental and second harmonic fields, illustrating the phase overlap of the two optical beams on the surface of the InAs substrate. In both panels, the optical components are denoted as HWP: Half-wave plate, BBO: Barium Borate crystal, CP: Calcite plate, SW: UV fused silica window.

Fig. 5.3 (a) illustrates the AO-SOR experimental setup, comprising of a fundamental excitation beam (λ = 800 nm, red beam) co-propagating with its second-harmonic signal (λ = 400 nm, blue beam). The second-harmonic signal was generated on-axis by a non-linear BBO crystal. The polarisation state of the two beams was fixed by a combination of two half-wave plates acting on the fundamental beam and placed before and after the nonlinear crystal. In this configuration, the two beams were co-polarised when reaching the semiconductor surface. As a THz generation surface, we considered an undoped InAs which generated a strong THz field in reflection (green beam). The THz emission was collected and analysed by a TDS setup, similar to previous chapters. Following standard approaches, we included a Calcite Plate (CP) along the optical path to introduce a controllable group delay $\tau_{cp}(\phi)$ between fundamental and second harmonic fields. As Calcite is a highly birefringent material, by entering the crystal with the optical beam p-polarised and the second harmonic beam s polarised the group delay between the two can be controlled by rotating the CP.

5.3 Results and discussion

In this experimental configuration, the total THz field generated in reflection consists of three distinct components such that:

$$E_{THz}^{Total} \propto \chi^{(3)} E_{\omega}^{2}(t) E_{Z}^{surf}(0) + \chi^{(3)} E_{2\omega}^{2} E_{Z}^{surf}(0) + \chi(3) E_{\omega}^{2}(t) E_{2\omega}(t - \tau_{cp} cos(2\omega\tau_{cp}). \quad (5.2)$$

The first two terms account for standard SOR from the fundamental and second-harmonic beams. In this case, the THz field originates from the interaction of each optical beam with the surface depletion field of the semiconductor [81]. The third term, conversely, corresponds to the AO-SOR mechanism, where fundamental and second-harmonic fields interact through a four wave mixing process. As described by Eq. 5.2 the group delay (τ_{cp}) controls the mutual interaction between the fundamental and second harmonic fields. More specifically, by acting on the group delay, it is possible to adjust the relative intensity of the all-optical THz emission, opening to a complete characterisation of the different contributions in Eq. 5.2.

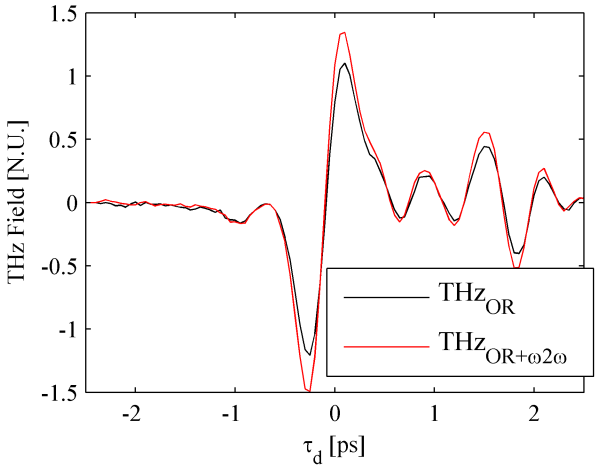

Figure 5.2: Terahertz emitted pulse for $\tau_{cp} = 0$ (red) and $\tau_{cp} = \frac{\pi}{4\omega}$ (black). In both cases, the excitation and detection were p-polarised. The experimental data has been normalised with respect to the THz OR emission peak illustrating the enhancement due to AO-SOR.

When $\tau_{cp} = 0$ (Fig. 5.2, red line), the optical fields are in phase and the total emission is the superposition of the two independent processes. When $\tau_{cp} = \frac{\pi}{4\omega}$, conversely, the two-colour emission is set to zero (Fig. 5.2, black line) and the THz emission is the result of standard SOR. Remarkably, when the fundamental and second-harmonic fields are in phase, the THz field emission is enhanced by a factor of 40%, corresponding to a 96% enhancement in emitted THz power. By comparing the two configurations, it is possible to extract the pulse profile for the two-colour generated field. Fig. 5.3 illustrates the reconstructed surface two-colour emission pulse, it can be seen that it has a much shorter pulse width than that of the surface field induced optical rectification pulse. Thus dis-

playing a larger bandwidth even within the limited detection bandwidth capable through EO sampling in ZnTe.

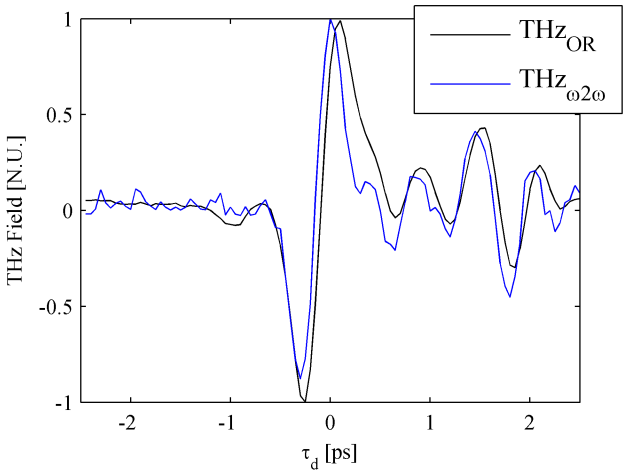

Figure 5.3: The black plot is a typical THz waveform generated by the InAs sample, as a function of the TDS delay t_d.This pulse is the result of Optical Rectification. The blue plot is the extracted surface two-colour emission pulse. Both pulses have been normalised with respect to themselves to highlight the difference in the pulse widths.

Due to the co-existence of SOR and AO-SOR, independently characterising the different contributions to the emitted field is not straightforward. To quantify the amount of carrier-induced THz emission, we performed a full characterisation of the emitted field as a function of the incident polarisation of the two beams. Carrier-induced mechanisms, in fact, are known to be largely unaffected by the incident polarisation direction [25]. Nonlinear parametric phenomena, conversely, have a distinct polarisation dependence, which is the result of the vector properties of the nonlinear susceptibility tensor $\chi^{(n)}$. In the case of standard SOR from InAs for example, the emitted field shows a characteristic two-fold symmetry with respect to the incident polarisation angle, with no emission for s-polarised optical pumps [69]. The two-fold symmetry observed in the SOR emission is a direct consequence of the spatial symmetry of the surface depletion field, which is directed along the depth axis. When considering the AO-SOR case, all the incident fields possess multiple projections along the p and s axes and the polarisation dependence assumes a rather complicated form. As an alternative to polarisation analysis, we characterised the AO-SOR THz emission as a function of the InAs crystal orientation. We report in Fig. 5.4 our experimental results, which were obtained by rotating the generating substrate along the normal to the surface. Theoretical and experimental analysis confirm that SOR from InAs is largely unaffected by a rotation of the semiconductor crystal [69]. When

considering AO-SOR, conversely, we observed a four-fold symmetry with respect to the crystal rotation. When considering p-polarised incident fields and s-polarised detection, for instance, the AO-SOR can be expressed as follows:

$$E_{AO-SOR}(\omega_{THz}) \propto sin(4\varphi)(\chi_{iiii} - 2\chi_{iijj} - \chi_{ijji}), \tag{5.3}$$

where φ is the crystal rotation angle, measured from the 100 axes of the semiconductor, and where χ_{iiii},χ_{iijj} and χ_{ijji} denote three independent components of the nonlinear susceptibility tensor $\chi^{(3)}$. Remarkably, the experimental results reproduce the four-fold symmetry predicted by the theoretical model, as shown in Fig. 5.4

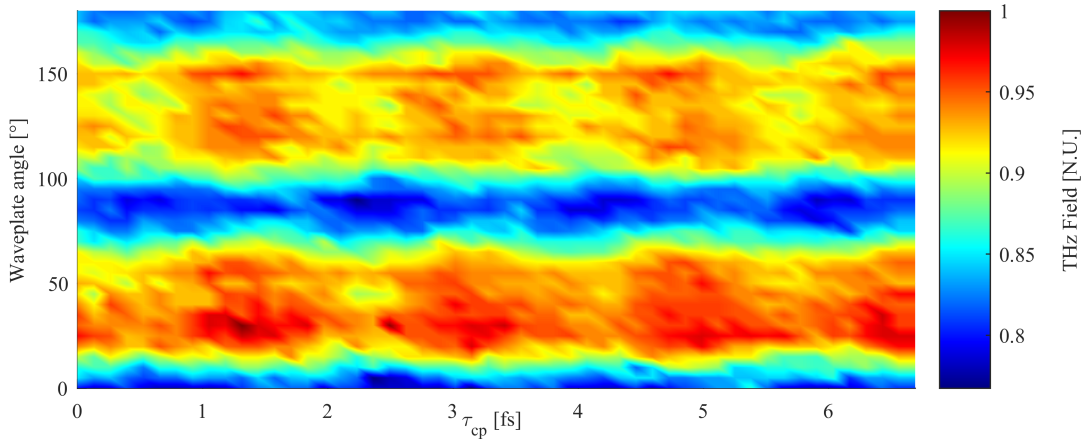

Figure 5.4: Diagram showing the experimental characterisation of SOR THz emission as a function of the waveplate angle and the delay induced by the calcite (τ_{cp}). Both the InAs and the AO-SOR can be seen to be exhibiting a fourfold symmetry.

The group delay induced by the calcite plate, as shown in Eq. 5.2 allows recreating an interference pattern of the two pulses, with a beat note equal to the second harmonic frequency and an envelope proportional to the temporal pulse width. This result is displayed in Fig. 5.5 where the peak THz field as a function of the delay induced by the rotation of the CP is plotted. The zoomed image of the interference pattern includes a fit to the data representing an agreement between the beat note and the second harmonic frequency. In addition, by taking a THz-TDS at the maximum and minimum points of the beating, we can overlap and subtract the two TDS pulses in order to isolate the THz electric field generated solely by the two-colour surface emission.

Further details on the main properties of the AO-SOR emission can be obtained by measuring the input-output diagram for the THz emitted field. Due to the co-existence of SOR and AO-SOR in the experimental setup, we were able to characterise both mech-

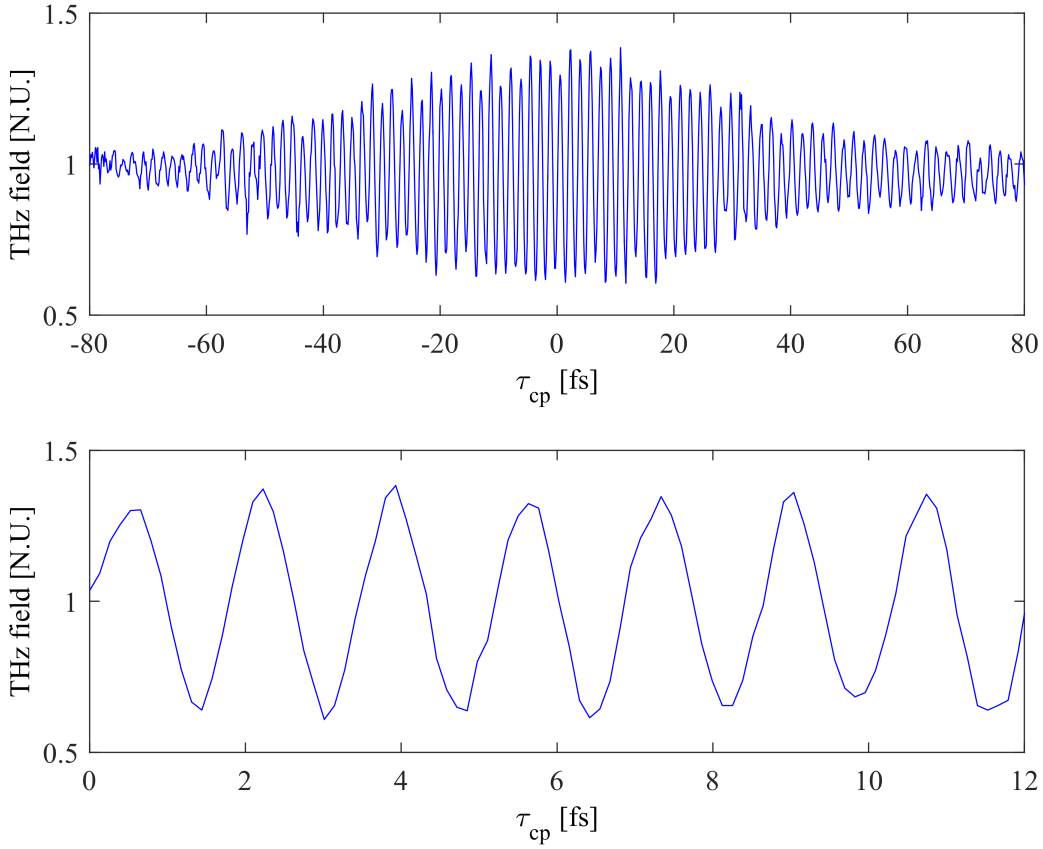

Figure 5.5: The interference pattern from the two-colour surface emission, obtained by rotating the calcite plate. Also shown is an enhanced image of the interference pattern allowing for the period of the beating to be observed. In both plots, the THz field has been normalised with respect to the typical InAs emission.

anisms simultaneously. This experimental characterisation is summarised in Fig. 5.6. As shown in Fig. 5.6 in fact, standard SOR is characterised by the distinctive saturation curve discussed in previous chapters, while AO-SOR does not appear to saturate. It should be noted that Fig. 5.6 (b) is plotted against E^2, the reason for this is that the process is quartic (the THz energy is proportional to E^4 so the field goes quadratic.

A direct comparison with the popular two-colour plasma THz generation in air is not directly possible as this the basic field-matter mechanism is rather different. However we can state that a purely quartic process (two-time quadratic) as the one that arises from the two-colour excitation design of a surface, can result in larger THz bandwidth, which is exactly the main selling point of two-colour THz generation in air. In addition, two-colour process in solids are normally limited by the issue of maintain simultaneous velocity matching of all colours and the generated THz, normally impossible in condensed matter.

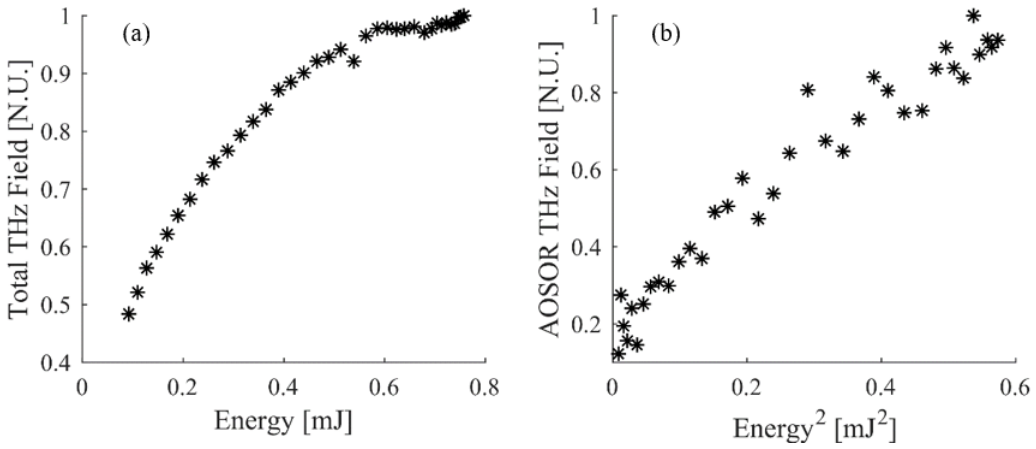

Figure 5.6: The peak THz field has been plotted for various excitation energies, (a) shows the total peak THz field for excitation energies while (b) shows just THz field from AO-SOR, but is plotted against E^2. For both figures, the peak THz field has been normalised with respect to the maximum field value of that figure.

Conversely, by operating in high-absorption regime the typical nonlinear coefficient tend to be very high and the phase-matching is made irrelevant by the nm-scale interaction length (i.e. the penetration depth of the second harmonic).

Furthermore, we can argue that as the generation occurs in such a thin region this THz pulse is not limited by the carrier dynamics in InAs, and does not suffer from the same saturation as surface field-induced emission.

In Surface Optical Rectification for p-polarised incident fields and s-polarised detection, there is no emitted THz field. However for AO-SOR, under the same condition the full form of the THz emission is

$$E_{AO-SOR} = \frac{3}{4} E_{800}^2 E_{400} A_s F_{800}^2 F_{400} \omega_{THz} L_{eff} t_{800}^2 t_{400} sin(4\phi)(\chi_{iiii} - 2\chi_{iijj} - \chi_{ijji}), \quad (5.4)$$

where E_{800} and E_{400} are the electric fields at 800nm and 400nm respectively. A_s is the phase matching coefficient for s. F_{800} and F_{400} are the Fresnel components at 800nm and 400nm respectively. t_{800} and t_{400} are Fresnel transmission coefficients at 800nm and 400nm respectively.ω_{THz} is the THz frequency ϕ is the crystal orientation angle and L_{eff} is the effective length in the medium. Under these conditions, we are able to isolate value for $\chi^{(3)}$ for InAs this value was calculated to be $1.4 \times 10^{-21} \frac{m^2}{V^2}$.

In conclusion, a novel technique for THz generation has been demonstrated, AO-SOR. The emitted THz power is greatly increased over a much thinner propagation distance, thus displaying an increased conversion efficiency per unit length when compared with

standard surface optical rectification. In addition to the emitted THz field enhancement, I have shown that there is a reduction in the temporal THz pulse width generated by the addition of the second harmonic field. This reduction in THz pulse width is inherently tied to an increase in the emitted bandwidth such that I believe this technique has the potential to pave the way to brighter and broader THz sources.

Chapter 6

Conclusion

6.1 Conclusions

Surface terahertz emissions have been studied from ultrathin emitters, in order to more thoroughly understand the emission mechanisms.

A methodology for mapping the DC surface potential of semiconductors was proposed. This methodology relies on Surface Optical Rectification, which is unique in that the terahertz is generated in the DC surface field region. Optical Pump Rectification Emission was verified to be based upon a modulation of the generation which is directly related to the surface potential proven by a linear relationship with the impinging pump energy. This technique could lead to novel methods to inspect semiconductor surfaces, with impact in the fields of electronics, photovoltaics and optical sensors.

The field-matter mechanism responsible for the saturation of Surface optical rectification was investigated. As the population of injected photocarriers increases, the thickness of the surface field of the semiconductor decreases, and a higher quantity of the photocarriers are excited outside of the surface field region. As the carriers generated outside of the surface field region do not contribute to the screening of the surface field, at high excitation energies a quadratic conversion trend is reestablished. This has been proved verifying that the depth of this surface field layer and the saturation of the trends can be controlled with either the doping of the material or by injecting an equivalent number of photocarriers. This is a very significant step forward in the understanding of THz surface generation physics.

I have demonstrated that the THz emission from Surface Optical Rectification can be enhanced beyond the normal efficiency limits with the addition of graphene platelets. This enhancement can be attributed to the graphene flakes inducing a local increase in

the surface field. It was noted however that at higher coverages of graphene flakes, the flakes began to percolate across the sample, forming large regions which ultimately end up attenuating the emitted THz field. This proof-of-concept methodology paves the way for future passive increases in the surface potential of ultrathin emitters potentially allowing for efficient ultrathin THz emitters.

A new generation mechanism of terahertz radiation has been demonstrated. This mechanism, All Optical Surface Optical Rectification, occurs through the nonlinear mixing of purely optical fields at interfaces enabled by the surface third-order nonlinearity. This mechanism has been demonstrated to be fundamentally different to Surface Optical Rectification and can be fully controlled by tuning the phase between the two impinging optical pulses. In addition, the terahertz emission from this mechanism has been analysed to calculate the $\chi^{(3)}$ of the substrate used.

6.2 Future Work

The work undertaken throughout this thesis has raised a few questions, that would require substantially more effort to answer. These questions and insight into future work on the topics will be discussed here.

An investigation will be carried out in the future on the viability of Optical Pump Rectification emission in extracting local values of the surface potential in a semiconductor. Such a technique would hold great promise as an inexpensive tool, with features comparable to Kelvin Probe Force Microscopy, in analysing the surfaces of semiconductors. This methodology would have a great potential impact in the fields of electronics, photovoltaics and optical sensors.

As it has been shown that the limits of the saturation of Surface Optical Rectification can be overcome. It begs the question of how far can these generation efficiencies could be pushed in order to create high-field THz emitter. Some potential ways in which this could be done includes large passive enhancement to the surface field, similar to the way the graphene platelets enhance the terahertz emission. Other possibilities include the manufacturing a custom surface with an extremely high $\chi^{(3)}$ and embedding strong static fields, which might suggest possible implementations using ferroelectric materials. This path has the potential transforming the industrial capabilities of terahertz technologies.

In a more personal view, I believe this work will lead to new research in the fields of ultrathin emitters, with emitters could be either a substrate of InAs thinned down below the micron scale or even an ink, these lines of research are currently being investigated at

the Emergent Photonics Lab. This new generation of efficient thin THz-emitters would be greatly beneficial to the field in light of boosting the integration with current micro and nanotechnologies allowing for an increase in the THz emission bandwidth and would also enable integration with current micro-optics technology. In addition, in near-field imaging the emitter needs to be placed as close to the sample as possible.

Another question that we seek to answer in future works is whether or not ultrathin emitters are practically scalable to a large surface area. Scalable emitters that are based upon ultrathin emitters would be hugely beneficial for the field allowing for significant areas to be illuminated with terahertz radiation simultaneously, something that is not possible with other methods of THz generation. Large scale emitters would allow for fast THz imaging and spectroscopy on large areas, which would be of great benefit to the fields of conservation and security. A Potential use would be allowing the replacement of x-ray machines at airports, with a non-ionising probing allowing for the screening of several passengers and luggage simultaneously.

To close this thesis, it is certainly challenging to give an exact prediction of the next events. This work moves in the proper direction, and I believe it shows that the Terahertz future is definitely not what it used to be, which is is certainly an obvious observation for a young subject, yet it is surprising. One can always hope that the legacy of this work will be the seed of novel works, which is maybe not the most original feeling to end this text, but it is certainly the truth.

Bibliography

[1] L. E. Hargrove, R. L. Fork, and M. A. Pollack. LOCKING OF He–Ne LASER MODES INDUCED BY SYNCHRONOUS INTRACAVITY MODULATION. *Applied Physics Letters*, 5(1):4–5, July 1964. 3

[2] D. H. Auston, A. M. Johnson, P. R. Smith, and J. C. Bean. Picosecond optoelectronic detection, sampling, and correlation measurements in amorphous semiconductors. *Applied Physics Letters*, 37(4):371–373, August 1980. 3

[3] G. Mourou, C. V. Stancampiano, A. Antonetti, and A. Orszag. Picosecond microwave pulses generated with a subpicosecond laserdriven semiconductor switch. *Applied Physics Letters*, 39(4):295–296, August 1981. 3

[4] David H. Auston, K. P. Cheung, J. A. Valdmanis, and D. A. Kleinman. Cherenkov radiation from femtosecond optical pulses in electro-optic media. *Physical Review Letters*, 53(16):1555, 1984. 3

[5] M. B. Ketchen, D. Grischkowsky, T. C. Chen, CC. Chi, I. N. Duling, N. J. Halas, JM. Halbout, J. A. Kash, and G. P. Li. Generation of subpicosecond electrical pulses on coplanar transmission lines. *Applied Physics Letters*, 48(12):751–753, March 1986. 3

[6] K. H. Yang, P. L. Richards, and Y. R. Shen. Generation of FarInfrared Radiation by Picosecond Light Pulses in LiNbO $_3$. *Applied Physics Letters*, 19(9):320–323, November 1971. 3

[7] M. Bass, P. A. Franken, J. F. Ward, and G. Weinreich. Optical rectification. *Physical Review Letters*, 9(11):446, 1962. 3, 14

[8] D. H. Auston, K. P. Cheung, J. A. Valdmanis, and D. A. Kleinman. Cherenkov radiation from femtosecond optical pulses in electro-optic media. *Physical Review Letters*, 53(16):1555, 1984. 3, 4

[9] Masayoshi T. Cutting-edge terahertz technology. *Nature Photonics*, 1(2):97–105, 2007. 03515. 3, 4

[10] K. Sakai, editor. *Terahertz optoelectronics*. Number v. 97 in Topics in applied physics. Springer ; NiCT, National Institute of Information and Communications Technology, Berlin ; New York : [Tokyo], 1st ed edition, 2005. 3

[11] D. Zimdars and J. S. White. Terahertz reflection imaging for package and personnel inspection. In *2004 Conference on Terahertz for Military and Security applications*, 2004. 3

[12] J. Sun, J. Shen, L. Liang, X. Xu, H. Liu, and C. Zhang. Experimental Investigation on Terahertz Spectra of Amphetamine Type Stimulants. *Chinese Physics Letters*, 22(12):3176–3178, 2005. 3

[13] N. Li, J. Shen, J. Sun, L. Liang, X. Xu, M. Lu, and Y. Jia. Study on the THz spectrum of methamphetamine. *Optics Express*, 13(18):6750–6755, 2005. 3

[14] T. Kishi, T. Kanamori, K. Tsujikawa, Y. T. Iwata, H. Inoue, O. Ohtsuru, H. Hoshina, C. Otani, and K. Kawase. Differentiation of optical active form and racemic form of amphetamine-type stimulants by terahertz spectroscopy. In *2005 Joint 30th International Conference on Infrared and Millimeter Waves and 13th International Conference on Terahertz Electronics*, volume 1, pages 184–185 vol. 1, September 2005. 4

[15] K. Kawase, Y. Ogawa, Y. Watanabe, and H. Inoue. Non-destructive terahertz imaging of illicit drugs using spectral fingerprints. *Optics Express*, 11(20):2549–2554, 2003. 4

[16] L. Chaix, S. de Brion, F. Lévy-Bertrand, V. Simonet, R. Ballou, B. Canals, P. Lejay, J. B. Brubach, G. Creff, F. Willaert, P. Roy, and A. Cano. THz Magnetoelectric Atomic Rotations in the Chiral Compound Ba 3 NbFe 3 Si 2 O 14. *Physical Review Letters*, 110(15), April 2013. 4

[17] D. L. Shenkenberg. CHECK POINT. *Photonics Spectra*, 2008. 4

[18] J. Valdmanis, G. Mourou, and C. Gabel. Subpicosecond electrical sampling. *IEEE Journal of Quantum Electronics*, 19(4):664–667, April 1983. 4

[19] C. Seco-Martorell, V. López-Domínguez, G. Arauz-Garofalo, A. Redo-Sanchez, J. Palacios, and J. Tejada. Goya's artwork imaging with Terahertz waves. *Optics Express*, 21(15):17800, July 2013. 5

[20] V Apostolopoulos and M E Barnes. THz emitters based on the photo-Dember effect. *Journal of Physics D: Applied Physics*, 47(37):374002–374002, September 2014. 00031. 8, 41

[21] P. Gu, M. Tani, S. Kono, K. Sakai, and X. C. Zhang. Study of terahertz radiation from InAs and InSb. *Journal of Applied Physics*, 91(9):5533–5537, 2002. 00277. 8, 10, 41

[22] H. Dember. Über eine photoelektronische kraft in kupferoxydul-kristallen. *Phys. Zeits.*, 32(554), 1931. 00000. 8

[23] V. L. Malevich, R. Adomavičius, and A. Krotkus. THz emission from semiconductor surfaces. *Comptes Rendus Physique*, 9(2):130–141, March 2008. 8

[24] M. C. Beard, G. M. Turner, and C. A. Schmuttenmaer. Subpicosecond carrier dynamics in low-temperature grown GaAs as measured by time-resolved terahertz spectroscopy. *Journal of Applied Physics*, 90(12):5915–5923, December 2001. 8

[25] K. Liu, J. Xu, T. Yuan, and X.-C. Zhang. Terahertz radiation from InAs induced by carrier diffusion and drift. *Physical Review B*, 73(15):155330–155330, April 2006. 8, 41, 64

[26] M. B. Johnston, D. M. Whittaker, A. Dowd, A. G. Davies, E. H. Linfield, X. Li, and D. A. Ritchie. Generation of high-power terahertz pulses in a prism. *Optics letters*, 27(21):1935–1937, 2002. 8

[27] S. Kono, P. Gu, M. Tani, and K. Sakai. Temperature dependence of terahertz radiation from n-type InSb and n-type InAs surfaces:. *Applied Physics B*, 71(6):901–904, December 2000. 8, 9

[28] J. N. Heyman, N. Coates, A. Reinhardt, and G. Strasser. Diffusion and drift in terahertz emission at GaAs surfaces. *Applied Physics Letters*, 83(26):5476–5478, December 2003. 8, 10

[29] T. Dekorsy, X. Q. Zhou, K. Ploog, and H. Kurz. Subpicosecond electric field dynamics in low-temperature-grown GaAs observed by reflective electro-optic sampling. *Materials Science and Engineering: B*, 22(1):68–71, 1993. 00006. 8, 34

[30] Thomas Dekorsy, Holger Auer, Huib J. Bakker, Hartmut G. Roskos, and Heinrich Kurz. THz electromagnetic emission by coherent infrared-active phonons. *Physical Review B*, 53(7):4005, 1996. 8

[31] W. Mönch. *Semiconductor Surfaces and Interfaces*, volume 26 of *Springer Series in Surface Sciences*. Springer Berlin Heidelberg, Berlin, Heidelberg, 2001. 8, 22

[32] M. C. Nuss, D. H. Auston, and F. Capasso. Direct subpicosecond measurement of carrier mobility of photoexcited electrons in gallium arsenide. *Physical Review Letters*, 58(22):2355, 1987. 10, 23

[33] S. C. Howells, S. D. Herrera, and L. A. Schlie. Infrared wavelength and temperature dependence of optically induced terahertz radiation from InSb. *Applied Physics Letters*, 65(23):2946–2948, December 1994. 10

[34] R A Lewis. A review of terahertz sources. *Journal of Physics D: Applied Physics*, 47(37):374001, September 2014. 10

[35] R. Ascázubi, I. Wilke, K. Denniston, H. Lu, and W. J. Schaff. Terahertz emission by InN. *Applied Physics Letters*, 84(23):4810–4812, June 2004. 10

[36] X.C. Zhang and D. H. Auston. Optoelectronic measurement of semiconductor surfaces and interfaces with femtosecond optics. *Journal of Applied Physics*, 71(1):326–338, January 1992. 10

[37] J. Shan and T. F. Heinz. Terahertz radiation from semiconductors. In *Ultrafast Dynamical Processes in Semiconductors*, pages 1–56. Springer, 2004. 10

[38] P. Gu and M. Tani. *Terahertz Radiation from Semiconductor Surfaces*, volume 97 of *Springer Topics in Appled Physics*. Springer Berlin Heidelberg, Berlin, Heidelberg, 2005. 10

[39] Y. Ko. *lectrical, optical, and THz emission studies of GaxIn1-xAs bulk crystals*. Department of Electrical, Computer, and Systems Engineering, Doctoral Thesis, Rensselaer, Polytechnic Institute Troy, NY, 2007. 10

[40] G. Gallot, Jiangquan Zhang, R. W. McGowan, Tae-In Jeon, and D. Grischkowsky. Measurements of the THz absorption and dispersion of ZnTe and their relevance to the electro-optic detection of THz radiation. *Applied Physics Letters*, 74(23):3450–3450, 1999. 00247. 15, 54

[41] D. T. F. Marple. Refractive Index of ZnSe, ZnTe, and CdTe. *Journal of Applied Physics*, 35(3):539–542, March 1964. 15

[42] Shun Lien Chuang, Stefan Schmitt-Rink, Benjamin I. Greene, Peter N. Saeta, and Anthony FJ Levi. Optical rectification at semiconductor surfaces. *Physical Review Letters*, 68(1):102, 1992. 00339. 15, 24, 41, 42

[43] Y. R. Shen. Surface properties probed by second-harmonic and sum-frequency generation.pdf. *Nature*, 337:519–525, February 1989. 16, 28

[44] A. Rice, Y. Jin, X. F. Ma, X.C. Zhang, D. Bliss, J. Larkin, and M. Alexander. Terahertz optical rectification from 110 zincblende crystals. *Applied Physics Letters*, 64(11):1324–1326, March 1994. 17, 28

[45] L. Peters, J. Tunesi, A. Pasquazi, and M. Peccianti. Optical Pump Rectification Emission: Route to Terahertz Free-Standing Surface Potential Diagnostics. *Scientific Reports*, 7(1), December 2017. 22, 41, 54

[46] François Léonard and J. Tersoff. Role of Fermi-level pinning in nanotube Schottky diodes. *Physical Review Letters*, 84(20):4693, 2000. 00000. 22

[47] M. Burgelman, P. Nollet, and S. Degrave. Modelling polycrystalline semiconductor solar cells. *Thin Solid Films*, 361:527–532, 2000. 00521. 22

[48] J. F. O'Hara, R. Singh, I. Brener, E. Smirnova, J. Han, A. J. Taylor, and W. Zhang. Thin-film sensing with planar terahertz metamaterials: sensitivity and limitations. *Optics Express*, 16(3):1786–1795, 2008. 22

[49] A. Brodde, St. Tosch, and H. Neddermeyer. Scanning tunnelling microscopy and spectroscopy on Cu(111) and Au(111). *Journal of Microscopy*, 152(2):441–448, 1988. 00018. 23

[50] G. Hörmandinger. Imaging of the Cu (111) surface state in scanning tunneling microscopy. *Physical Review B*, 49(19):13897, 1994. 00000. 23

[51] N. Horiuchi. Terahertz technology: Endless applications. *Nat Photon*, 4(3):140–140, March 2010. 00000. 23

[52] B. I. Greene, J. F. Federici, D. R. Dykaar, A. F. J. Levi, and L. Pfeiffer. Picosecond pump and probe spectroscopy utilizing freely propagating terahertz radiation. *Optics letters*, 16(1):48–49, 1991. 00087. 23

[53] M. C. Beard, G. M. Turner, and C. A. Schmuttenmaer. Terahertz Spectroscopy. *The Journal of Physical Chemistry B*, 106(29):7146–7159, July 2002. 00493. 23

[54] R. Ulbricht, E. Hendry, J Shan, T. F. Heinz, and M. Bonn. Carrier dynamics in semiconductors studied with time-resolved terahertz spectroscopy. *Reviews of Modern Physics*, 83(2):543–586, June 2011. 23

[55] P. Uhd Jepsen, W. Schairer, I. H. Libon, U. Lemmer, N. E. Hecker, M. Birkholz, K. Lips, and M. Schall. Ultrafast carrier trapping in microcrystalline silicon observed in optical pump–terahertz probe measurements. *Applied Physics Letters*, 79(9):1291, 2001. 23

[56] H. J Joyce, C. J Docherty, Q. Gao, H. Tan, C. Jagadish, J. Lloyd-Hughes, L. M. Herz, and M. B. Johnston. Electronic properties of GaAs, InAs and InP nanowires studied by terahertz spectroscopy. *Nanotechnology*, 24(21):214006, May 2013. 00000. 23

[57] D. E. Aspnes and A. A. Studna. Dielectric functions and optical parameters of si, ge, gap, gaas, gasb, inp, inas, and insb from 1.5 to 6.0 ev. *Physical Review B*, 27(2):985, 1983. 03119. 23, 25, 28, 32, 41

[58] Y. Sakai, I. Kawayama, H. Nakanishi, and M. Tonouchi. Visualization of GaN surface potential using terahertz emission enhanced by local defects. *Scientific Reports*, 5:13860, September 2015. 23, 24

[59] M. Tonouchi. Dynamic terahertz emission microscope. In *2010 Conference Proceedings ICECom, 20th International Conference on Applied Electromagnetics and Communications*, pages 1–2, September 2010. 23

[60] H. Nakanishi, A. Ito, K. Takayama, I. Kawayama, H. Murakami, and M. Tonouchi. Visualization of Photoexcited Carrier Responses in a Solar Cell Using Optical Pump—Terahertz Emission Probe Technique. *Journal of Infrared, Millimeter, and Terahertz Waves*, 37(5):498–506, 2016. 24

[61] T. Mochizuki, A. Ito, J. Mitchell, H. Nakanishi, K. Tanahashi, I. Kawayama, M. Tonouchi, K. Shirasawa, and H. Takato. Probing the surface potential of oxidized silicon by assessing terahertz emission. *Applied Physics Letters*, 110(16):163502, April 2017. 24, 55

[62] V. Mag-usara, S. Funkner, G. Niehues, E. Prieto, M. Balgos, A. Somintac, E. Estacio, A. Salvador, K. Yamamoto, Mu. Hase, and M. Tani. Low temperature-grown GaAs carrier lifetime evaluation by double optical pump terahertz time-domain emission spectroscopy. *Optics Express*, 24(23):26175, November 2016. 24, 36, 45

[63] J.B. Héroux and M. Kuwata-Gonokami. Photoexcited Carrier Dynamics in InAs, GaAs, and InSb Probed by Terahertz Excitation Spectroscopy. *Physical Review Applied*, 7(5), May 2017. 24, 32

[64] C. A. Mead and W. G. Spitzer. Fermi level position at semiconductor surfaces. *Physical Review Letters*, 10(11):471, 1963. 24

[65] R. Valdés Aguilar, A. V. Stier, W. Liu, L. S. Bilbro, D. K. George, N. Bansal, L. Wu, J. Cerne, A. G. Markelz, S. Oh, and N. P. Armitage. Terahertz Response and Colossal Kerr Rotation from the Surface States of the Topological Insulator Bi 2 Se 3. *Physical Review Letters*, 108(8), February 2012. 24

[66] G. Kaur, P. Han, and X.-C. Zhang. Transmission coefficient enhancement in undoped Indium Arsenide by high THz field. In *Lasers and Electro-Optics (CLEO), 2011 Conference on*, pages 1–2. IEEE, 2011. 00000. 25

[67] D. Grischkowsky, Søren Keiding, Martin Van Exter, and Ch Fattinger. Far-infrared time-domain spectroscopy with terahertz beams of dielectrics and semiconductors. *JOSA B*, 7(10):2006–2015, 1990. 01931. 26

[68] H.-E. Ponath and G. I. Stegeman, editors. *Nonlinear surface electromagnetic phenomena*. Number v. 29 in Modern problems in condensed matter sciences. North-Holland, Elsevier Science Pub. Co, Amsterdam ; New York : New York, NY, USA, 1991. 26

[69] M. Reid, I. V. Cravetchi, and R. Fedosejevs. Terahertz radiation and second-harmonic generation from InAs: Bulk versus surface electric-field-induced contributions. *Physical Review B - Condensed Matter and Materials Physics*, 72(3):1–9, 2005. 27, 41, 44, 64

[70] Hans L. *Solid Surfaces, Interfaces and Thin Films*. Graduate Texts in Physics. Springer International Publishing, Cham, 2015. 00576 DOI: 10.1007/978-3-319-10756-1. 28

[71] L. Ö. Olsson, C. B. M. Andersson, M. C. Håkansson, J. Kanski, L. Ilver, and U. O. Karlsson. Charge accumulation at inas surfaces. *Phys. Rev. Lett.*, 76:3626–3629, May 1996. 29

[72] H. S. Karlsson, G. Ghiaia, and Ulf O. Karlsson. Electron dynamics and accumulation on the InAs (110) surface. *Surface science*, 407(1-3):L687–L692, 1998. 29

[73] S. Kawaji and H. C. Gatos. Electric field effect on the magnetoresistance of indium arsenide surfaces in high magnetic fields. *Surface Science*, 7(2):215–228, June 1967. 00000. 29, 43

[74] J. Heyman, P. Neocleous, D. Hebert, P. Crowell, T. Müller, and K. Unterrainer. Terahertz emission from GaAs and InAs in a magnetic field. *Physical Review B*, 64(8):1–7, 2001. 00145. 30, 31

[75] A. Reklaitis. Terahertz emission from InAs induced by photo-Dember effect: Hydrodynamic analysis and Monte Carlo simulations. *Journal of Applied Physics*, 108(5):053102, 2010. 31, 35, 43

[76] M. Reid and R. Fedosejevs. Terahertz emission from (100) InAs surfaces at high excitation fluences. *Applied Physics Letters*, 86(1):011906–011906, 2005. 31, 32

[77] Q. Wu, M. Litz, and X.C. Zhang. Broadband detection capability of ZnTe electro-optic field detectors. *Applied Physics Letters*, 68(21):2924–2926, May 1996. 32

[78] S. A. Kovalenko. Descartes-Snell law of refraction with absorption. *Semiconductor Physics, Quantum Electronics & Optoelectronics*, 4(3):214–218, 2001. 00000. 32

[79] T. B. A. Senior and J. L. Volakis. *Approximate boundary conditions in electromagnetics*. Institution of Electrical Engineers, London, 1995. OCLC: ocm32509096. 34

[80] Gaofang Li, Xin Xue, Xian Lin, Sannan Yuan, Naiyun Tang, Fenghong Chu, Haoyang Cui, and Guohong Ma. Evolution of terahertz conductivity in ZnSe nanocrystal investigated with optical-pump terahertz-probe spectroscopy. *Applied Physics A*, 116(1):45–50, July 2014. 00000. 36

[81] L. Peters, J. Tunesi, A. Pasquazi, and M. Peccianti. High-energy terahertz surface optical rectification. *Nano Energy*, 46:128 – 132, 2018. 40, 63

[82] R. Adomavičius, A. Urbanowicz, G. Molis, A. Krotkus, and E. Šatkovskis. Terahertz emission from p-lnAs due to the instantaneous polarization. *Applied Physics Letters*, 85(13):2463, 2004. 00105. 41

[83] M. B. Johnston, D. M. Whittaker, A. Corchia, A. G. Davies, and E. H. Linfield. Simulation of terahertz generation at semiconductor surfaces. *Physical Review B*, 65(16), March 2002. 00307. 41

[84] G. D. Chern, E. D. Readinger, H. Shen, M. Wraback, C. S. Gallinat, G. Koblmüller, and J. S. Speck. Excitation wavelength dependence of terahertz emission from InN and InAs. *Applied Physics Letters*, 89(14):141115, 2006. 00094. 41

[85] Georgi L. Dakovski, Brian Kubera, and Jie Shan. Localized terahertz generation via optical rectification in ZnTe. *Journal of the Optical Society of America B*, 22(8):1667–1667, 2005. 00050. 41

[86] R. Mendis, M. L. Smith, L. J. Bignell, R. E. M. Vickers, and R. a. Lewis. Strong terahertz emission from (100) p-type InAs. *Journal of Applied Physics*, 98(12):126104–126104, 2005. 41

[87] H. Takahashi, A. Quema, R. Yoshioka, S. Ono, and N. Sarukura. Excitation fluence dependence of terahertz radiation mechanism from femtosecond-laser-irradiated InAs under magnetic field. *Applied Physics Letters*, 83(6):1068–1070, 2003. 41

[88] I. Nevinskas, K. Vizbaras, A. Trinknas, R. Butkut, and A. Krotkus. Terahertz pulse generation from (111)-cut InSb and InAs crystals when illuminated by 155-m femtosecond laser pulses. *Optics Letters*, 42(13):2615, July 2017. 41

[89] P. Cicnas, A. Geižutis, V. L. Malevich, and A. Krotkus. Terahertz radiation from an InAs surface due to lateral photocurrent transients. *Optics Letters*, 40(22):5164, November 2015. 41

[90] Y. V. Malevich, R. Adomavičius, A. Krotkus, and V. L. Malevich. Anisotropic picosecond photoconductivity caused by optical alignment of electron momenta in cubic semiconductors. *Journal of Applied Physics*, 115(7):073103, February 2014. 41

[91] A. Krotkus, R. Adomaviius, G. Molis, and V. L. Malevich. Terahertz emission from inas surfaces excited by femtosecond laser pulses. *Journal of Nanoelectronics and Optoelectronics*, 2(1):108–114, 2007. 41, 51

[92] K. Smit, L. Koenders, and W. Monch. Adsorption of chlorine and oxygen on cleaved InAs(110) surfaces: Raman spectroscopy, photoemission spectroscopy, and Kelvin probe measurements. *Journal of Vacuum Science & Technology B: Microelectronics and Nanometer Structures*, 7(4):888, July 1989. 43

[93] L. F. J. Piper, T. D. Veal, M. J. Lowe, and C. F. McConville. Electron depletion at InAs free surfaces: Doping-induced acceptorlike gap states. *Physical Review B*, 73(19), May 2006. 43

[94] Q. Wu and X.C. Zhang. Ultrafast electrooptic field sensors. *Applied Physics Letters*, 68(12):1604–1606, March 1996. 43

[95] B.-Y. Hsieh, N. Wang, and M. Jarrahi. Toward ultrafast pump-probe measurements at the nanoscale. *Opt. Photon. News*, 22(12):48–48, Dec 2011. 45

[96] S.S. Mao, F. Qur, S. Guizard, X. Mao, R.E. Russo, G. Petite, and P. Martin. Dynamics of femtosecond laser interactions with dielectrics. *Applied Physics A*, 79(7), November 2004. 54

[97] A. K. Geim and K. S. Novoselov. The rise of graphene. *Nature Materials*, 6:183, March 2007. 55

[98] K. R. Paton, E. Varrla, C. Backes, R. J. Smith, U. Khan, A. O'Neill, C. Boland, M. Lotya, O. M. Istrate, P. King, T. Higgins, S. Barwich, P. May, P. Puczkarski, I Ahmed, M. Moebius, H. Pettersson, E. Long, J. Coelho, S. E. O'Brien, E. K. McGuire, B. M. Sanchez, G. S. Duesberg, N. McEvoy, T. J. Pennycook, C. Downing, A. Crossley, V. Nicolosi, and J. N. Coleman. Scalable production of large quantities of defect-free few-layer graphene by shear exfoliation in liquids. *Nature Materials*, 13(6):624–630, June 2014. 55

[99] D. Sinha and J. U. Lee. Ideal Graphene/Silicon Schottky Junction Diodes. *Nano Letters*, 14(8):4660–4664, August 2014. 56

[100] A. Di Bartolomeo. Graphene Schottky diodes: An experimental review of the rectifying graphene/semiconductor heterojunction. *Physics Reports*, 606:1–58, January 2016. 56

[101] Y. Hernandez, V. Nicolosi, M. Lotya, F. M. Blighe, Z. Sun, S. De, I. T. McGovern, B. Holland, M. Byrne, Y. K. Gun'Ko, J. J. Boland, P. Niraj, G. Duesberg, S. Krishnamurthy, R. Goodhue, J. Hutchison, V. Scardaci, A. C. Ferrari, and J. N. Coleman.

High-yield production of graphene by liquid-phase exfoliation of graphite. *Nature Nanotechnology*, 3:563, August 2008. 56

[102] R. Y. N. Gengler, A. Veligura, A. Enotiadis, E. K. Diamanti, D. Gournis, C. Józsa, B. J. van Wees, and P. Rudolf. Large-Yield Preparation of High-Electronic-Quality Graphene by a Langmuir–Schaefer Approach. *Small*, 6(1):35–39, January 2010. 56

[103] P. A. Obraztsov, N. Kanda, K. Konishi, M. Kuwata-Gonokami, S. V. Garnov, A. N. Obraztsov, and Y. P. Svirko. Photon-drag-induced terahertz emission from graphene. *Physical Review B*, 90(24), December 2014. 56

[104] M. Zhao, Z. Ye, R. Suzuki, Y. Ye, H. Zhu, J. Xiao, Y. Wang, Y. Iwasa, and X. Zhang. Atomically phase-matched second-harmonic generation in a 2d crystal. *Light: Science &Amp; Applications*, 5:e16131, August 2016. 60

[105] N. Kinsey, M. Ferrera, V. M. Shalaev, and A. Boltasseva. Examining nanophotonics for integrated hybrid systems: a review of plasmonic interconnects and modulators using traditional and alternative materials. *J. Opt. Soc. Am. B*, 32(1):121–142, Jan 2015. 61

[106] A. Melikyan, L. Alloatti, A. Muslija, D. Hillerkuss, P. C. Schindler, J. Li, R. Palmer, D. Korn, S. Muehlbrandt, D. Van Thourhout, B. Chen, R. Dinu, M. Sommer, C. Koos, M. Kohl, W. Freude, and J. Leuthold. High-speed plasmonic phase modulators. *Nature Photonics*, 8:229, February 2014. 61

[107] M. Zahirul Alam, Israel De Leon, and Robert W. Boyd. Large optical nonlinearity of indium tin oxide in its epsilon-near-zero region. *Science*, 352(6287):795–797, 2016. 61

[108] M. Clerici, N. Kinsey, C. DeVault, J. Kim, E. G. Carnemolla, L. Caspani, A. Shaltout, D. Faccio, V. Shalaev, A. Boltasseva, and M. Ferrera. Controlling hybrid nonlinearities in transparent conducting oxides via two-colour excitation. *Nature Communications*, 8:15829, June 2017. 61

[109] X. Yin, Z. Ye, D. A. Chenet, Y. Ye, K. O'Brien, J. C. Hone, and X. Zhang. Edge Nonlinear Optics on a MoS2 Atomic Monolayer. *Science*, 344(6183):488–490, 2014. 61

[110] S. M. Rao, A. Lyons, T. Roger, M. Clerici, N. I. Zheludev, and D. Faccio. Geometries

for the coherent control of four-wave mixing in graphene multilayers. *Scientific Reports*, 5:15399, October 2015. 61

[111] Y. Huang, L. Zhu, Q. Zhao, Y. Guo, Z. Ren, J. Bai, and X. Xu. Surface Optical Rectification from Layered MoS2 Crystal by THz Time-Domain Surface Emission Spectroscopy. *ACS Applied Materials & Interfaces*, 9(5):4956–4965, February 2017. 61

[112] J. Maysonnave, S. Huppert, F. Wang, S. Maero, C. Berger, W. de Heer, T. B. Norris, L. A. De Vaulchier, S. Dhillon, J. Tignon, R. Ferreira, and J. Mangeney. Terahertz Generation by Dynamical Photon Drag Effect in Graphene Excited by Femtosecond Optical Pulses. *Nano Letters*, 14(10):5797–5802, October 2014. 61

[113] Vl. A. Margulis, E. E. Muryumin, and E. A. Gaiduk. Three-wave collinear difference-frequency mixing and terahertz coherent emission from gapped graphene. *Physica B: Condensed Matter*, 479:143–148, December 2015. 61

[114] D. J. Cook and R. M. Hochstrasser. Intense terahertz pulses by four-wave rectification in air. *Optics letters*, 25(16):1210–1212, 2000. 61

[115] K. Y. Kim, J. H. Glownia, A. J. Taylor, and G. Rodriguez. Terahertz emission from ultrafast ionizing air in symmetry-broken laser fields. *Opt. Express*, 15(8):4577–4584, Apr 2007. 61

[116] L. Costa, M. Betz, M. Spasenović, A. D. Bristow, and H. M. van Driel. All-optical injection of ballistic electrical currents in unbiased silicon. *Nature Physics*, 3:632, July 2007. 61

Appendix A

Experimental Design and Calibration

I joined the Emergent Photonics Lab in 2014, when the lab comprised of just an ultrafast oscillator running a THz antenna system, hosted on an optical table in the lab of another group.

However, almost immediately the lab experienced exponential growth during my PhD, with about £1M in equipment acquired in the first four years of activities. Hence I spent the first year of my PhD setting the first high energy THz system ever constructed at the University of Sussex.

In this appendix, I will focus on the calibration and characterisation of the photonic equipment that was necessary for my work. Although it is organised by topic, I would like to convey the chronological perception of the way I acquired 'sentience' in ultrafast photonics. It was not linear nor regular, but full of acceleration, break-through, emergency stops and setbacks. Hence many of these operations have been repeated during the years, with a better understanding of what an ultrafast High-energy system is, which implies very specific research methodologies.

A.1 Calibration of Laser System

The pivotal source in my high-energy experiment was a 5 mJ-class Titanium Sapphire (Ti:Sa) regenerative amplifier (Coherent Libra-He). The Libra was specified as generating ⟨95 fs pulses centred at 800 nm, with a 1 kHz repetition rate. and with a beam diameter of 9mm. It is important to understand that, at these peak-power levels (Above 50GW), a regenerative amplifier is typically an open construction in an open box. Drift from the

specifications are very common and can be caused by several different events (e.g. an air conditioning failure). Hence all the specifications must be constantly diagnosed.

To measure the Full Width at Half Maximum (FWHM) of the Libra pulse, a knife edge approach is exploited. A razor blade large enough to block the entire pulse is mounted onto a manual translation stage. An energy meter (Gentec: QE12SP-H-MT) was placed after the knife edge setup. The stage was then moved in increments so that the blade slowly shielded the detector form the pulse and the resulting energy recorded. The data obtained is shown in Fig. A.1.

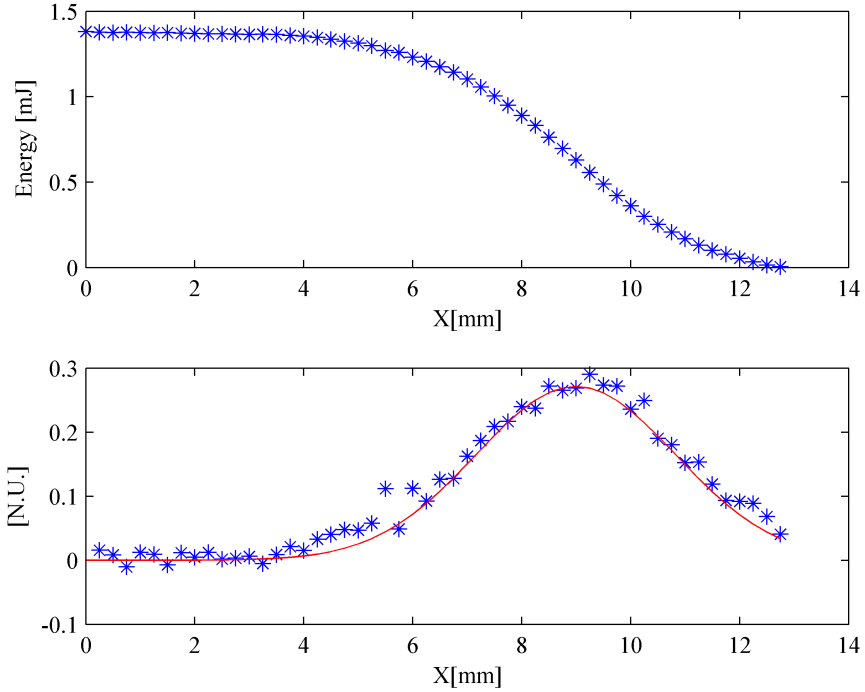

Figure A.1: Top: A knife edge measurement of detected energy against translation of the knife edge. The measurement was performed on the Libra. Bottom: Reconstruction of the Gaussian pulse shape from the knife edge measurement, based upon the integral relation between the knife-edge measurement and the beam profile. The blue shows the data, and the red shows the fitted curve used in calculations.

A Gaussian function of the form shown in Eq. A.1 is fitted to the function:

$$f(x) = ae^{-\frac{(x-b)^2}{2c^2}} \tag{A.1}$$

For a Gaussian function, the FWHM is equivalent to $2\sqrt{2ln2}c$, so for the fitted curve shown in Fig. A.1 I obtained the FWHM of 11.16mm. The relation, for a Gaussian beam, between the FWHM and the beam waist is $w = \sqrt{\frac{FWHM^2}{2ln2}}$. So I calculated a beam waist

of 9.48mm.

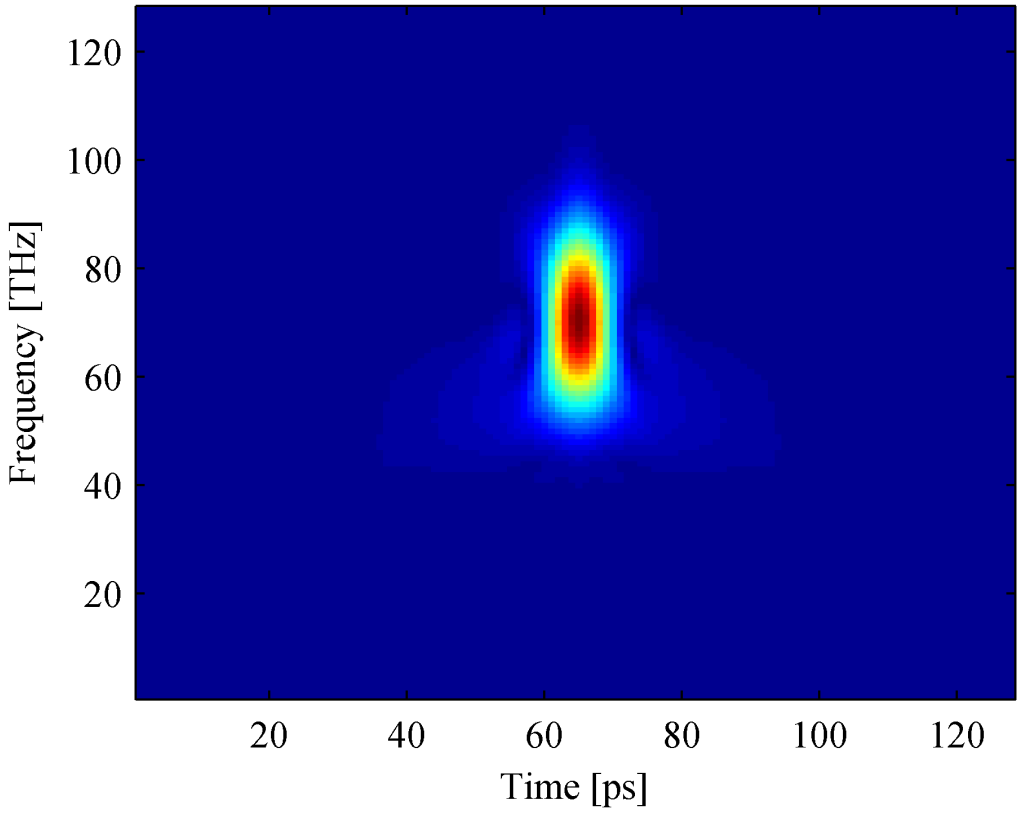

Figure A.2: FROG measurement performed on the Libra, showing a spectrogram of the pulse.

The next step was to analyse the pulse of the Libra. This was achieved using a Frequency-Resolved Optical Gating (FROG) setup. The FROG used was custom built in the lab, and had previously been calibrated. The FROG is an industry standard characterisation technique for ultrafast pulses. FROG uses algorithms to retrieve the amplitude and phase starting from the experimentally measured "spectrogram", which is a 2-Dimensional matrix, technically the power spectrum of the optical signal obtained by the nonlinear product of the pulse with the same pulse replica delayed in time. From the spectrogram, a retrieval algorithm can be used to determine a pulse that can produce it. In general terms a pulse can be formalised as

$$E(t) = A(t)E^{i\omega t+\phi(t)} \tag{A.2}$$

Hence the complete information for a pulse at a certain point in time (t_0) and the phase ($\phi(t_0)$). In practice, to reconstruct the pulse in N point in time we require at least 2N points in independent measurement. In general terms we can immediately observe

that in principle a pure intensity measurement, such as using a fast photodiode (although sub-ps pulses are too short to be measured in such a fashion), cannot provide a complete pulse description.

Yet the phase is extremely important because it determines the field-matter interaction of the pulse in a medium. In addition, in practical terms, any high-energy source like the Libra possesses a compression stage that can be tuned to obtain a flat phase pulse which corresponds to the shortest pulse that can be obtained from the source (i.e. the transform limited output condition).

For each of the N temporal delays, the FROG acquires the spectrum of the nonlinear product at M different frequencies. Hence, the FROG operates under the assumption that a $M \times N$ information space is so redundant that it an originate a unique set of N amplitudes and phases.

This is very important because there is not an easy way to correlate the spectrogram in Fig. A.2 and the pulse amplitude and phase profile without a complex best-fit algorithm. However, a perfect transform limited pulse is represented by a symmetric ellipse in the spectrogram, which is the method in which FROG can be exploited for diagnostic purposes.

The specific FROG design exploited is named Second-Harmonic FROG, it exploits a nonlinear crystal, in our case a Beta Barium Borate (BBO) to generate the sum-frequency (second harmonic) of the two pulse replica. The FROG output is then represented by 400nm beam which has a spectrum that varies with the relative delay between the two pulse replica. A spectrometer (AvaSpec-ULS2048XL-EVO) is used to measure the second harmonic spectrum. The spectrogram obtained for the Libra is shown in Fig. A.2. In this instance, the FWHM of the Libra was calculated to be 108fs.

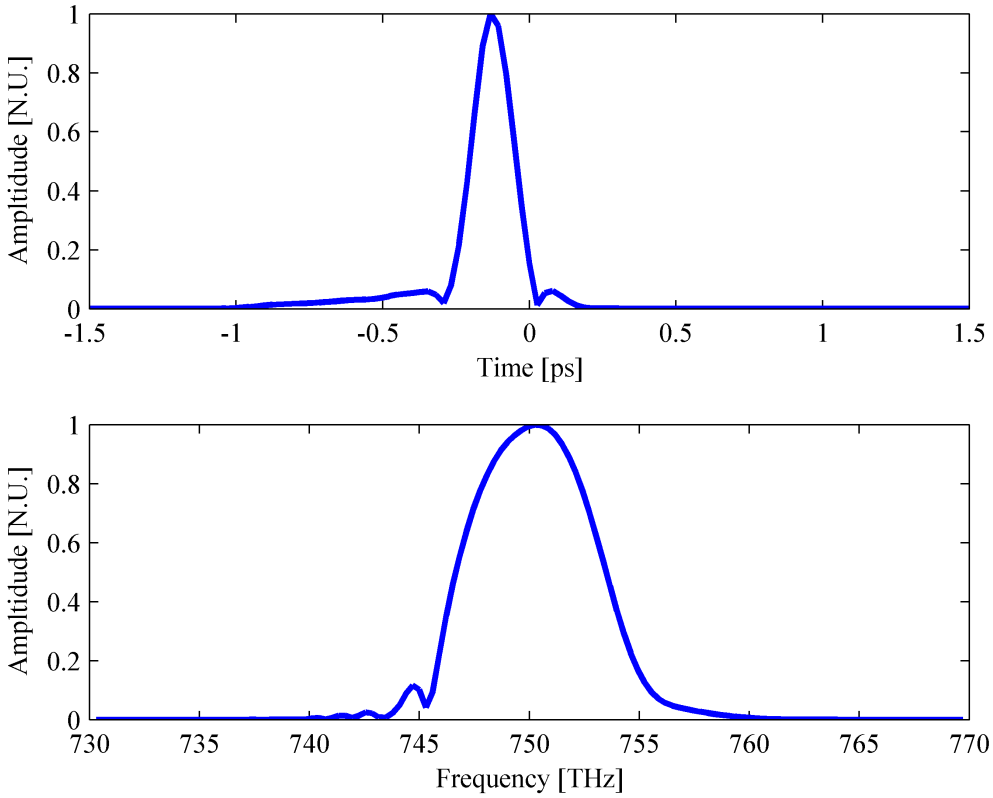

Figure A.3: Top: Reconstruction of the amplitude of the Libra pulse intensity, in the time domain, extracted from the frog measurement. Bottom: Reconstruction of the spectral amplitude of the Libra pulse, in the frequency domain, extracted from the frog measurement. In both cases, the amplitude has been normalised against the respective peak amplitudes.

A.2 THz-TDS system

A.2.1 Design

Once the characterisation of the Libra had been completed the construction of the THz-TDS system began. Initially, the THz-TDS system was built in the transmission configuration as shown in Fig. A.4. The setup comprises of two beam lines, separated by a beam splitter. The THz excitation pump (≈1.5mJ) and the optical sampling probe (≈1μJ) for the detection line. Optical Rectification (OR) is exploited on the generation pump line to generate a THz pulse. A 10 mm x 10 mm x1 mm $<$ 110 $>$ ZnTe crystal is used as the generation source. A delay line (Thorlabs DDS220/M) was exploited to control the relative delay between the THz and probe pulses. A pellicle beamsplitter was used to

recombine the THz and probe pulses so that they propagate collinearly. THz electro-optic detection is implemented by copropagating the THz field and the optical sampling probe through a standard 10mmx10mmx1mm $< 110 >$ ZnTe crystal. The beam then passed through a $\frac{\lambda}{2}$ waveplate and a Wollaston prism. A pair of balanced photodiodes (custom built in house) was used to detect the optical pulses, and a Lock-In amplifier (Standford SR510) and optical chopper (Thorlabs MC2000B-EC) to retrieve the THz field with a high signal-to-noise ratio.

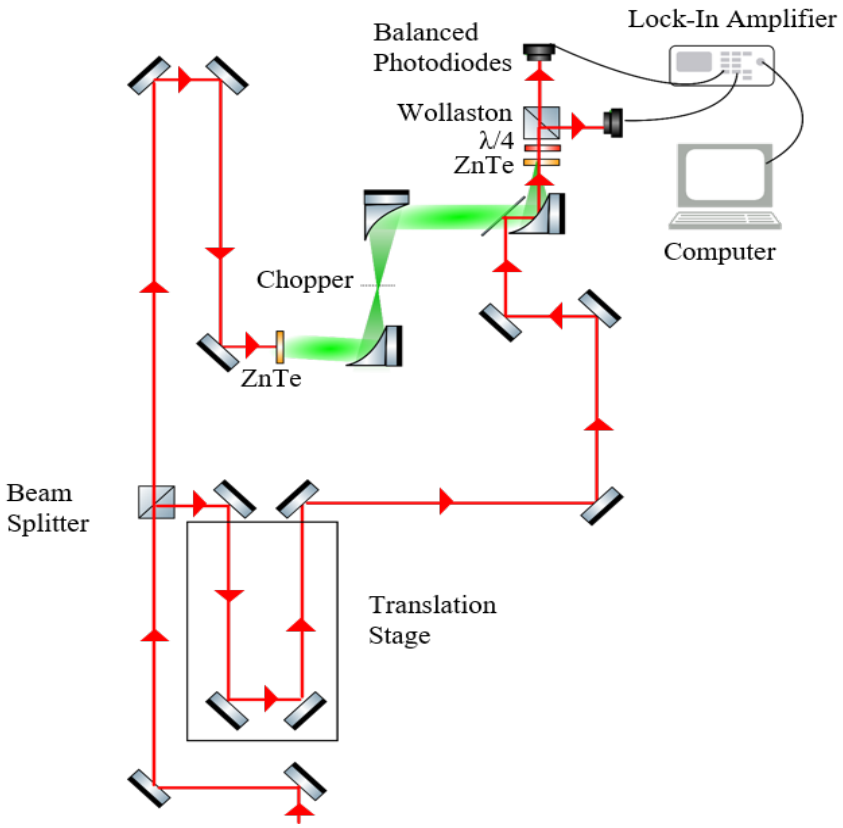

Figure A.4: Experimental setup for the THz-TDS with a ZnTe sample mounted in a transmission configuration The red beam path denotes the 800nm optical beam path, while the green beam bath denotes the THz emission.

A.3 Benchmark of InAs emission

To exploit the InAs as the THz emitter, in the setup a few modifications were made to the THz-TDS setup shown in Fig. A.4. In particular, the geometry was changed from a transmission setup to a reflection setup. The InAs sample used was a 10mmx10mmx0.5mm $< 100 >$ unless otherwise stated. The doping of the sample which was undoped, but due to the nature of InAs was slightly n-doped. The InAs THz-TDS is shown in Fig. A.5.

Fig. A.6 shows a comparison between a typical TDS of InAs and a typical TDS of ZnTe.

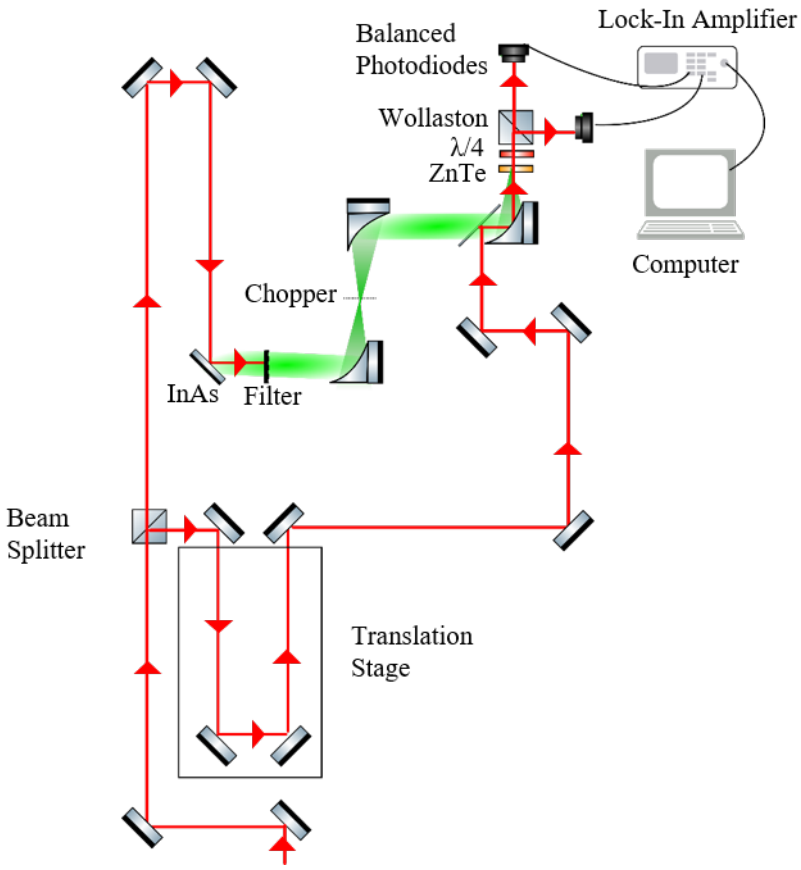

Figure A.5: Experimental setup for the THz-TDS, with an InAs sample, mounted in a reflection configuration. The red beam path denotes the 800nm optical beam path, while the green beam bath denotes the THz emission.

The peak THz field emission of InAs is roughly $\frac{1}{3}$ of the emission for ZnTe. Both traces were taken with the input beam p-polarised and the detection ZnTe orientated to detect p polarisation. Both the InAs and the ZnTe were rotated so that they were oriented to emit maximum THz. ZnTe is used in a transmission geometry so the entire length of the crystal is used in the generation process (1mm). In InAs the skin depth at a wavelength 800nm is 100-200nm (citation, and as the InAs is used in a reflection geometry, the generation process only occurs over this length. Therefore it can be said that per unit thickness InAs has a higher efficiency in the generation process. Generation of THz from InAs occurs due to three main processes these are: SOR, the photo-Dember effect and surge current migration. To fully understand the generation in InAs it is important to estimate the prevalence of each of these mechanisms in the experimental configuration. Reid highlights that each of the mechanisms have a different relationship to the input polarisation of the laser, so by investigating the input polarisation the composition of the THz emission

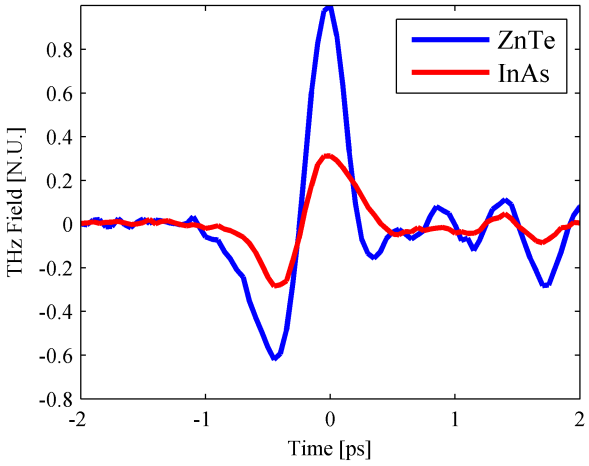

Figure A.6: Trace showing a THz-TDS emission of two different substrates: ZnTe (Blue) and InAs (Red). Both traces are normalised with respect to the ZnTe to show the difference in efficiency.

from the different generation mechanisms can be determined. Fig. A.7 shows polarisation against peak THz field for an undoped InAs $< 100 >$ sample. The detection crystal was orientated so that s-polarised was detected. It is noticeable that there is a two-fold symmetry with a slight pedestal. Since carrier related emission techniques such as the photo-Dember effect and surge current emission do not emit THz in the s-polarisation, the large polarisation dependence shown can be described by the emission mechanism SOR, due to linear optical properties and surface nonlinear tensor elements of the InAs, and therefore depends only on the polarisation of the input beam. The slight pedestal shown in this data is likely due to the photon-drag effect. Fig. A.8 shows polarisation against peak THz field for an undoped InAs $< 100 >$ sample. The detection crystal was orientated so that p-polarised was detected. Similiar to in Fig. A.7 there a large two fold rotation dependence on the input polarisation which can be explained by SOR. Although, in addition a small part of the polarisation dependence is also due to Fresnel reflectivity in the p-polarised THz signal. In the p-polarised THz emission there also exists pedestal which is likely due to photocarrier emissions such as the photo-Dember effect. It is concluded that the most dominate emission process in the InAs configuration is SOR.

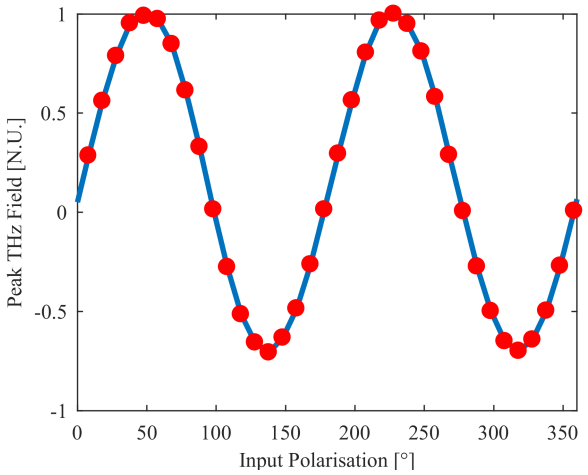

Figure A.7: Trace showing how the peak THz field emission changes with input polarisation angle in an undoped InAs < 100 > sample. 0 degrees on the input polarisation corresponds to exciting with a p-polarised beam. The detection was configured so that the s component of the emission was detected.

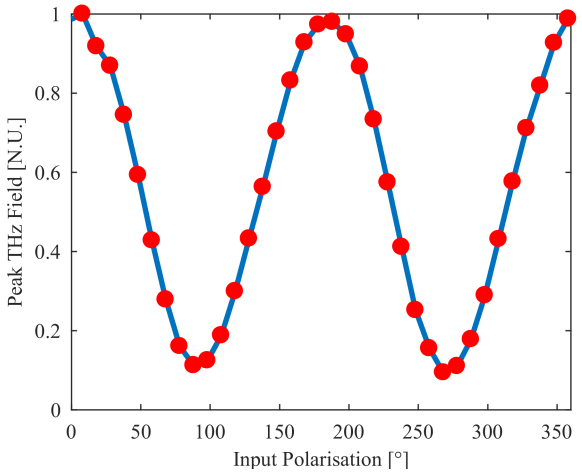

Figure A.8: Trace showing how the peak THz field emission changes with input polarisation angle in an undoped InAs < 100 > sample. 0 degrees on the input polarisation corresponds to exciting with a p-polarised beam. The detection was configured so that the p component of the emission was detected.

Appendix B

Authored Publications

The work presented in this thesis has resulted in two high impact factor publications as first author, four articles in submissions, four conference proceedings and a patent in submission. The details of which will be presented here.

B.1 Journal articles

[1] **L. Peters**, J. Tunesi, A. Pasquazi and M. Peccianti, "Optical Pump Rectification Emission: Route to Terahertz Free-Standing Surface Potential Diagnostics". Scientific Reports **7**, ; doi:10.1038/s41598-017-08734-z (2017)

[2] **L. Peters**, J. Tunesi, A. Pasquazi and M. Peccianti, "High-energy terahertz surface optical rectification". NANO ENERGY **46**, ; https://doi.org/10.1016/j.nanoen.2018.01.027 (2018)

B.2 Journal articles (In submission)

[3] D.C. Zografopoulos, K.P. Prokopidis, A.Ferraro, L. Peters, M. Peccianti and R.Beccherelli "Numerical and experimental time-domain characterization of terahertz conducting polymers." (in submission to IEEE PTL.)

[4] **L. Peters**, J. Tunesi, S. Ogilvie, M.Large, A. Pasquazi, A. Dalton and M. Peccianti, "Terahertz Emission via Graphene Enhanced Surface Optical Rectification." (in submission to Nanoenergy.)

[5] J.S. Totero Gongora **L. Peters**, J. Tunesi, M.Clerici, A. Pasquazi and M. Peccianti, "Terahertz Emission from all Optical Surface Optical Rectification." (in submission

to ACS photonics.)

[6] **L. Peters**, J. S. Totero Gongora, L. Olivieri J. D. Tunesi, A. Fratalocchi, A. Pasquazi, and M. Peccianti, "Nonlinear THz Plasmonic Reponses in Silicon Metamaterials." (in preparation, the author order is not defined yet.)

B.3 Conference Proceedings

[7] **L. Peters**, J. D. Tunesi, A. Pasquazi, and M. Peccianti, "Optical Pump Rectification Emission: Terahertz Surface State Diagnostics," in Advanced Photonics 2017 (IPR, NOMA, Sensors, Networks, SPPCom, PS), OSA Technical Digest (online) (Optical Society of America, 2017), paper ITh2C.3.

[8] **L. Peters**, J. S. Totero Gongora, J. D. Tunesi, A. Fratalocchi, A. Pasquazi, and M. Peccianti, "Route to Photo-Enabled Random Terahertz Metasurfaces," in Advanced Photonics 2017 (IPR, NOMA, Sensors, Networks, SPPCom, PS), OSA Technical Digest (online) (Optical Society of America, 2017), paper IM2A.5.

[9] **L. Peters**, J. D. Tunesi, A. Pasquazi, and M. Peccianti, "Mapping of Surface Field via Nonlinear Optical Pump Rectification Emission," proc. of CLEO®/Europe-EQEC 2017 paper CD15.6.

[10] M. Missori, J. Bagniuk, M. Clerici, J. Lojewska, M. C. Misiti, **L. Peters**, R. Morandotti, A. M. Conte, O. Pulci, L. Teodonio, C. Violante, and M. Peccianti, "Terahertz Waves for Ancient Manuscripts Conservation," in 2015 European Conference on Lasers and Electro-Optics - European Quantum Electronics Conference, (Optical Society of America, 2015), paper CCP6.

B.4 Patents (In Submission)

[11] Co-inventor of a patent in submission (funded by the University of Sussex) on ultrafast pulse characterisation